Fakultät für Maschinenwesen

Lehrstuhl für Carbon Composites

Thermo-Mechanical Coupled Simulation of the Thermoset Automated Fibre Placement Process

Roland F. X. Lichtinger

Vollständiger Abdruck der von der Fakultät für Maschinenwesen der Technischen Universität München zur Erlangung des akademischen Grades eines

Doktor-Ingenieurs (Dr.-Ing.)

genehmigten Dissertation.

Vorsitzender:	Univ.-Prof. Dr.-Ing. Gunther Reinhart
Prüfer der Dissertation:	Univ.-Prof. Dr.-Ing. Klaus Drechsler
	Prof. Kevin Potter, Ph.D.
	(University of Bristol, U.K.)

Die Dissertation wurde am 24.03.2015 bei der Technischen Universität München eingereicht und durch die Fakultät für Maschinenwesen am 25.09.2015 angenommen.

Für meine Eltern

For my parents

Abstract

With increased demand for carbon fibre reinforced parts, automated manufacturing methods like fibre placement are well established for aircraft and spacecraft manufacture. However the automated manufacturing process is still in development despite its extensive use in industry. The quality of the automated deposition processes heavily depends on the tack of the preimpregnated thermoset fibres. Without sufficient tack the fibres do not stick to the surface and the process will fail. One key aspect to influence the magnitude of tackiness and therefore the quality of parts attainable from the thermoset Automated Fibre Placement process is the impact of the heat source. For most industrial applications, an infrared heater is used and suitable process windows are still defined by trial-and-error approaches. Further, to utilize AFP's strong potential to deposit fibres on complex curvature surfaces or even steer the slit-tapes along a load path, the need arises to analyse emerging defects like gaps or bridging. The deformability of the compaction roller further influences tack with contact time and compaction pressure. Commercially available software solutions allow the kinematic offline-simulation of the lay-up process, but do not take into account any process parameters or material properties. To reduce this gap in design and to understand the complex interactions of the process parameters the main goal of this thesis is the coupling of those thermal and mechanical interactions. Different analytical and numerical models were developed to achieve this goal. Robust thermal prediction tools in different dimensions are presented, and validated with experiments with very good agreement to simulation values. The deformation behaviour of an industrial compaction roller on convex and concave tooling is studied and a simulation model of the roller developed that is able to accurately predict the deformation behaviour and pressure distribution under the roller. With the individual thermal and mechanical models a sequentially coupled thermal-mechanical model with geometry update is developed that is able to capture the continuous placement process, including the result variables compaction pressure, contact time and process temperature. Further, an analytical relationship between adhesive failure and compaction pressure, process temperature and feed rate is found, with good agreement to experimental results from literature.

Zusammenfassung

Durch die zunehmende Nachfrage von kohlefaserverstärkten Bauteilen in der Luft- und Raumfahrt sind automatisierte Fertigungsverfahren wie Tapelegen und Automated Fibre Placement fest etabliert. Trotz des weitreichenden Einsatzes in der Industrie befinden sich diese automatisierten Verfahren noch in der Entwicklung. Die Qualität der automatisierten Ablage hängt sehr von der Klebrigkeit der imprägnierten Fasern ab. Ohne ausreichende Klebrigkeit werden die Fasern nicht auf der Werkzeugoberfläche haften und so den Prozess gefährden. Einer der Hauptaspekte, welcher die Klebrigkeit und damit die Qualität der Ablage beeinflusst, ist der Einfluss der Wärmequelle. Für die meisten industriellen Anwendungen wird eine Infrarot-Lampe verwendet, und entsprechende Prozessfenster durch Versuche bestimmt. Um das Potentials des AFP's ausnutzen und Fasern auf einer komplexen Geometrie, oder gar lastpfadgerecht in der Ebene gekrümmt abzulegen müssen auftretende Effekte wie Spaltbildung oder Brückenbildung untersucht werden. Die Klebrigkeit wird ebenfalls durch das Verformungsverhalten der Kompaktierungsrolle beeiflusst, da diese von der Höhe und der Dauer des aufgebrachten Druckes abhängig ist. Kommerziell verfügbare Software lässt eine kinematische Offline-Simulation des Ablegeprozesses zu. Allerdings werden weder Prozessparameter noch Materialeigenschaften berücksichtigt. Um diese Lücke in der Entwicklung zu schließen und die komplexen Zusammenhänge der Prozessparameter zu verstehen ist das Ziel dieser Arbeit, eine Kopplung dieser thermischen und mechanischen Zusammenhänge zu untersuchen. Dafür wurden verschiedene analytische und numerische Modelle entwickelt. Es werden robuste Werkzeuge zur thermischen Simulation in unterschiedlichen Dimensionen präsentiert, welche anhand von Versuchen mit sehr guten Ergebnissen validiert wurden. Die Deformation einer industriell eingesetzten Kompaktierungsrolle wurde auf verschiedenen konvexen und konkaven Oberflächen untersucht, und daraus ein Simulationsmodell abgeleitet, welches das Verformungsverhalten sowie die Druckverteilung unter der Rolle akkurat abbildet. Weiterhin wurde ein analytischer Zusammenhang zwischen adhäsivem Versagen und Kompaktierungsdruck, Prozesstemperatur und Ablegegeschwindigkeit ermittelt, welcher durch Ergebnisse aus Literatur validiert wurde.

Acknowledgement

Contents

Nomenclature

Symbols

Arabic letters

a	$[mm]$	bisected contact area for hertzian contact
A	$[mm^2]$	contact area
A_C	$[\%]$	true contact area
a_m	$[N/mm]$	scale factor for maximum adhesive energy release rate
B_1	$[N \cdot mm^2]$	bending stiffness
c	$[-]$	constant surface roughness coefficient
c_p	$[\frac{J}{gK}]$	specific heat
dW^e	$[J]$	stored elastic energy of the peel material
dW^v	$[J]$	dissipated plastic energy of the peel material
E_i	$[\frac{N}{mm^2}]$	elastic modulus
F	$[N]$	compaction force
F_{L_B}	$[\frac{N}{mm}]$	line load due to grafity
F_P	$[N]$	peel force
F_{PS}	$[N]$	compaction force evaluated by PRESCALE
F_{TM}	$[N]$	compaction force measured by universal testing machine
g	$[mm]$	gap width between individual paths
G_{ij}	$[\frac{N}{mm^2}]$	shear modulus
$G_{IC_{adh}}$	$[N/mm]$	energy release rate due to adhesive failure
$G_{IC_{coh}}$	$[N/mm]$	energy release rate due to cohesive failure
G_{IC}	$[N/mm]$	energy release rate
g_1	$[mm]$	gap width at ramp centre
g_2	$[mm]$	gap width at the top of the ramp
g_3	$[mm]$	gap width at the bottom of the ramp
g_{max}	$[mm]$	maximum allowable gap
h	$[mm]$	ramp height
h_0	$[mm]$	stack thickness
k_{sigma}	$[-]$	empirical peel tack parameter
k_T	$[-]$	parameter dependent on bond deformation
l_0	$[mm]$	overhang length of sample
l_1	$[mm]$	gap length at bottom plane

l_2	$[mm]$	gap length at top plane
l_r	$[mm]$	path length on inclined plane
l_S	$[mm]$	length of sample
m	$[-]$	empirical peel tack parameter
m_S	$[g]$	mass of sample
o_g	$[mm]$	parallel offset of one path on parallel planes
p	$[MPa]$	normal contact pressure
p_{corr}	$[-]$	correction factor
$\mathbf{\dot{q}}$	$[\frac{W}{mm^2}]$	heat flow vector
R	$[mm]$	roller outer radius
r_{min}	$[mm]$	minimum steering radius
$\mathbf{T}$	$[°C]$	temperature vector
v	$[\frac{mm}{s}]$	peel rate
W	$[mm]$	width of the peel material
w_i	$[mm]$	distance between two paths

Greek letters

α	$[°]$	path angle
ϵ	$[-]$	error criterion for path optimisation
ε	$[-]$	emissivity
η_T	$[Pa \cdot s]$	temperature dependent viscosity of the resin
γ	$[°]$	theoretical steering angle
γ_{min}	$[°]$	minimum allowable steering angle
$\lambda_{\mathbf{i}}$	$[\frac{W}{mmK}]$	heat conductance
$\nu_{\mathbf{ij}}$	$[-]$	poission ratio
φ	$[°]$	peel angle
φ_f	$[-]$	fibre volume fraction
ρ	$[\frac{g}{mm^3}]$	density
θ	$[°]$	ramp angle

Abbreviations

AFP	Automated Fibre Placement
ATL	Automated Tape Laying
CAD	Computer Aided Design
CAx	Computer-aided technologies
CFRP	Carbon Fibre Reinforced Plastic
CLT	Classical Laminate Theory
DoF	Degree of Freedom
FD	Finite Differences
FEA	Finite Element Analysis
FEM	Finite Element Method
HMI	Human machine interface
IR	Infra red
LED	Light-emitting diode
MD	Multidirectional
NC	Numerical Control
NCF	Non-Crimp-Fabric
OoA	Out-of-Autoclave
prepreg	Pre-Impregnated Carbon Fibres
PSA	Pressure Sensitive Adhesive
PTFE	Polytetrafluoroethylene
PUR	Polyurethane
TCP	Tool Centre Point
TTS	Time-temperature superposition
UD	Unidirectional
WLF	Williams-Landel-Ferry

1. Introduction

With increasing energy cost the demand for fuel efficient products under similar or even elevated performance requirements arises. To achieve this goal there is the need for the continuous improvement of products to fully utilize their light weight potential.

Parts made from carbon fibre reinforced plastics (CFRP) combine these opposed goals of light weight design with elevated performance, as the specific strength and stiffness of CFRP parts exceed those made from metal [1]. CFRP consist of at least two components: the matrix and the fibres. The mechanical stiffness and strength is essentially carried by the fibres, while the matrix allows for the fixation of the fibres in their desired position, stabilisation of the fibres in compressive and shear load cases and the load transfer between individual fibres [2]. This concept allows the designer to fully utilize the anisotropic behaviour of the composite and create effective parts suited to their application. In the aerospace industry composite materials are already used in a wide range of products, e.g. the Airbus A350XWB or the Boing 787 Dreamliner consist of over 50 % of CFRP [3].

CFRP parts are usually manufactured from a layup of dry fibres that are infiltrated by resin, or a collation of fibres preimpregnated with resin - so called prepregs [4]. Prepregs are suitable for hand lay-up, filament winding and many automatic lay-up processes. The component is built up iteratively on a tool surface, with individual prepreg layers that form the complete part. After layup, the laminate is consolidated and cured in the presence of pressure and temperature to obtain the final product [5], usually inside an autoclave for aerospace applications. During layup and after cure the plies are inspected for layup quality [6]. As a near-net-shape is usually not possible for CFRP, the part boundaries are machined to limits, and further assembled in the case of a multi-component part.

In the past the low level of automation was the main driver for the high cost of this technology. However, there was great progress in terms of automation of CFRP parts within the last decade. One of the most promising processes for the automated manufacture of high performance CFRP parts is the Automated Fibre Placement (AFP) process. With the high level of automation there is great potential in time and labour cost, and with cut-and-restart capabilities scrap may be reduced.

For the improvement and expansion of the application of the AFP process and the associated process manufacturing chain the introduction of process simulation is a valuable tool. Process simulation provides a basis for a well-founded physical, mechanical and thermodynamic understanding of the process. In the product development chain simulation may be used to substitute for experiments and gain optimum process parameters. With the advancement of computational capacity,

product engineering is enhanced with a faster and cost improved process chain. Different process phenomena may be distinguished in process simulation and provide important variables, that cannot be directly determined by experiments [7]. A further field of operation for process simulation is the side by side application along with the main work-flow of the process chain in terms of quality management. For verification and to ensure a constant high quality of the process control and regulation of the process is imperative. Process simulation may deliver required input values for quality control [1].

There are some promising approaches to process simulation of the AFP process, that are reviewed in detail in the individual chapters of this thesis. However, no process model so far covers all relevant phenomena of the process. Further, most process models over-simplify the process by dimensional reduction or further assumptions. Commercially available software up to this point solely covers kinematic process simulation without input of process or material properties.

1.1. Thesis objective

The main objective of the research work presented in this thesis is to develop physically based process simulation models for the Automated Fibre Placement process. These start from the analysis of basic AFP layup and lead to the detailed research of the placement on the complex geometry of a tapered honeycomb chamfer. The models shall include the relevant AFP process variables. Understanding the impact and the implication of the heat source to the process is vital for defining a stable process window. Tack of the deposition material plays a vital role in layup quality. An AFP specific model is developed incorporating all relevant boundary conditions to study the impact of variations of process variables. Further, the manufacturability of multiple curved tool surfaces is studied by the analysis of the deformability behaviour and the pressure distribution of an industrial AFP compaction roller. For understanding of the complex interaction of thermal and mechanical phenomena during the AFP process, different models are developed, from which the desired process variables are deduced. The main goals of this thesis may be summarized with:

- Study and accurately predict the complete temperature history during the thermoset AFP process including heat up and cool-off phases during placement including the effects of a diffuse infrared lamp. The geometry may consist of arbitrary tool shapes, up to multi-material tools such as a tapered honeycomb on aluminium.

- Understand deformability, contact length and contact pressure of AFP compaction rollers for their use on the complex geometry of a tapered honeycomb tool.

- Predict all relevant AFP process parameters for the placement on a tapered honeycomb structure by the means of a thermo-mechanically coupled simulation model.

- Analyse and predict the adhesive behaviour of the deposition material

1.2. Structure of the thesis

Chapter 2: Principles and state-of-the-art of Automated Fibre Placement and motivation for this work Chapter 2 presents the historical development and the detailed principle of the AFP process. Advantages of the process along with its restrictions are discussed. Additionally process parameters for the thermoset AFP process are deducted. Commercially available AFP simulation software are listed along with the basic work flow. Finally, the research needs and motivation for this thesis are explained as a bridge to the following chapters.

Chapter 3: Kinematic and mechanical analysis of the AFP process In Chapter 3 the mechanical aspects of the AFP process are studied. After the literature review, some thoughts on kinematic simulation are presented, along with experimental analysis of gaps during the placement on a tapered honeycomb. Further, the deformability of an industrial compaction roller for AFP is studied and a simulation model of the non-hertzian deformation behaviour is deducted. Additionally, the through-thickness compaction behaviour of a prepreg stack with AFP boundary conditions is investigated experimentally.

Chapter 4: Thermal measurements and thermal models for AFP After a thorough literature review of existing thermal process models for AFP, current thermal material models are derived. These are the input for the developed 1D, 2D and 3D thermal models that are explained in detail. Experimental test setups and measured temperature are presented. The experimental values are compared to simulation results of the process models. Finally the influence of process parameters and the validity of the pure thermodynamic models is discussed.

Chapter 5: Thermo-mechanically coupled model of the AFP process Chapter 5 describes the development of a temperature dependent bending model for an uncured UD prepreg tape. In combination with the information of previous chapters about

thermal and mechanical models, a sequentially thermo-mechanically coupled model is derived, that predicts the placement on a tapered honeycomb.

Chapter 6: Tack in Automated Fibre Placement - theory and application   With the input variables process temperature, compaction pressure and layup velocity, an AFP specific process model for tack of prepreg tapes is developed in Chapter 6. The model than is applied and compared to experimental values from literature.

Chapter 7: Conclusions and future applications   Chapter 7 concludes the thesis with a summary of the work conducted, and the implications of the work towards industrial applications. Additionally, possible future applications of described models are discussed, along with further research needs to increase the level of detail in the AFP process simulation.

2. State-of-the-art of Automated Fibre Placement and motivation for this work

The extended availability and declining prices for carbon fibres in the 1960s, promoted the interest in the development of an automated placement process for prepregs. These can consist of non-crimp-fabrics (NCFs), woven fabrics or unidirectional (UD) layers, which are impregnated with a thermosetting or thermoplastic resin. As part of the commercialisation of carbon fibres in the late 1960s, Automated Tape Laying (ATL) was developed [8]. ATL was designed as an alternative for the slow and imprecise manual layup [3].

In the year 1974 Goldworthy [9] patented a cutting mechanism for a machine head, which could divide a wide tape into narrower strips. This step was a response to the disadvantages of placing a wide tape on a multiple curved surface. The patent of Goldsworthy is mentioned in literature as the first available AFP machine [3].

AFP technology finally found its way into industry in the late 1980s as a synthesis of filament winding and ATL [3]. The controlled parameters are layup rate, compaction force, process temperature and tension of the tapes. The advantages which distinguish the AFP process from other automated processes are, among others, the increased degree of material utilization, the increased freedom in design and improved mechanical properties.

The increasing demand for thermoplastics for structural applications in the aerospace industry has led to the adaptation of thermoplastic materials in AFP. Since thermoplastics must be heated above their melting point, thermoplastic AFP permits a lower layup rate than with thermoset materials. Further, with phase change of the material of melting and solidifying, temperature control of the process is imperative for consolidation and in situ quality.

In the years after the introduction of the AFP technology the number of scientific publications about the AFP process increased greatly and have exceeded the publications on ATL since the 1990s [3], compare Figure 2.1. It is presumed that this trend will continue, as the AFP process is realistically still in development and is not fully understood yet.

AFP has great potential for the manufacture of complex parts in a range of different scale magnitudes, and will find its way into automotive applications in upcoming years. It is therefore imperative to gain knowledge in the basic physical mechanism during AFP to optimize the process.
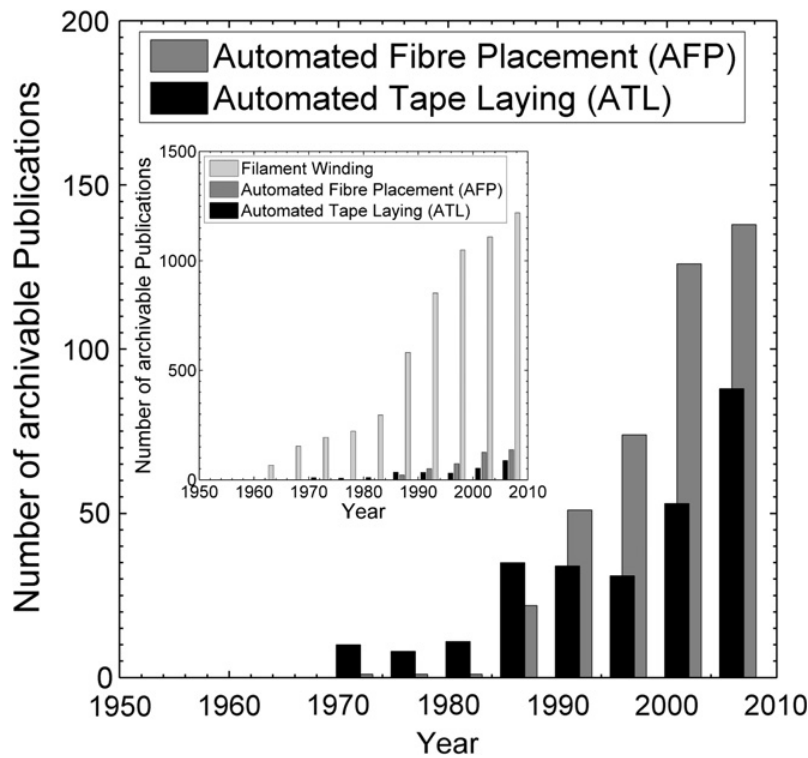
Figure 2.1. Development of scientific publications on ATL and AFP, Figure from Lukaszewicz et al. [3]

2.1. Principles of the Automated Fibre Placement process

The AFP process is largely viewed as an additive manufacturing process [10]. Unidirectional (UD) prepreg tapes are deposited on a tool surface sequentially. A roller system separates the tapes from a release film and conveys them to the AFP head to be placed. A freely rotating compaction roller presses the tapes on the tool surface, so the tapes are pulled of the spool by friction between roller, tool and tapes.

A fibre placement machine consists of nine different parts, explained in the following:

Compaction roller (1)   The compaction roller's function is to apply sufficient pressure to the slit-tapes, so they stick to the tool surface. The roller needs good deformation behaviour for an adequate conformation to a curved surface. Further, the roller needs to be treated with a release film, so that the tacky slit-tapes do not stick to the roller surface instead of the tool. When the roller presses the material on the tool surface, the resulting friction is enough to pull the tapes from their spools. The compaction roller is usually made of silicone rubber [3], in the case of the *Coriolis Composites* AFP machines the roller consists of polyurethane foam treated with a release film.
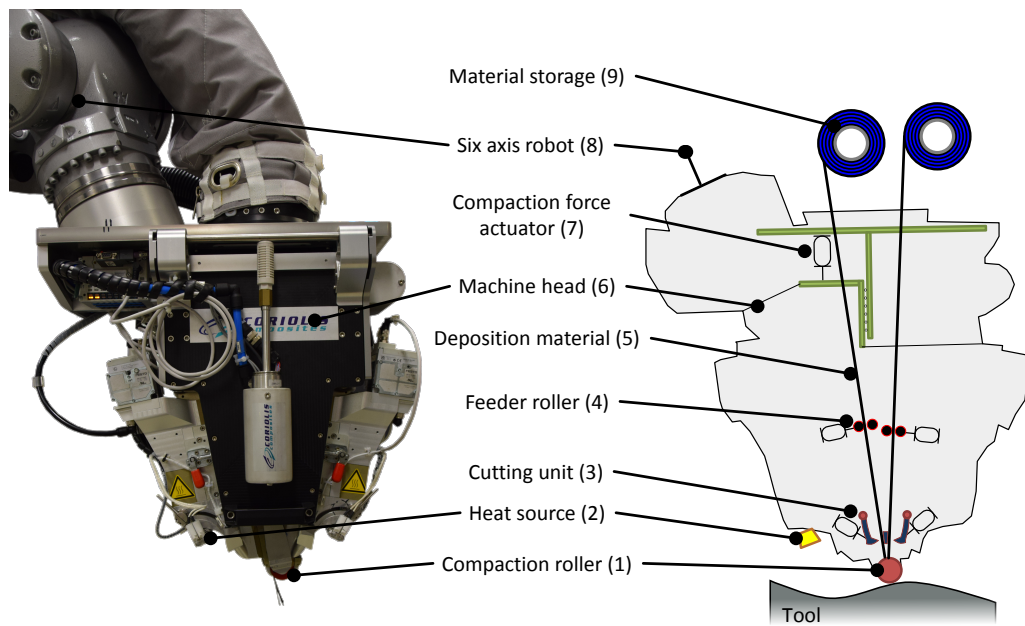
Figure 2.2. *Coriolis Composites* AFP machine (left) with design principle (right)

Heat source (2)   A heat source is needed to enhance the adhesive behaviour of the slit-tapes in the case of thermosetting resin systems. In most industrial scale thermoset AFP machines, an infra-red (IR) lamp is used, that heats the area in front of the nip point, the tapes themselves are not irradiated. In thermoplastic AFP, it is beneficial to also heat the incoming tapes to enhance bond formation.

Cutting unit (3)   The cutting unit cuts the tapes individually inside the machine head. This enables a near-net-shape manufacture. The cutting mechanism works usually with a guillotine or a rotating knife principle. The cutting unit is designed to be as close as possible to the nip-point, as the length between cutting unit and nip point defines the minimum cut length - the minimum length of the tapes to be placed.

Feeder rollers (4)   The feeder rollers are mounted inside the machine head, in front of the cutting unit. Their function is to hold the tapes once they are cut, and feed them to the nip point when the tapes need to be (re-)started. The feeder rollers force the tapes forward, until the tapes are pressed on the tool by the compaction roller and pulled out by friction. Then the feeder rollers are released and allow free movement of the slit-tapes.

Deposition material (5)   The deposition material is driven through guiding channels in the machine head towards the compaction roller, to be deposited on the

tool surface. Usually the material is manufactured from prepreg tapes slit to desired width. Therefore the deposition material is referred to as slit-tapes in the following.

The slit-tapes have adhesive characteristics, so they stick to the tool surface. A detailed description of general AFP material can be found in Section 2.1.3.

Machine head (6)   The machine head incorporates the housing for all relevant parts of the fibre placement machine.

Depending on the design of the machine head, it is capable of placing between one and 32 individual slit-tapes simultaneously. For every slit-tape individual feeder rollers, cutting units, guiding channels and material storage need to be available.

Force application and clearance adjustment (7)   One of the AFP process parameters is compaction force. In industrial scale AFP machines, the compaction force is usually applied by pneumatic equipment. This equipment also incorporates a clearance adjustment, so compensation of small geometric irregularities is not purely covered by the deformability of the compaction roller.
In the case of the *Coriolis Composites* AFP head, the machine is able to compensate $\pm 10 \, \text{mm}$ of vertical distance.

Six axis robot (8)   The AFP head is mounted on a robot with a minimum of six axes. It must be able to reach all required positions within the robotic cell. The robot may be of a gantry type design or of the design of a robotic arm. Further axes may be added for a linear motion of the complete robot or movement of the tool.

Individual material storage and issue (9)   The material to be placed is stored individually on spools. In the case of thermoset resin system, the storage unit needs to be cooled and humidity controlled. There are concepts for AFP machines that have the material storage on the placement head, travelling along with the robot, and concepts with individual storage creels that need variable tape guiding channels [11] that guide the tapes towards the placement head.

Tape tension needs to be controlled, so there is constant and as little as possible tape tension throughout the process. Variable systems exist to maintain stable tape tension. In the case of *Coriolis Composites*, the concept of the "Multiwinch®"[12] is employed. This ensures constant minimal tape tension on the placement head.

Tool   The tool is not part of the AFP head. However it is crucial for the AFP process. It is independent of the fibre placement head, and is contained in the robotic

cell. It may be designed freely in concave and convex curvature, with the single geometric restriction of collision avoidance of the placement head. The tool is mounted on a tool carrier, which may have additional degrees of freedom. The tool surface needs to be treated with a release agent or alternatively with a vacuum bag, so the placed laminate can be safely removed for curing.

2.1.1. Process advantages

The AFP process is the advancement of filament winding and ATL. It combines the advantages of both processes, which are discussed in the following:

Cut-and-restart capability along with reduction of material scrap The ability of the AFP process for cut-and-restart operations is one major advantage. With this capability it is possible to implement sectoring [13], i.e. various fibre angles on a lamina level.

Closely related to cut-and-restart capabilities is the reduction of scrap. As the machine is able to closely cut and restart material, a near-net-shape preform is possible to manufacture. Figure 2.3 shows the manufacture of a flat plate with cut-out of a circular hole

Figure 2.3. Reduced material scrap with the help of cut-and-restart operations and near net shape manufacture

Scrap reduction of AFP is a major cost advantage compared to other processes, as material scrap is reduced up to 37 % [8].

Automated manufacturing method The automated nature of the process implies that it is precise and repeatable. Further, the cost of manual labour is reduced

considerably, along with elevated material throughput. Soutis [14] interprets that manufacturing cost of manual layup are 60 % higher compared to automated layup. However Krolewski and Gutowski [15] state that with a low part volume typical for the aerospace industry the high material cost and high initial investment negates the saving in manual labour. Nevertheless they conclude that automation is critical for future application, and they advice on parts designed for manufacturability in three points:

- Create repetitive manufacturing steps,

- Improve part quality and reduce material cost and

- Reduce the cost of equipment, in particular the autoclave investment cost.

Variable stiffness composites   With the six degrees of freedom of the placement robot, there is the possibility to manufacture variable stiffness composites [13] (Figure 2.4) with in-plane steering of the fibres along a defined load path.
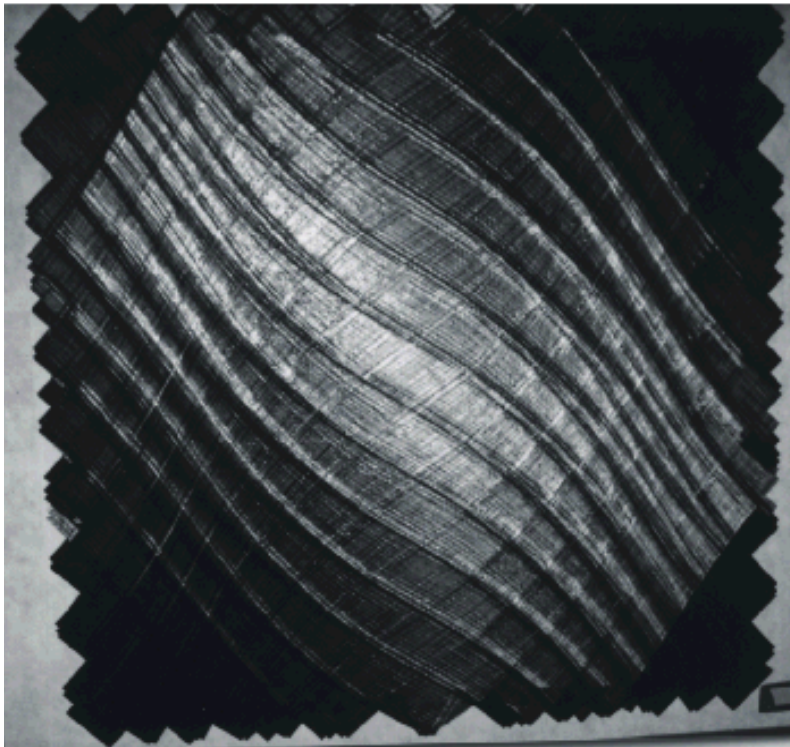
Figure 2.4. A panel manufactured with fibre steering, therefore increasing eigenfrequencies, compare Tatting and Gürdal [16]

Open contoured multiple-curved tool surface   With the adhesive behaviour of the slit-tapes and the deformability of the compaction roller, it is possible to manufacture open contoured convex and concave surfaces. Further, with the individual

slit-tapes and steering capabilities, it is possible to manufacture multiple-curved surfaces.

In situ manufacture for thermoplastic fibre placement   Sarrazin and Springer [17] state that the in situ manufacture of CFRP parts with thermosetting matrix is not possible, as the heat input is not sufficiently long enough. They claim that the maximum reached cure stays below 2 %. However, with the introduction of thermoplastic fibre placement with laser heating, in situ manufacture has become possible recently [18]. However, full on-the-fly consolidation still requires an extended amount of research. Nevertheless this opens up many possibilities of cost reduction as well as size restrictions, as an autoclave is no longer needed for consolidation.

2.1.2. Process restrictions

Although the process has many advantages, there are some restrictions concerning cost and efficiency as well as process restrictions.

Cost of tape material and initial investment   Depending on the size of the part to be manufactured by AFP and the amount of debulking cycles, material cost makes up to 30 % of the total manufacturing cost [19].
The AFP material is, compared to other CFRP materials, relatively expensive. The reason for that is twofold: First, the demand for slit UD prepreg tape is low. Nowadays AFP finds its application solely in the aerospace industry, where precision and repeatability are key factors in manufacture. Here the material throughput is little compared to automotive industry. Second, the slit-tapes require an additional step in manufacture. Wide UD Prepreg roles need to be cut to achieve the exact width of the slit-tapes, and added to another spool with additional backing paper. This further increases the material cost.
Mazumar [5] states material cost for aerospace parts hand layup from 33 €/ Kg to 220 €/ Kg. The cost for aerospace grade slit-tape material are around 200 €/ Kg, an increase from 13 % to 650 %, given the current currency exchange rate. It is presumed that the highly reduced scrap rate compensates only partly for the elevated material cost.
Further, the cost of initial investment is considerable higher than manual layup. The cost of a complete AFP cell is well in excess of 1M €. Additionally, tool cost as well as the cost for autoclave curing increase the total initial investment further.

Material variability   Between each path of the placement usually a gap is defined to accommodate for variations in material width or machine control issues, compare

Lukaszewicz [6]. The risk of material variability in automated layup is high, as usually there is no online control of the material to be placed in an industrial scale AFP process.

Potter et al. [20, 21] state a significant variability in resin content of up to 2%. They find a variability in fibre misalignment of up to $3.8°$ and conclude that design practises need to include these variations. Potter further states [22] that there is little possibility to improve on the variability of prepreg as-delivered from manufacturer, but that the specification for variability needs to be sufficient.

Crowley et al. [23] propose the establishment of acceptable levels of variations to avoid scrap parts. As the detection of flaws in a part is only possible at the last production step, the embedded cost of the scrapped part is maximised. They propose acceptance criteria [24] for individual process steps and compare these measurements to a proposed defects knowledge-base.

Control of process variables   The control of the process variables compaction pressure, layup rate and temperature is challenging. Most process variables are interacting. The layup rate influences process temperature, as the heat source has more time to dwell at a specific area. With decreased compaction pressure, thermal contact efficiency increases, influencing the temperature distribution. Further, layup rate as well as compaction pressure may change within one single lay down pass. Therefore, control of the process variables is imperative. In industrial scenarios, most process variables are fixed to a certain level, and are determined experimentally by process testing.

Necessity of an autoclave   For thermoset AFP, the following process step after layup is cure in an autoclave. There are concepts for Out-of-Autoclave (OoA) cure aerospace grade materials [25], however they are still in a state of development. Sarazzin and Springer [17] state that in situ cure for thermosetting resin systems is not possible using AFP.

State of the art for thermoplastic AFP is the consolidation of the layup inside an autoclave. This reduces voids in the layup as well as increases bond strength between layers. Nowadays, in situ layup for thermoplastic AFP becomes possible [18]. However, before this technology can be advanced to an industrial level, more research is necessary.

Material throughput   The theoretical calculated material throughput for AFP machines is stated from Lukaszewicz [6] (Figure 2.5).

However, realistic material throughput ranges around $10\,\mathrm{Kg/h}$ [3], as most of the machine time originates from secondary operations, e.g. turning and positioning.
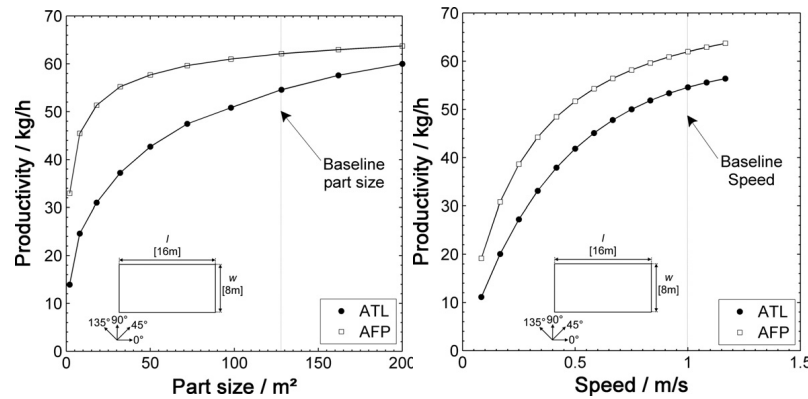
Figure 2.5. Material Throughput of AFP compared to ATL in part size (left) and layup
           rate (right) [6]

Minimum cut length   The distance between the cutting unit and the nip point
of the compaction roller - minimum cut length - restricts the minimum length of a
slit-tape path to be placed. This means a slight increase in material scrap as well as
a deviation from near-net-shape, especially in corners of the layup where the length
of a placement paths would be below this minimal length. However, this restriction
has little influence on the process, and is assumed to influence material cost as well
as production time only marginally.

2.1.3. AFP material

AFP material can be divided into three categories:

1. Dry bindered fibres

2. Fibres preimpregnated with thermoset resin

3. Fibres preimpregnated with thermoplatic resin

Most commonly used material in an industrial scale are fibres preimpregnated with
thermoset resin. There are two ways to manufacture the tapes: to cut them from a
UD prepreg spool with much wider size - so-called slit-tapes. This has the advantage
that the width of the tapes, as well as thickness and fibre volume fraction, is con-
stant. Second, fibre tows with a certain filament count can be spread to a specified
size and impregnated with resin - so called tow-pregs. There the advantages are that
all fibres are continuous and are not cut. Further, the price for tow-pregs is lower
than for slit-tapes. The width of AFP material ranges from 3.2 mm to 25.4 mm.
A relatively new and upcoming technology is the automated placement of dry
bindered fibres. They allow for a expanded freedom in design, as more complex
geometry as well as smaller steering radii are possible to manufacture.
Further, fibres preimpregnated with thermoplastic resin - thermoplastic tapes - are

used for in situ manufacture of CFRP with thermoplastic resin systems. During placement the resin is melted with a heat source, and the tape is welded to the underlying substrate.

In current study the focus is in areospace grade thermoset slit-tape, therefore a detailed description of material properties of dry fibres or thermoplastic tapes is omitted.

2.2. Thermoset AFP process parameters

The AFP process offers high freedom in design, as complex parts with multi-material tooling and limited size as well as large parts with relatively simple design, e.g. skin structures for aerospace industry [26], are possible. Therefore, the process variables of AFP need to be adjusted to suit the requirements.

The main process variables are stated below along with a detailed description.

2.2.1. Adhesive behaviour of the slit-tapes

The AFP material is compacted onto the tool surface or the already placed plies. In order for the slit-tapes to stick to the surface without further treatment, the adhesive behaviour of the tapes is employed - so called tack. The behaviour of tack can be characterized in the form of Pressure Sensitive Adhesives (PSAs) [27], as the resin acts as a viscoelastic material. The magnitude of tack is closely related to process temperatures as well as contact time and contact pressure. The tack of the slit-tapes must be sufficiently high to stick to the tool surface. On the other hand, within the delivery chain to the tool surface inside the placement machine tack must be reduced so the tapes do not stick to guiding channels or roller systems. Therefore most industrial AFP machines contain temperature control with active cooling. During placement, the compaction roller presses the tapes to the tool surface. The compaction roller needs to have a release film so the tack between roller and tapes is less than the tack between tapes and tool surface. When the tool surface is treated with a release agent, special care needs to be taken to avoid any rolling up of the tapes on the compaction roller.

2.2.2. Process temperature

A heat source elevates surface temperatures of the tool or already placed substrate in front of the nip point. When the tapes to be placed touch the surface, resin viscosity is reduced and therefore the tack of the material is enhanced. Without sufficient

temperature, the tack level of the material is too low, therefore the material does not stick to the tool surface and the process will fail.

However, temperature must not exceed the material level to avoid premature partial cure or artificial ageing of the material [28].

The complete layup needs to be considered, as every layer gets heated up repeatedly with every pass of the robot. Control of the temperature process window is one of the main challenges of the thermoset AFP.

2.2.3. Contact pressure distribution of the compaction roller

Tack is dependent on contact pressure as well as pressure dwell time, as it acts like a PSA. Therefore, contact pressure needs to be sufficiently high for tack to develop. The deformation behaviour of the compaction roller influences pressure magnitude as well as contact length. The more deformable the compaction roller, the higher contact length as well as lower pressure magnitude.

However, when placing on a honeycomb surface, pressure must not exceed the core crush limit of the honeycomb. When the process does not allow for high compaction pressures, it is possible to substitute pressure with reduced layup rate [27].

2.2.4. Layup rate

In view of material throughput, the layup rate of a specific AFP machine needs to be maximised. However, as tack acts as a PSA, contact dwell time influences tackiness. There is an inverse proportional relationship of layup rate and tack. When the layup rate is reduced, the applied compaction pressure is allowed to act longer on the tapes, therefore increasing contact formation [27].

These are contradictory requirements. For a fast process with high material throughput a high layup rate as high as possible is needed, for a stable process with high tack properties, a as slow as possible process is needed. It is therefore important to optimize the AFP process to a maximum layup rate with sufficiently high tack properties.

2.2.5. Further parameters

The AFP process depends on a variety of process influencing factors, depending on the material choice as well as environmental conditions.

Surface roughness   Tack of the material is, among others, dependent on surface roughness of both contacting partners [29]. Surface roughness influences the degree

of intimate contact as well as the type of bond formation [30]. Further laminate quality aspects,e.g. interlaminar shear stiffness or peel strength also depend on surface roughness of the material.

Tool material The tool material highly influences the mechanical and thermal process behaviour. With the surface roughness of the tool, intimate contact is influenced. Process temperature depends on the magnitude of thermal conduction into the tool material [28]. Emissivity of the tool surface influences the temperature uptake during the first ply. Usually the tool is treated with a release agent or vacuum bag to prepare for layup removal.

Material shelf life Thermoset slit-tapes need to be stored in frozen condition to reduce the polymer bonding reaction. However, the age of the material even under cooled conditions influences its behaviour as well as its tackiness.

Humidity Tack is further depending on the humitiy of the enviroment, as well as the out-time of the material. Further, humidity influences process temperature, with elevated specific heat levels when vapour or water is stored inside the material.
The focus of this study was not on environmental conditions, therefore all further material parameter were assumed to be constant within this study.

2.3. Commercially available AFP simulation software

The AFP process contains many operations, that partly need to be executed simultaneously. Along with the six degrees of freedom of the placement robot come cut and restart operations, control of the heat source and the application of the compaction force. Therefore, online programming of the robot, so called teaching, is not feasible concerning AFP. In conclusion, offline programming software for the AFP process needs to be utilised.
Most manufacturer of AFP machines offer commercial offline programming software. Additionally there are some AFP specific software available that offer machine independent programming possibilities. Table 2.1 sums up commercially available software tools alongside the AFP equipment manufacturer. The software tools are either stand alone or implemented in a CAx software environment.

All above mentioned software employ a pure kinematic approach for offline programming and offline simulation. Therefore, the software allow for collision avoidance and kinematic evaluation of gaps, overlaps and steering radii. However, neither process variables nor material behaviour are considered.

Manufacturer Placement Head	Software manufacturer	Software-Name
Automated Dynamics	Automated Dynamics	FPM, FPS
Broetje Automation	Broetje Automation	Soul
CGTech/ AFPT/ Electroimpact	CGTech	VERICUT
Coriolis Composites	Coriolis Composites	CADFiber, CATFiber
Ingersoll	Ingersoll	iCPS
MAG	MAG	ACES
Mikrosam	Mikrosam	MikroPlace
-	Siemens	Fibersim

Table 2.1. Compendium of commercially available software packages for kinematic offline analysis of the AFP process

The usual workflow of the offline programming of an AFP layup may be summarized in following steps:

1. Tool surface definition with either geometry or mesh based approach

2. Defining guide curves

3. Ply-boundary definition

4. Layup evaluation

5. Kinematic simulation

6. NC output

Therefore it must be concluded that a pure kinematic simulation allows to manage for the AFP robot to complete the programmed course without collision. However, to accurately predict the material behaviour and the influence of process variables like compaction pressure or layup rate, models with higher details need to be developed.

2.4. Conclusion and motivation for this work

The APF process is well established in the aerospace industry, and is now advancing towards automotive [31]. For an industrial scale AFP process, feasibility and process parameters are determined through trial-and-error. In commercially available software packages, regulation of the power output, and therefore the process temperature, is usually solely dependent on the kinematics of the placement head and is independent of tool or slit-tape material properties. When considering multi-material toolings, e.g. the aforementioned combination aluminium-honeycomb, heat output of the heat source is not regulated, leading to highly irregular process temperatures. Further, layup rate as well as compaction force along with the deformation behaviour of the compaction roller is determined empirically, leaving room for im-

provement at productivity and material throughput. Multiple curved surfaces are considered kinematically, leaving out the deformation behaviour of the compaction roller. Therefore, emerging defects like bridging are not detected a priori and increase the cost of the process.

Therefore, to reduce this gap in design, simulation models as well as process studies are conducted within this study to gain understanding of the AFP process regarding the process parameters tack of the material, thermal input during the process as well as the layup speed.

From the kinematic input of an industrial offline programming software for AFP and the applied compaction force of the robot actuator, the deformation behaviour of the compaction roller was determined experimentally and simulative. Depending on layup rate and heat output of the heat source process temperature are measured and compared to simulation results. With the knowledge of the key parameters temperature, compaction pressure and layup rate a model is developed for the characterisation of prepreg tack under AFP conditions.

3. Kinematic and mechanical analysis of the AFP process

To utilize AFP's strong potential on multiple-curved surfaces such as tapered sandwich structures, it is important to analyse and control emerging effects like gaps, bridging, and non-geodesic steering. An analytical relationship between path generation and effects of the AFP manufacture of tapered sandwich structures was found with good agreement to experimental tests. The deformation behaviour of an industrially used compaction roller has been analysed numerically and experimentally. The results show a non-uniform deformation behaviour on flat and curved surfaces and the limited deformability of the compaction roller.

Further, the compaction behaviour of an aerospace grade toughened prepreg was experimentally studied under AFP process conditions. The results show that the slit-tapes may experience significant reduction in thickness during layup.

3.1. Literature review

3.1.1. Open contoured multiple curved surfaces

Specific parts like honeycomb sandwich structures with high strength-to-weight and stiffness-to-weight ratios are well understood [32] and are well established. Recent developments show the advantages of tapered sandwich structures. Oster [33] describes a combination of monolithic and CFRP / Nomex honeycomb construction resulting in especially light and stiff CFRP cells in helicopters. The effects of the manufacturing procedure on fracture mechanisms of tapered sandwich structures are studied by Di Bella et al. [34]. The high performance of asymmetrical sandwich structures was demonstrated by Castanié et al. [35] in experimental and theoretical analysis. They found asymmetric sandwich structures to be extremely resistant to static shear / compression tests [36].

The AFP process is well-established for the manufacture of flat or single-curved surfaces. For the combination of tapered sandwich structures with the benefits of the AFP process, little work is available. To utilize AFP's strong potential to deposit fibres on complex curvature surfaces such as tapered honeycomb sandwich structures or steer the slit-tapes along a load path, it is important to analyse and control emerging defects like gaps, overlaps and bridging. Paris et al. [37] describe the failure mechanisms of AFP manufactured sandwich ramps under tensile loading, however they do not go into detail about the manufacturing procedures. Offline tra-

jectory programming is still an area of ongoing research, although Shirinzadeh and
co-workers [38–40] studied different path-planning algorithms for the AFP process
in detail. Usually a point-cloud or mesh-based system is utilized for the path gener-
ation on the tool surface. Blom et al. [41] defines different path-generation methods
for an analytically defined surface. In most cases path-generation algorithms work
under the assumption of a differentiable surface, e.g. smooth surface without kinks.
Lichtinger et al. [42] study the effects of gaps and bridging on tapered honeycombs,
including the deformation behaviour of an industrial compaction roller as well as
emerging gaps between two courses on a ramped structure.

3.1.2. Roller deformation

Another important factor is the compaction device of the AFP head. Schledjew-
ski [43] stated the importance of the orientation of the compaction roller. With a
deviation of 3 % from the normal vector the peel force reduced considerably when
using a rigid compaction roller. Therefore it is imperative to use a conformable com-
paction device on multiple curved surfaces. Usually the conformable behaviour is
achieved using a soft silicone roller [3]. Crossley et al. [44] stated a direct relation-
ship between compaction pressure and tack of thermoset prepreg. Lichtinger et al.
[29] proposed a theoretical relationship between normal pressure, contact time and
tack properties of slit-tapes. Therefore an AFP compaction roller has to conform to
the tool surface as well as apply sufficient normal pressure. This especially applies
for concave tool geometries, as insufficient tack will lead to the bridging of the slit-
tapes between two contact points. On the other hand the normal pressure of the
compaction roller must not exceed the core crush limit of a honeycomb structure [45].
This leaves a specific process window for compaction force and roller deformation
behaviour.
One of the first to take the pressure distribution underneath a compaction roller
for AFP processes into account was Helenon et al. [46]. They modelled part of an
industrial scale compaction roller using a linear FEM approach with a isotropic ho-
mogeneous material model based on compression testing. Lichtinger et al. [42] fully
tested an industrial scale compaction roller manufactured by *Coriolis Composites*
and developed an orthotropic material model using FEM.

3.1.3. Compaction of prepregs

During the placement of the slit-tapes, the compaction roller applies pressure as well
as heat input so the adhesive behaviour is enhanced and the slit-tapes stick to the
tool surface or the already deposited substrate. State of the art toughened prepreg

material usually are partially impregnated to allow for channels so entrapped gas can escape during evacuation [30]. With the application of pressure and heat, resin will flow through thickness to fully impregnate the slit-tapes. Therefore a reduction in thickness is involved during compaction. Springer [47] studied resin flow during cure experimentally and compared obtained data to the Springer-Loos model [48]. Davé et al. described resin flow during composite processing analytically [49] and numerically [50]. The model is based on a theory of consolidation and flow through a porous medium, based on Darcy's law [51]. Smith and Poursartip [52] compared two well established models based on viscous flow through porous media. They found that the fibre bed carries some of the applied pressure, and the fibre bed compaction is one of the key parameters during processing.

Gutowski et al. [53] modelled the fibre bed compaction including viscous flow of resin, and validated their model with experiments [54]. Cai and Gutowski [55] developed their theory further to a general behaviour of fibres impregnated with a viscous fluid. They found both the viscous as well as the elastic behaviour of the fibre bundles shift their proportional values during compaction. Lekakou et al. [56] apply Gutowskis model to a woven fabric, and transfer the results to a macro-scale model.

A full compaction curve is directly measured by Hubert and Poursartip [57]. They introduce a simple setup for experiments on UD and quasi-isotropic prepregs. Gu et al. [58] study the compaction of toughened prepregs experimentally and apply the squeezed sponge model to their experimental value. They found a highly uneven distribution of consolidation through thickness. Comas-Cardona et al. [59] introduce permanent deformations in the form of plasticity during compaction. They apply a geometrically non-linear FEM model to both dry fabrics and pre impregnated fibres of compaction experiments. Li et al. [60] introduce a simple method for compaction measurements including permeability predictions, and fit their experimental values to Gutowskis compaction model. Hubert et al. [61] developed a flow and compaction model for complex shape composites during cure in an autoclave. They found that the fibre bed permeability and resin viscosity affects the compaction rate of the laminate, while the fibre bed shear modulus dominates the compaction behaviour in corner sections of curved laminates.

Creep recovery and relaxation was studied by Guedes et al. [62] for CFRP material. They model the material response with the Schapery equation, approximated with a Prony's series.

In AFP, after compaction, the pressure is removed and the slit-tapes have time to recover from the compaction. All models mentioned above consider long time scale behaviour, counted in minutes and hours, while the AFP specific boundary conditions vary in seconds and milliseconds. Further, main focus of literature is on compaction, while recovery also plays an important role during automated layup.

It is presumed that the slit-tapes exhibit non-linear viscoelastic behaviour through-thickness. Within a lubricated fibre bundle the embedded fibres may not be assumed to be straight, but will exhibit a slight curvature, compare Cai and Gutowski [55]. From point of application of compaction pressure, the slightly curved fibres are straightened, resulting in an elastic pre-stress of the fibre bundle. Additionally, the resin flows viscously in all directions. With the applied pressure, voids within the fibre bundle may reduce. After the pressure is released, the pre-stressed fibres induce a thickness increase of the fibre bundles, constricted by the viscous resin.

Various studies were performed concerning consolidation with AFP specific boundary conditions. Pitchumani et al. [63] study void dynamics including consolidation in the thermoplastic AFP process. They found that increased compaction pressure results in reduced final void content. They further concluded that forced cooling after passing of the placement head may be necessary for parts with low void content. Gangloff et al. [64] model a tow unit cell that determines the consolidation and impregnation of a thermoset prepreg tape under an input pressure profile. Their results show a non-linear relationship between layup velocity and compaction force on tow consolidation. Lukaszewicz and Potter [65] model the through-thickness compression response of uncured thermoset prepregs with a viscoelastic material model compared against an elastic-plastic material behaviour. They found a simple strain hardening material model can be used to accurately model the compression response during automated layup.

There is little work available to gain insight into the compression response of thermoset prepreg material under AFP specific boundary conditions. Therefore the current study experimentally determines the compression - recovery response cycle for repeated short term compressive boundary conditions under elevated temperatures.

3.2. Kinematics for discrete open contoured surfaces

With the AFP specific operations, e.g. cut-and-restart operations, control of the compaction pressure or control of the heat output of the IR lamp, a manual teaching of the operations is no longer feasible. Therefore, the complex robot movement is programmed offline alongside the AFP specific operations.

The preoperative planning of the paths is the basis for the complete process. For an optimal laminate quality, it is imperative to plan the fibre placement paths according to layup strategy as well as process restrictions. For a multiple-curved surface, like a tapered honeycomb structure, geodesic paths without deviations from the intended design are no longer possible. Different path planning strategies are able to account for the avoidance of varying effects such as gaps, overlaps or multiple ply drop-offs. However one needs to be aware of some subsequent restrictions to the process.

The offline programming software has a wide influence on the later laminate quality. Commercially available software solutions for the AFP process are able to account for some defects, e.g. gaps and overlaps. However, non of the available software (compare Table 2.1 in Chapter 2) can include all defects resulting from multiple curved surfaces. All commercial software share the closed-source character. It is not possible for the user to comprehend the actual procedure of the path planning, and has to trust and agree with the placement procedure with only limited possibilities of intervention. Lichtinger et al. [42] state that depending on mesh quality and the quality of the path planning algorithms, it is possible for singularities of the robot to emerge. This can lead to small steering radii locally or even a rapid movement of the robot.

The path generation usually is mesh or surface based. From a starting point, a guide curve, i.e. a path direction is defined. Depending on the path planning strategy for multiple curved surfaces, there are numerous possibilities for an initial path, e.g. a globally straight path, or a geodesic path. For a projected globally straight direction the path angle is fixed and all steering effects due to the surface curvature is ignored. Geodesic paths have no in-plane steering, and follow the shortest distance possible between two points on a curved surface.

3.2.1. Gaps and steering effects

In the current study on the placement on a tapered honeycomb structure, a compromise has to be found between gaps, overlaps and steering radii at the edges of the discrete ramp. For a multiple curved surface it is not possible to reach full coverage without the possibility of adapting tape width [66]. However for industrial scale AFP processes this is not possible. Therefore design restrictions apply.

In the case of a tapered honeycomb (compare Figure 3.1), to complete full coverage either steering is necessary, a deviation from the planned fibre angle, or a sectorisation of the surface.

3.2.1.1. Analytical considerations

For the discrete case of a ramped structure, including the two discontinuities of the edges, analytical calculations can be undertaken to accurately predict the emerging gap and the theoretical steering angle, or the fibre deviation from the set fibre angle at the ramp. These considerations are explained in the following.

Constant angle paths   On the basis of globally straight paths projected from the top, it is apparent that there are discontinuities at the edges of the ramp. Looking
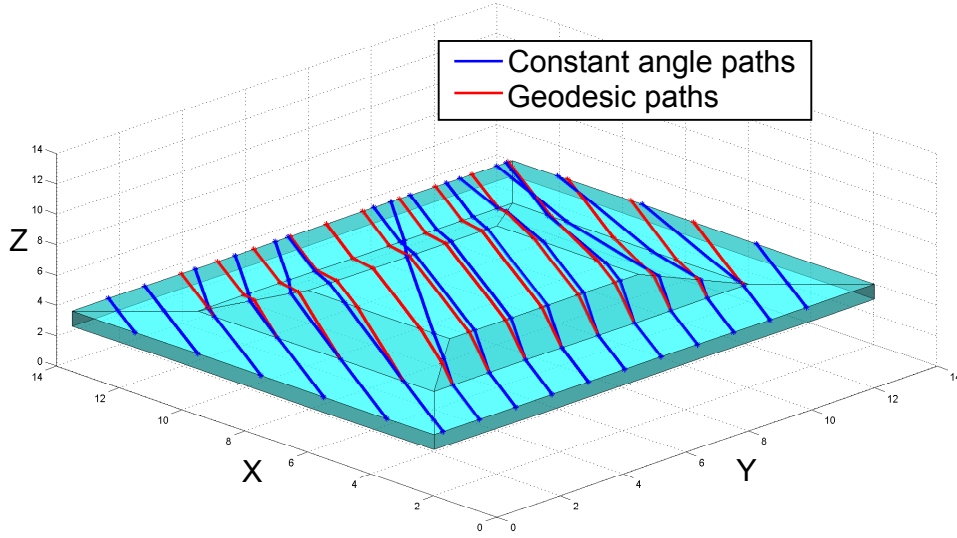
Figure 3.1. Tapered honeycomb on a flat surface with constant angle paths and geodesic paths

at the flat projection of the surface, depicted in Figure 3.2, distinct kinks in the path are visible, resulting in theoretical in-plane steering angles. This is required to maintain constant path angles.

In the discrete case such as as edges of a ramp, a theoretical steering angle (γ) is needed and can be calculated as a function of path angle and ramp angle displayed in Equation 3.1:

$$\gamma\left(\alpha, \theta\right) = acos\left(\frac{\frac{sin\alpha}{sin\theta} + \frac{cos\alpha}{tan\theta \cdot \tan\alpha}}{\left(csc^2\alpha + cot^2\theta \cdot cot^2\alpha\right)^{0.5}}\right) \tag{3.1}$$

An instantaneous steering angle is impractical, as this would induce wrinkles and kinks of the slit-tapes at the point of the direction change.

Furthermore, as also shown in Figure 3.2, due to the nature of the combination of the constant angle paths with the curved surface, the distances between two paths deviates at the ramp. There is a defined analytical relation between path angle (α), ramp angle (θ), and distance between two paths (w_1). The resulting gap, $g = w_2 - w_1$, is depicted in Equation 3.2:

$$g\left(\alpha, \gamma, w_1\right) = w_1 \cdot \left(\frac{\left(cot^2\alpha \cdot cot^2\theta + csc^2\theta\right)^{0.5}}{sin\alpha \cdot sin\theta + csc\alpha \cdot cos\theta \cdot cot\theta} - 1\right) \tag{3.2}$$

With above Equation 3.2 the gap between each path of the placement courses can be calculated, as well as the width of the sum of all gaps along a ramp.
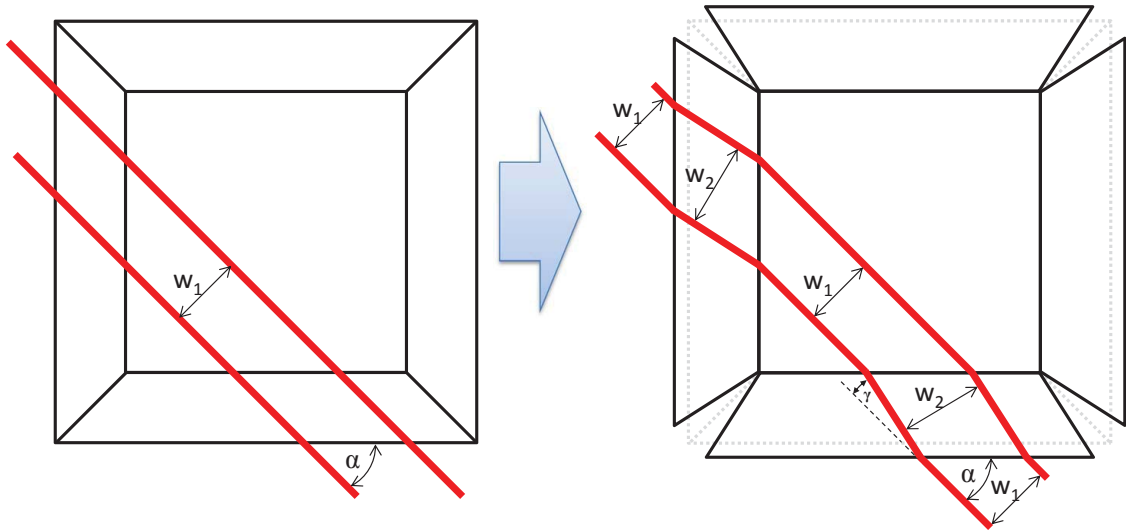
Figure 3.2. Projected path for constant angle paths on a ramped structure (left) with the flat projection (right), compare Lichtinger et al. [42].

Geodesic paths   When considering geodesic trajectories on a multiple curved surface, a certain deviation from fibre angle has to be taken into account at the ramp, as well as a parallel offset of parallel planes.
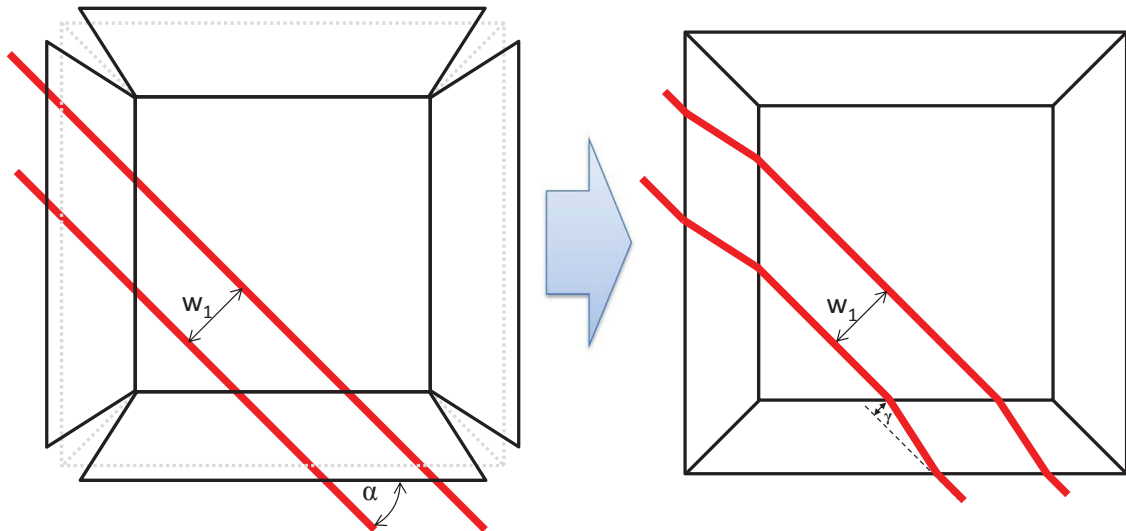
Figure 3.3. Projected path for geodesic paths on a ramped structure (right) with the flat projection (left), as depicted in Lichtinger et al. [42].

Equation 3.1 can be used to calculate the fibre deviation. The defined parallel offset from the original path at the top of the ramp and all further offsets can be calculated with the steering angle ($\gamma = f(\alpha, \theta)$) and the path length l_r on the inclined plane:

$$o_g = l_r \cdot sin\gamma \tag{3.3}$$

where $l_r = \left(\left(\frac{h}{tan\theta} \right)^2 + \left(\frac{h}{sin\theta \cdot tan\alpha} \right)^2 + h^2 \right)^{0.5}$.

3.2.1.2. Experimental analysis of gaps

Tests were conducted using a *Coriolis Composites* fibre placement machine with the capability of simultaneously placing eight slit-tapes with 6.35 mm width each. The tool layout is pictured in Figure 3.4 with a ramp height (h) of 15 mm.
The experimental procedure consisted of the placement of two constant angle paths with eight slit-tapes each. Varying parameters were path angle in relation to the ramp edge as well as ramp angle.
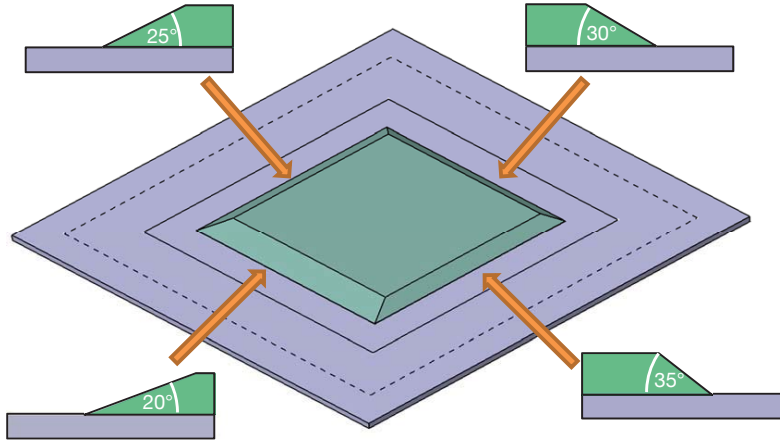
Figure 3.4. Layout of the tool for the testing of gaps, compare Lichtinger et al. [42]

To gain some insight into variability, three repeats of each test were undertaken with same test conditions. The path generation was conducted using the mesh-based commercial Software *CATFiber* distributed by *Coriolis Composites*. The test results were analysed using image analysis. Test parameters analysed are presented in Figure 3.5 and Table 3.1.
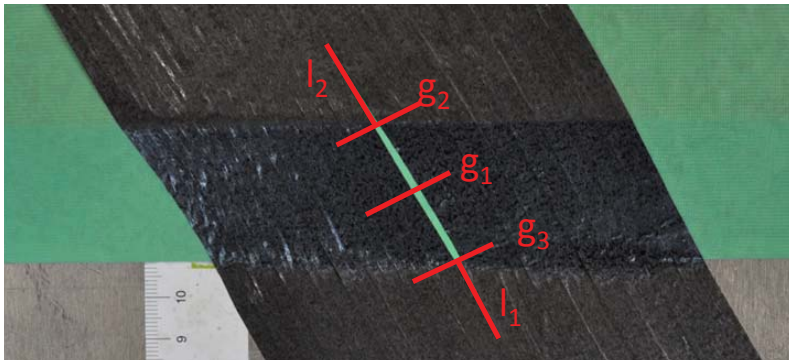
Figure 3.5. Evaluated results of the experimental testing of gaps [42].

l_1	Gap length at bottom plane
l_2	Gap length at top plane
g_1	Gap width at ramp centre
g_2	Gap width at the top of the ramp
g_3	Gap width at the bottom of the ramp

Table 3.1. Testing of gaps: evaluated test results [42]

3.2.1.3. Analytical and experimental results

Figure 3.6 and shows the analytical gap width g_1 at the ramp as function of path angle α for the four tested ramp angles. The gap width starts off a plateau, the magnitude depending on the ramp angle. The gap size reduces non-linearly as the path angle rises. As α approaches a right angle towards the ramp edge, the gap converges towards zero. The curvature of the graph changes with α from a positive inflexion to a negative one. It is worth noting that with $\lim\limits_{\theta,\alpha \to \infty} g_1 :\to \infty$.
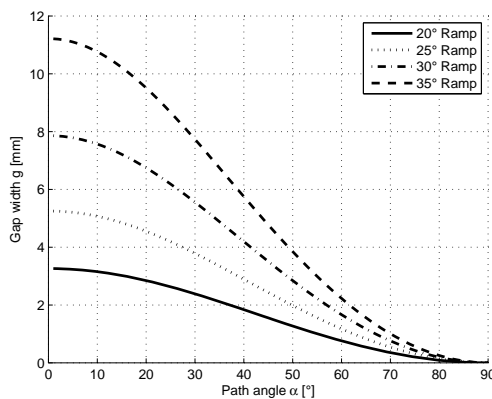
Figure 3.6. Resulting gap width g_1 as a function of path angle for different ramp angles [42].
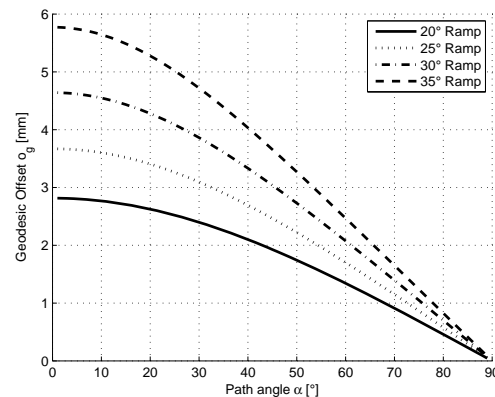
Figure 3.7. Parallel offset due to geodesic path generation [42]

The parallel offset of the geodesic paths start with a plateau, as depicted in Figure 3.7, depending on the ramp angle. With advancing path angle the geodesic offset drops, and reaches a close to linear behaviour for path angles above 45°. As expected the geodesic offset for 0° path angles is zero for all ramp angles.

Figure 3.8 shows the analytical gap width g_1 compared to experimental results. Results show similarities in shape in general, but the comparison suggests that further effects influence the placement process that is not captured with the model assumptions.

At path angles below 50° the gap widths are over predicted by the analytical model. The reason for that is that at the experiments at low path angles gaps started to emerge between the individual tapes, and not just between the two paths. The whole
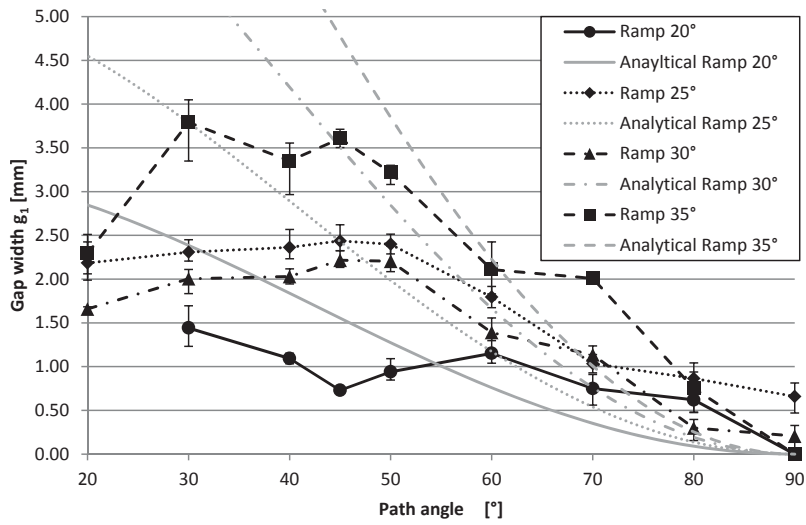
Figure 3.8. Gap width analytical results compared to experimental values

process started to fail and uncontrolled gaps and overlaps appeared, along with tape wrinkling and bridging effects. Figure 3.9 depicts the placement on a 30° ramp at a path angle of 30°. The distinct gap between both paths are visible, along with smaller gaps between each tapes. It is worth noting that experimental values for gaps at 25° ramp angles are constantly above the gaps of 30° ramp angles. This directly contradicts the analytical prediction, and is presumed to originate from the mesh dependent path algorithm.
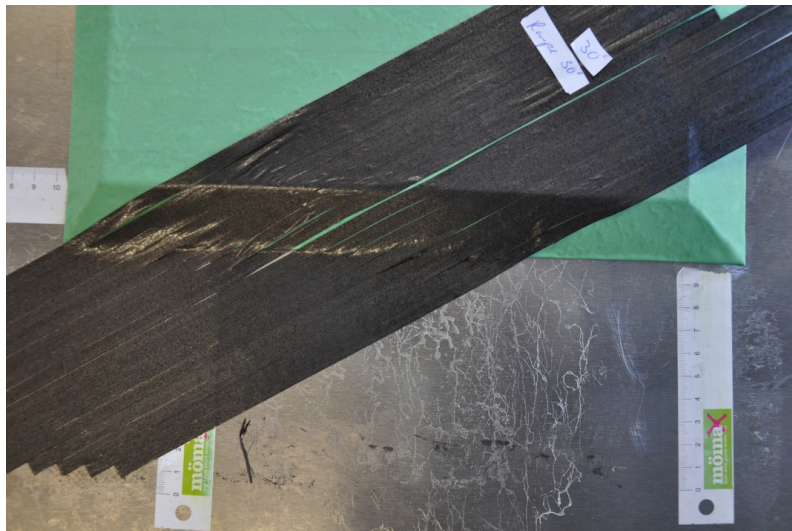
Figure 3.9. Emerging gaps at ramp angle 30° and a path angle of 30°

Figures 3.10-3.11 show the resulting gap width at the top of the ramp and at the bottom of the ramp, g_2 and g_3 respectively. For all ramp angles at 90° path angles no gaps are visible. With declining path angles the gaps are expanding.

However, there is no distinct correlation between path angles and ramp angles. g_2 start to reduce at path angles smaller than 50° for ramps of 20°, 30° and 35° angle.

This is contrary to expected results, and is assumed to be correlated to the mesh dependency of the path planning algorithm, detailed in Lichtinger et al. [42].
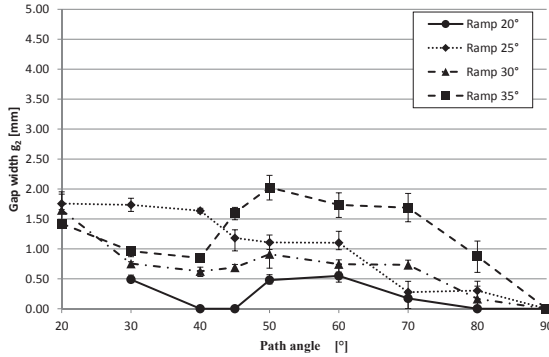
Figure 3.10. Experimental gap width g_2 at the top of the ramp [42]
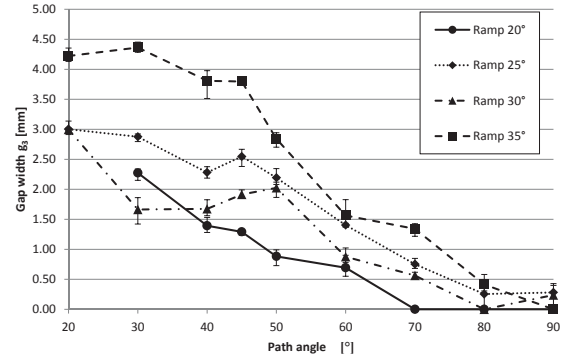
Figure 3.11. Experimental gap width g_3 at the bottom of the ramp [42]
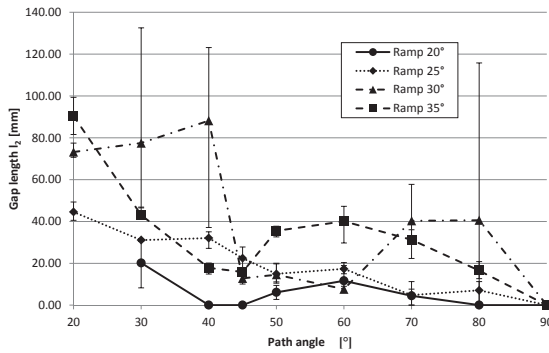
Figure 3.12. Experimental gap length l_2 at the top plane [42]
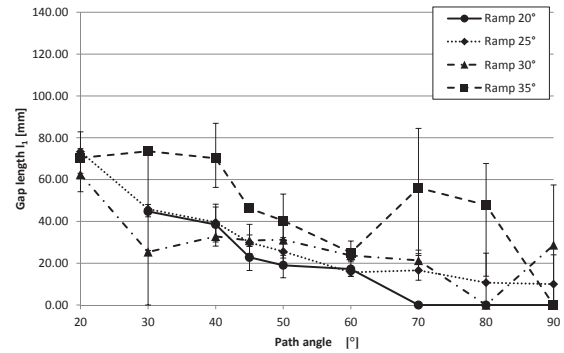
Figure 3.13. Experimental gap length l_1 at the bottom plane [42]

Gap length at the top plane and the bottom plane, compare Figures 3.12 and 3.13, show high variance. This is evidence that for the placement on multiple curved surfaces, the placement tolerances need to be closely monitored, and are subject to big variations.

3.2.2. Optimization of the placement paths

The analytical considerations of the path planning of Section 3.2.1.1 were used to design an optimization tool to reduce gap and overlap size. A discrete surface was partitioned into triangles or rectangles, and a path optimisation algorithm was performed, each path depending on its neighbour. The starting path was a constant angle path. Figure 3.14 depicts the optimization procedure. On the edge of every partition, the distance to the neighbouring path is evaluated, and the path point is moved along the edge of the partition to close gaps or omit overlaps. A further boundary condition is a minimum steering radius, which is calculated with the flat projection of the two path segments.
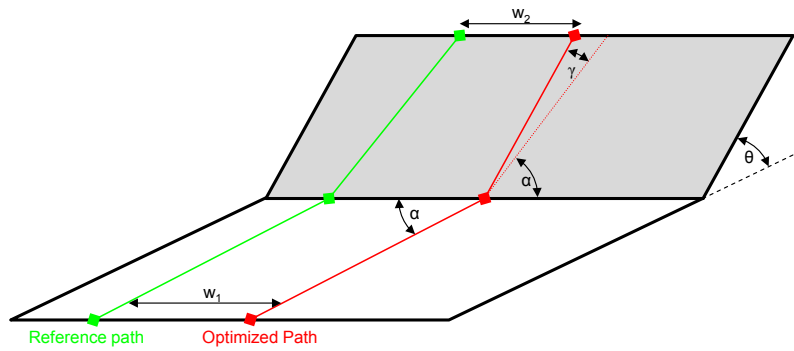
Figure 3.14. Path optimization procedure

For an optimized path, a error criterion ϵ is minimized, which applies a weighting function *weight* between emerging gaps / overlaps and minimum steering radius with Equation 3.4:

$$\epsilon = weight \cdot \frac{|g|}{g_{max}} + (1 - weight) \cdot \frac{\gamma_{min}}{gamma} \tag{3.4}$$

with $weight \in [0; 1]$.

With the optimization algorithm a further effect during the placement process is visible, which we called "Dancing of the Robot".
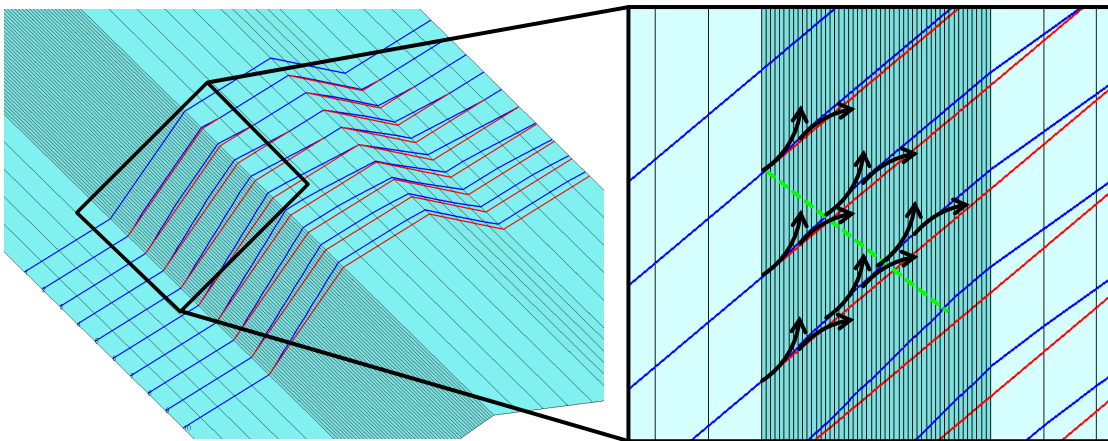
Figure 3.15. Curvature of the paths due to gap optimization

During preliminary placement experiments with active gap optimization of the path planning algorithm, the robot rotated visibly back and forth around its vertical axis, therefore creating wrinkles in the tapes.

This "dancing", i.e. the rotation about the vertical axis of the robot, is due to the gap optimization algorithm. Figure 3.15 shows the path planning behind the gap optimization.

The gap can only be closed with in-plane steering. With the input of maximum steering radius, the placement head runs through a wave motion. Starting tangen-

tial to the original path, on the ramped section the path deviates to close the gap, changing the steering curvature from negative steering radius to positive steering radius.

With progressing amount of paths, also the amount of waves rise, as each wave aggravate with progressing path number. The optimization algorithm always measures perpendicular to the current path section, therefore accumulating the waviness of the pass indefinitely with number of paths, or until the end of the ramp is reached.

3.2.3. Discussion of kinematic effects

The kinematic path planning of the robot is the basic requirement for any AFP process. Without offline programming, the complete placement process in infeasible to execute. With the complex translational and rotational DoFs of the robot it is imperative to know the exact movement of the robot to avoid collisions. Control of the IR lamp or cut-and-restart actions also need to be programmed beforehand, and cannot be conducted on-line.

However, most of these functions are state of the art in commercially available path planning software. The effects of the complex movement of the robot need to be understood by the operator, as well as the layup design. Especially when an optimization is involved in the path planning algorithm, the resulting movement of the robot may counteract the benefits of described optimization.

3.3. Influence of the compaction roller

The deformation behaviour of the compaction roller has major influence on the AFP process. Especially for the placement on multiple curved surfaces, the roller needs to conform to the surface to supply sufficient normal pressure. Insufficient contact pressure will lead to the bridging of the slit-tapes between two contact points on a concave surface. However, the normal pressure of the compaction roller must not exceed the core crush limit of a honeycomb structure [45]. This leaves a specific process window for compaction force and roller deformation behaviour.

Usually the conformable behaviour is achieved using a soft silicone roller [3]. In the current study a individual compaction roller from *Coriolis Composites SAS* with the label *8F14-M510* is used (Figure 3.16).

The roller consists of a coiled thermoset foam material bonded around an axis with a release coating in the form of a shrink tube. The dimensions of the roller are summarized in Table 3.2.

It is mounted to the placement head, and rotates freely around its centre axis. The rotation originates solely from frictional forces, when the AFP head presses the roller
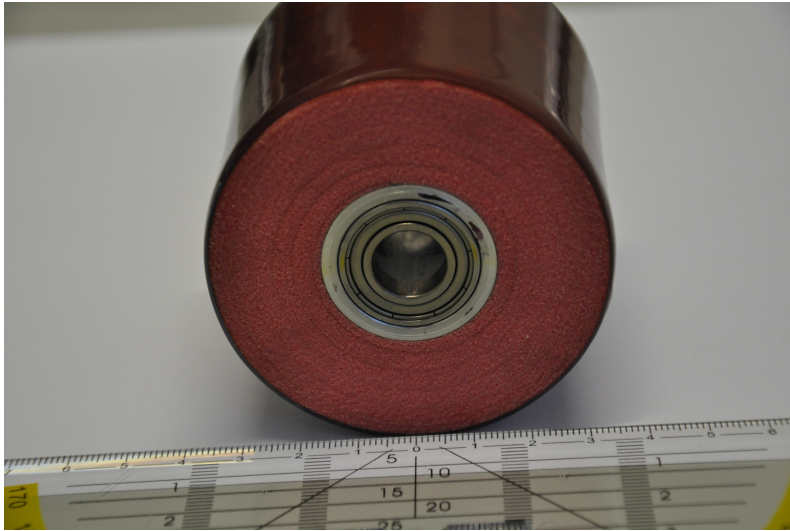
Figure 3.16. *Coriolis Composites* compaction roller for $8 \times 1/4$ inches slit-tapes [42].

against the surface, and then moves along its path. Inside the roller ball bearings are installed to reduce frictional losses.

Table 3.2. Dimensions of the Coriolis Composites Compaction Roller [42]

Roller inner diameter	30.0 mm
Roller outer diameter	68.3 mm
Thickness of the release coating	0.8 mm

3.3.1. Hertzian deformation considerations

One of the major influencing factors of the AFP process is the pressure distribution under the compaction roller as well as its deformability. Without sufficient pressure there is the risk of process failure due to the absence of tack. Further, when the roller does not conform to a concave surface, the tapes will bridge the resulting gap. With the compaction force as a process parameter, the roller deforms depending on:

- Roller material and roller design

- Surface deformability

- Surface Geometry

Hertz [67] developed a theory in 1882 which is the basis of all further contact mechanics theories. The Hertz theory focuses on the normal contact of two homogeneous isotropic elastic bodies with small deformations.

Considering general deformable compaction rollers under the assumption of Hertzian contact [67], the deformation of the compaction roller on a rigid flat surface is [68]:

$$\overline{u}_z = -\frac{2}{\pi E^*} \int_{x_{min}}^{x_{max}} \int_{-a}^{a} \frac{p(s)}{x-s} \, ds \, dx. \tag{3.5}$$

with $E^* = \frac{E_{roller}}{1-\nu_{roller}^2}$, assuming a rigid tool surface, with E_{roller} as the elastic modulus of the roller and ν_{roller} as its Possion's ratio.

Peak magnitude of pressure is in the centre of the contact area, exactly underneath the roller axis. The pressure reduces quadratically to the edge of contact area with zero pressure, using set of Equations 3.6a and 3.6b. The total load compressing the solid F is related to contact area a by

$$F = \frac{\pi a^2 E^*}{4R}, \tag{3.6a}$$

with R the roller radius. With the contact area, the pressure distribution in relation to location can be determined:

$$p(x) = \frac{2F}{\pi a^2} \left(a^2 - x^2\right)^{1/2}. \tag{3.6b}$$

With above mentioned restrictions, it is possible to calculate the pressure distribution underneath a homogeneous compaction roller.

Figure 3.17 depicts the theoretical roller indentation under the assumption of Hertzian deformation, as well as the resulting pressure distribution for a deformable roller and rigid flat surface.
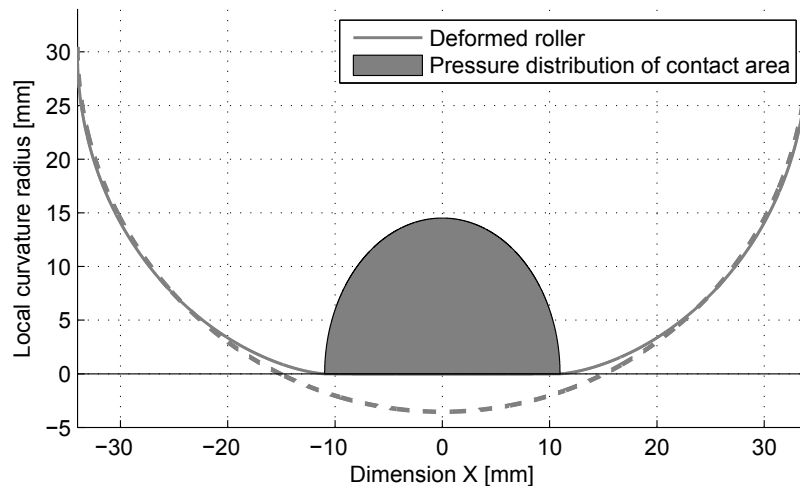
Figure 3.17. Indentation of a roller cross section according to Hertzian theory, along with the pressure distribution

Usually an industrial scale roller has a complex design with a combination of multiple materials, therefore Hertzian contact mechanics cannot be applied. In the following Section the deformability of an industrial compaction roller is studied.

3.3.2. Experimental determination of the deformation and pressure distribution of an industrial AFP compaction roller

The industrial scale roller used within the tests was a customised coiled thermoset foam bonded around an axis with a release coating at the outer surface. With the inhomogenious design, Hertzian assumptions of Section 3.3.1 cannot be applied.
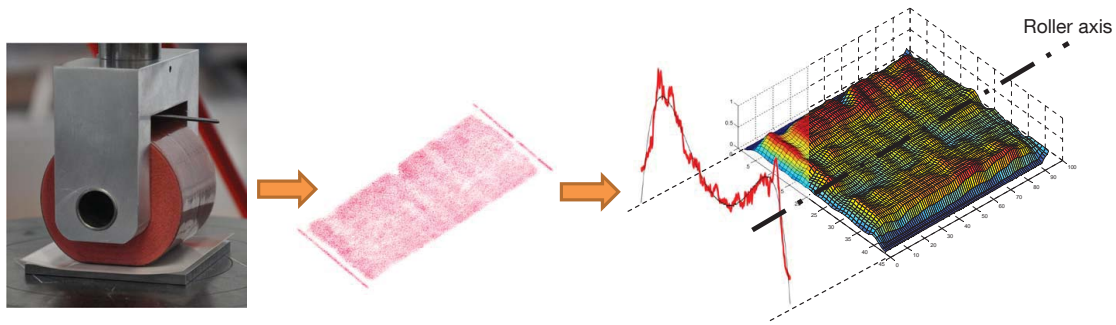
Figure 3.18. Pressure evaluation procedure, compare Lichtinger et al.[42]

With the thermoset foam and the inhomogeneous design the deformation as well as the pressure distribution under the area of contact is different from Hertzian theory. Below the industrial AFP roller manufactures by *Coriolis Composites* was characterized for different surface geometries. Figure 3.18 shows the testing procedure of the pressure distribution of the compaction roller on a flat surface. Between tool and roller a pressure sensitive film (*Prescale by FUJIFILM* [69]) was inserted, and the resulting colour distribution was evaluated using image analysis.

3.3.2.1. Test setup

To analyse the compaction roller statically it was mounted on a universal testing machine. Then the roller was pressed against different tools. The tests are clustered into five different setups:

1. Flat tool surface with roller force parallel to area normal
   "Flat tool"

2. Convex tool surface with roller axis perpendicular to apex
   "Convex tool lateral"

3. Convex tool surface with roller axis parallel to apex
   "Convex tool longitudinal"

4. Concave tool surface with roller axis perpendicular to edge
   "Concave tool lateral"

5. Concave tool surface with roller axis parallel to edge
   "Concave tool longitudinal"

Figure 3.19 shows the five different test scenarios with three different tool designs on which static compression tests were performed. Dynamic effects of the roller were neglected. The tool geometry (the angle of the concave and convex tool as well as the radii) was designed to be comparable to the honeycomb surface discussed in Section 3.2.1.3.
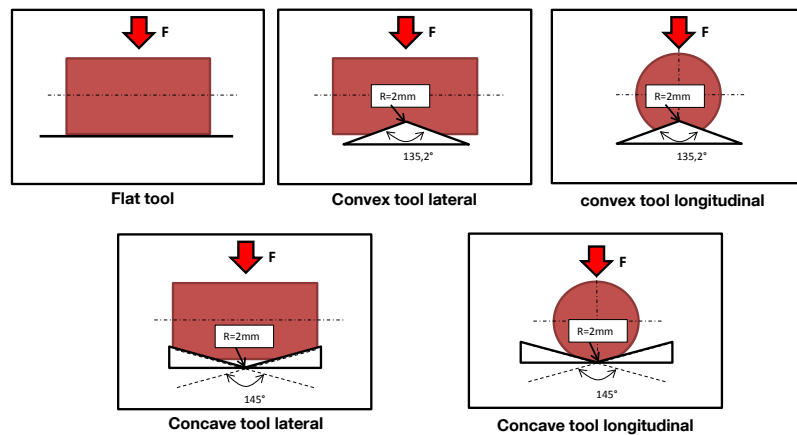
Figure 3.19. Five different test scenarios with three tool designs for static roller tests, according to Lichtinger et al. [42]

Table 3.3 presents the applied compaction forces for each scenario. To avoid damaging of the compaction roller the maximum force was not applied at certain test configurations. Tests with too little contact area, and therefore negligible results, were omitted.

Table 3.3. Test Setup with applied compaction forces

Test Setup	Applied Compaction Forces
1: Flat tool	250 N, 500 N, 750 N
2: Convex tool lateral	250 N
3: Convex tool longitudinal	500 N
4: Concave tool lateral	250 N, 500 N
5: Concave tool longitudinal	250 N, 500 N, 750 N

Five repeats of each test were undertaken to gain insight into the variability. The force-controlled displacement of the universal testing machine during each test cycle was marginal, so time-dependent behaviour of the roller was assumed to be negligible.

3.3.2.2. Image analysis of the pressure sensitive film

The *Prescale* pressure sensitive film varies colour according to the intensity of the normal pressure. The pressure application time is specified in the documentation [70] with 120 s per test.

Figure 3.20 depicts the evaluation procedure. The colour density of the *Prescale* pressure tests are compared to the colour density scale of the manual [70] to get the correct pressure values.

The coloured film was scanned to get a digital image. The colour density of the image than was analysed using a MatLab routine, and evaluated accordingly with the density scale of the manual.
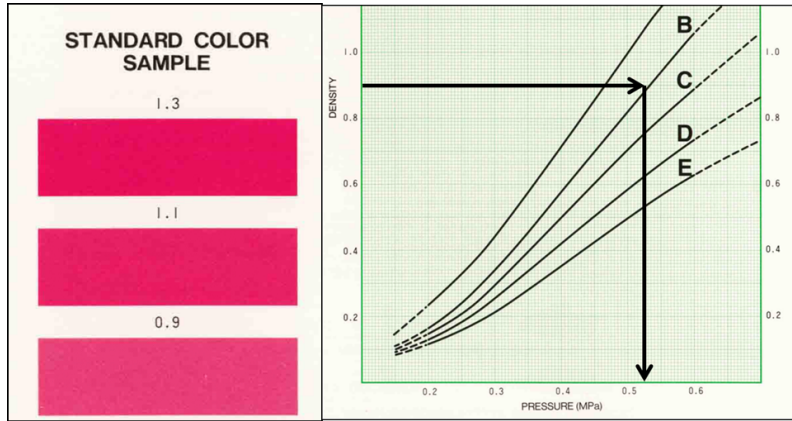
Figure 3.20. Evaluation procedure of the *FUJIFILM Prescale* pressure sensitive film [70]

As the colour distribution of the scanned image was inhomogeneous, the pressure values had to be smoothed using MatLab internal smoothing algorithms. Figure 3.21 shows an evaluated pressure distribution before and after smoothing.
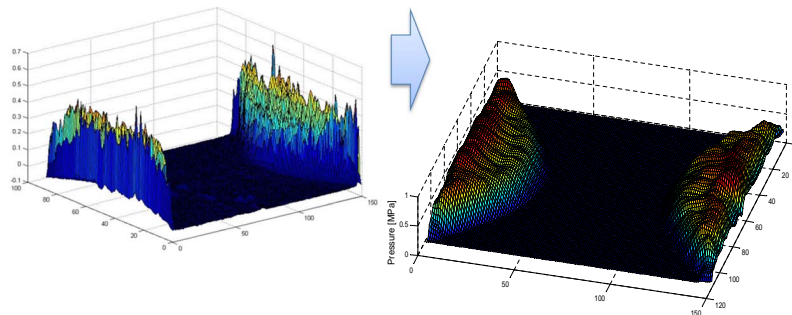
Figure 3.21. Evaluated image of the Prescale results of Test setup 5 (Concave tool lateral) before (l) and after (r) application of the smoothing algorithm

The complete resulting pressure was integrated over both dimensions of the image to gain the resulting compaction force according to Equation 3.7:

$$F_{PS} = \int_A p dA. \tag{3.7}$$

The resulting force F_{PS} was then compared to known compression force F_{TM} set on the universal testing machine, and a correction factor p_{corr} for the pressure was introduced with $p_{corr} = \frac{F_{TM}}{F_{PS}}$ and applied accordingly with Equation 3.8:

$$p_{real} = p_{corr} \cdot p. \tag{3.8}$$

However, with the integration of the pressure and the correction factor p_{corr}, there is the possibility of error due to the fact that there is a maximum measurable pressure. When the maximum measurable pressure is exceeded, the pressure sensitive film is coloured all red, therefore not allowing for any higher pressure to be detected. Subsequently, the global scale factor will affect all other measured results.
The assignment from colour density to pressure was interpolated pointwise linearly. The colour density scale was extrapolated linearly above and below the individual limits to gain insight into lower and higher pressure magnitudes.

3.3.3. Simulation of an industrial compaction roller

With the complex design of the roller it is impractical to model the roller in such detail. The numerical cost would have surmounted the acquired results. Therefore the intention was to get a analogous model that has the same normal pressure behaviour than the real compaction roller.
Based on the static experimental results, an FEM model was designed to reflect the compaction roller's behaviour using the commercial software Abaqus CAE. As both material combinations and material properties are unknown, a reverse approach was used to determine the behaviour of the roller. Figure 8 shows the design of the model. In the static experimental compression tests discussed in Section 3.3.4, time-dependent behaviour of the roller was found to be marginal. Therefore, a linear elastic material model was chosen and time-dependent effects were neglected. Due to large deformation, the model was analysed geometrically non-linear. The material of the outer coating was assumed to be isotropic; the material of the foam was assumed to be orthotropic due to the complex design of the tested compaction roller. The resulting parameters obtained via finite element analysis (FEA) are listed in Table 3.4. For test setups 1, 3, and 5, a 2D plain strain approach was used with 640 CPS4 elements and a rigid tool surface. For test setups 2 and 4, a 3D continuum model was built with 20580 C3D8 elements. Both models use a penalty contact formulation.

Table 3.4. Material parameters for the analogous FEM model obtained using the reverse approach (left) with sketch of model (right)

FEM Roller Dimensions	
Roller inner diameter	30.0 mm
Roller outer diameter	68.3 mm
Thickness of the release coating	2.5 mm
Material Properties of Release Coating	
E	$20.0 MPa$
ν	0.3
Material Properties of Roller Foam Material	
$E_1 = E_r$	$0.8\,\text{MPa}$
$E_2 = E_t$	$0.8\,\text{MPa}$
$E_3 = E_z$	$5.0\,\text{MPa}$
ν_{12}	0.3
ν_{13}	0
ν_{23}	0
G_{12}	$0.8\,\text{MPa}$
G_{13}	$1.2\,\text{MPa}$
G_{23}	$1.2\,\text{MPa}$
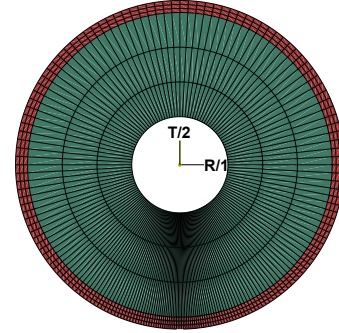
The linear elastic material model does not accurately cover hyperelastic material behaviour of most foams. Arising consequences are discussed in Section 3.3.5.2 of the chapter.

3.3.4. Resulting pressure distribution of experiments and simulation model

The static testing of the roller showed distinct results and confirm that the non-homogeneous design of the roller provides a non-hertzian pressure distribution under the roller as well as a specific deformation behaviour.

Figure 3.22 shows the typical roller deformations for all test setups described in Section 3.3.2.1. With the relative stiff and hard release coating compared to the foam material, one aspect of the normal pressure of the roller is the pre-stress of the bended coating, and the resulting transferred pressure. Therefore the roller cannot conform perfectly to the tool surface in some cases, and the pressure under the roller is influenced by the bending radius of the release coating.

Figure 3.22(A) shows the roller deformation on a flat tool. There is full contact under the roller, and a high bending deformation of the release coating at the edges of contact.
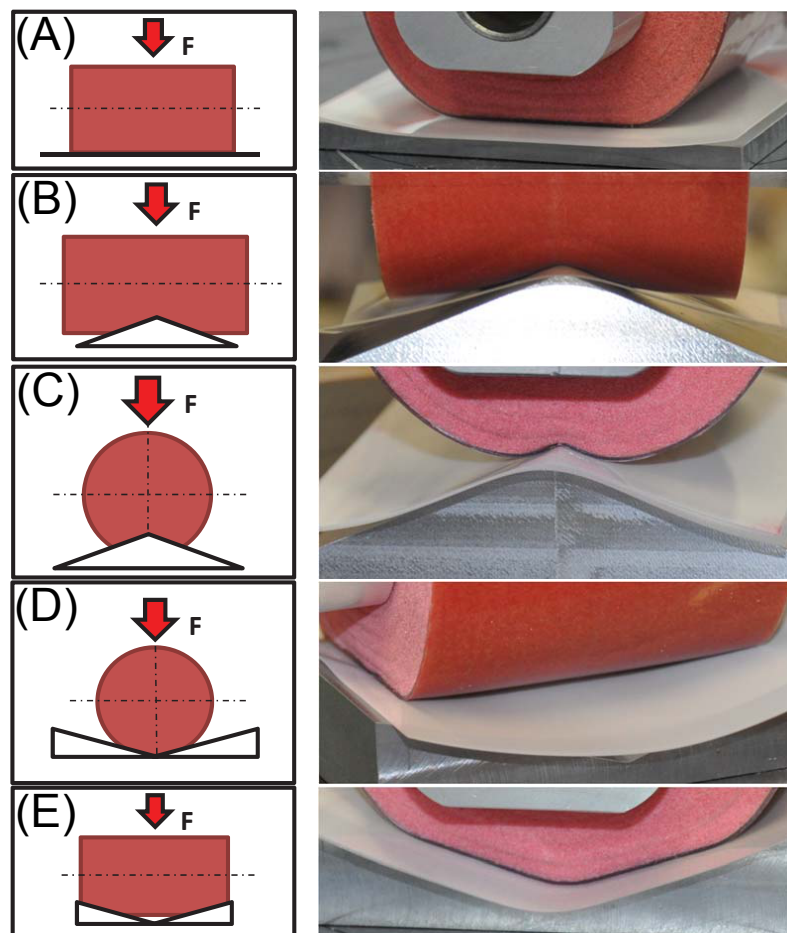
Figure 3.22. Typical roller deformation for all five test setups. (A) Flat tool, (B) convex tool lateral, (C) convex tool longitudinal, (D) concave tool lateral, (E) concave tool longitudinal, compare Lichtinger et al. [42]

At the convex tool (Figure 3.22 (B) & (C)) the roller does not fully conform to the surface. The high bending stiffness of the coating prevents full contact left and right of the apex of the tool. With the high deformation at the apex it is assumed that there is high normal pressure. Tests with high compaction force of 750 N had to be omitted so permanent damage to the compaction roller was prevented. The full deformability of the roller is seen with the concave tool (Figure 3.22 (D) & (E)). As point of first contact is on the flanges of the tool, the roller cannot slide into the resulting gap. Figure 3.23 depicts the displacement of the force controlled
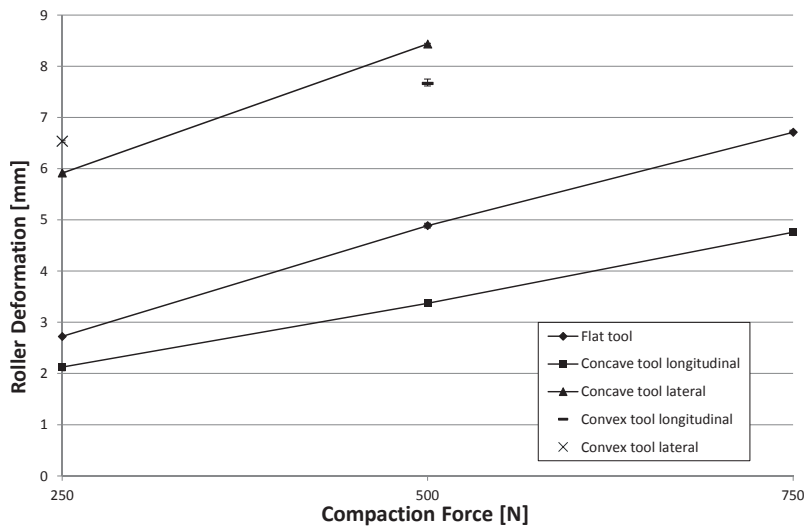
Figure 3.23. Displacement of the testing machine for all static roller tests [42].

universal testing machine. There is a linear trend visible, however, more data points are needed for a more detailed analysis of the trend of the displacement.

3.3.4.1. Pressure distribution on a flat tool

The pressure distribution of the roller on a flat tool is depicted in Figure 3.24. It is apparent that the experimental values experience high variance. On the evaluation path parallel and to the roller axis in the centre pressure resulting from 250 N compaction force vary from 0.08 MPa to 0.33 MPa, 400 % deviation. At 500 N force, pressures vary between 0.18 MPa and 0.36 MPa. At 750 N the pressure along the axis has a deviation of 195 %. The high variance origins from surface irregularities of the roller.

Simulation results along with experimental values of the pressure distribution orthogonal to the roller axis are pictured in Figure 3.25.
The pressure distribution is highly non-uniform. This arises because of the pre-stress of the release coating. With the non-uniform design of the roller, there is the effect that the pressure distribution on the evaluation path orthogonal to the roller axis
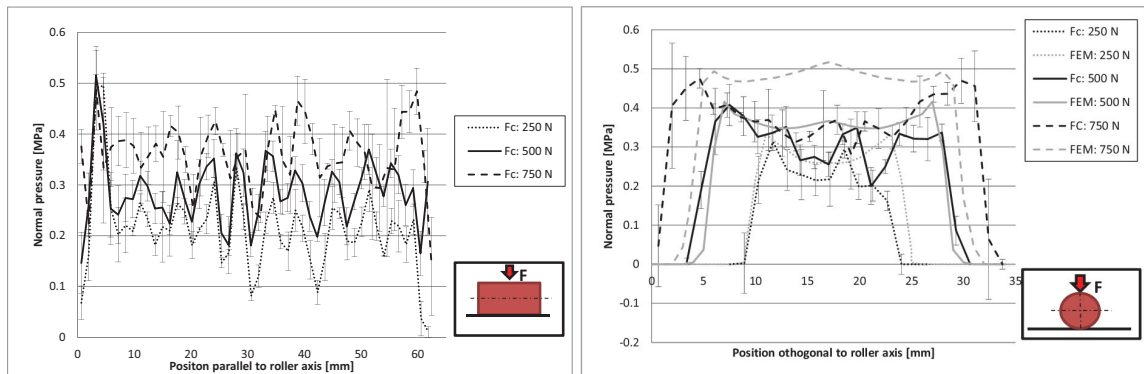
Figure 3.24. Pressure distribution of the compaction roller on the flat tool parallel to roller axis [42].

Figure 3.25. Pressure distribution of the compaction roller on the flat tool orthogonal to roller axis, compare Lichtinger et al. [42]

stays relatively constant compared to a hertzian pressure distribution, with peak pressures occurring at the out-most points of contact. The non-uniform pressure distribution compared to hertzian pressure as well as its implications are discussed in Section 3.3.5.3 of this chapter.

At a high compaction force, simulation results do not agree fully with the experimental values. Pressure magnitudes as well as pressure gradient is not represented sufficiently. It is presumed that the linear elastic material model for the foam material in the simulation model does not describe high compaction values within the foam sufficiently. The material model is discussed in detail in Section 3.3.5.2 of this chapter.
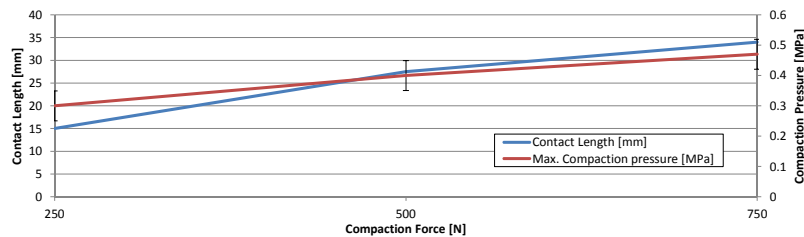
Figure 3.26. Contact length and maximum pressure over the compaction force

With higher compaction forces the contact length rises. The maximum pressure does not rise equivalent to contact length (compare Figure 3.26). With 250 N compaction force, contact length is 15 mm, while with 750 N contact length is 34 mm, an increase of 227 %. Maximum compaction pressure increases 157 % with triple the compaction force.

3.3.4.2. Pressure distribution on a convex tool

The convex tool represents the transition from the tapered section of the honeycomb tool to the top flat plane of the honeycomb ramp.

With the complex design of the roller, the pressure distribution on a convex tool has a specific gradient. The roller does not conform perfectly to the tool surface, but the stiff and hard release coating elevates the bending radius, therefore reducing pressure left and right of the apex of the tool. At a longer distance from the apex, the roller deforms sufficiently, therefore applying more pressure.
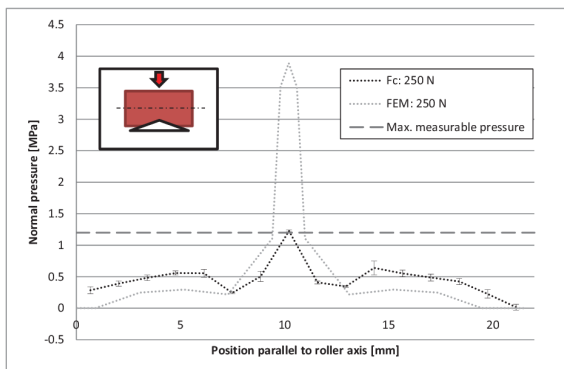
Figure 3.27. Normal pressure of the compaction roller on the convex tool in lateral direction parallel to roller axis, compare Lichtinger et al. [42]
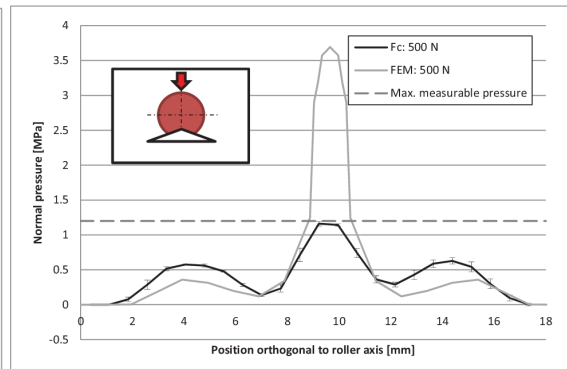
Figure 3.28. Normal pressure of the compaction roller in longitudinal direction orthogonal to roller axis on the convex tool. [42].

At the evaluation path of the roller axis orthogonal to the apex of the tool (Figure 3.27), highest pressure is at the centre at the apex. Maximum measurable pressure with the pressure sensitive film was $1.2\,\mathrm{MPa}$, therefore it is assumed that the pressure is underestimated experimentally. Left and right of the apex pressure is greatly reduced to $0.25\,\mathrm{MPa}$. Further along the evaluation path, the pressure rises again to $0.6\,\mathrm{MPa}$, $100\,\%$ above the minimum value.

Similar results occur at test setup 3, with the roller axis parallel to the apex of the tool. Peak pressure is at the apex of the tool, with experimental values assumed to be under-predicted. Left and right of the apex, the pressure reduces over-proportional because of the high bending stiffness of the release coating, with $70\,\%$ higher pressure further along the evaluation path.

Hexcel Nomex data sheet [71] states that minimum compressive strength of used *HRH - 10 - 1/8 - 3.0* has a minimum compressive strength of $1.62\,\mathrm{MPa}$ for direct pressure perpendicular to the surface. This pressure magnitude cannot be measured with current test setup. However, the simulation results state maximum pressures close to $4\,\mathrm{MPa}$, $247\,\%$ of the minimum compressive strength, therefore risking a crushing of the honeycomb core.

Further, honeycombs are very sensitive to side loading. When the compaction force vector deviates from the normal direction, e.g. at the ramped section of the honeycomb, the risk of core crush increases significantly.

3.3.4.3. Pressure distribution on a concave tool

The concave tool represents the transition from the flat plat to the ramped section of the honeycomb.

The outer edges of the roller contacts the tool first at the test setup "Lateral direction parallel to roller axis"(Figure 3.29). At $500\,\text{N}$ compaction force highest pressure occurs with $1.0\,\text{MPa}$. Pressure drops along the evaluation path non-linearly to a plateau at $0.5\,\text{MPa}$. At the centre of the evaluation path, the roller does not deform sufficiently, resulting in a gap between the contact at both sides of $28\,\text{mm}$. At $250\,\text{N}$ compaction force pressure peaks at the outer edge with $0.8\,\text{MPa}$, $20\,\%$ less than at twice the compaction force. The pressure drops to $0.4\,\text{MPa}$, with a $39\,\%$ greater gap of $39\,\text{mm}$.
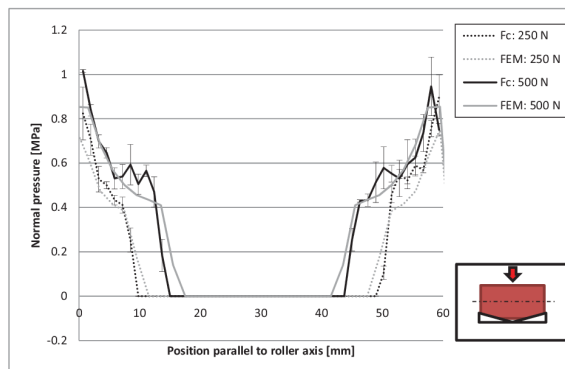
Figure 3.29. Normal pressure of the compaction roller in lateral direction parallel to roller axis on the concave tool, compare Lichtinger et al. [42]
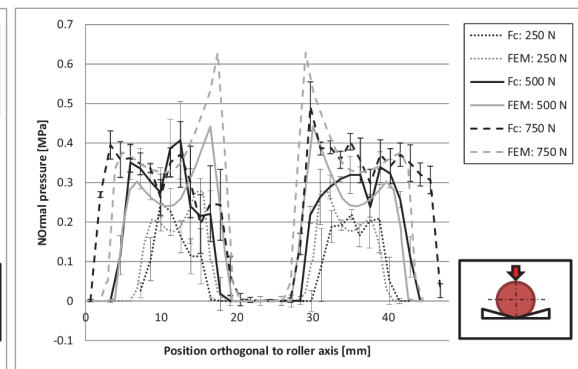
Figure 3.30. Normal pressure of the compaction roller in longitudinal direction orthogonal to roller axis on the concave tool. [42].

At test setup 5 "Longitudinal direction orthogonal to roller axis"(Figure 3.30) the roller does not conform enough to the tool surface to omit resulting gaps. Along the evaluation path a similar effect from Section 3.3.4.1 occurs, with highest pressure at the outer edges of the contact. With the inclined angle of the tool, and further movement down, shear is induced. These combined effects result in an exaggerated peak pressure at the inner contact edges, and reduced pressure at the outer edges of contact. At a compaction force of $250\,\text{N}$, the gap length is $13\,\text{mm}$, with a contact length of $11\,\text{mm}$ at both sides. At a force of $500\,\text{N}$, the gap length is $10\,\text{mm}$, $23\,\%$ less than at half the compaction force, and a contact length of $15\,\text{mm}$ on both sides

of the tool. At a compaction force of 750 N, the gap is 7.5 mm, 42 % less than at 250 N compaction force. The resulting contact length on both sides is 20 mm. Simulation results agree well with experimental values. Differences are assumed to arise from the high variability of the measured results. Further, there is an undefined stick-slip-condition at the experiments, while the simulation uses a permanent non-slip condition after contact.

3.3.5. Discussion

3.3.5.1. Design of the compaction device

The slit-tapes need to be compacted onto the tool surface. In most industrial applications, a compaction roller is used. The roller may have different designs, like the conformable full size roller used in this study, or a segmented roller [72]. Instead of a compaction roller, there is the possibility to use a compaction shoe [73] that slides along the tape surface, applying pressure. Sarrazin and Springer [17] state that a compaction device with radial shape may induce shear stresses as well as normal stresses opposite to the compaction pressure at the edges of contact (Figure 3.31).
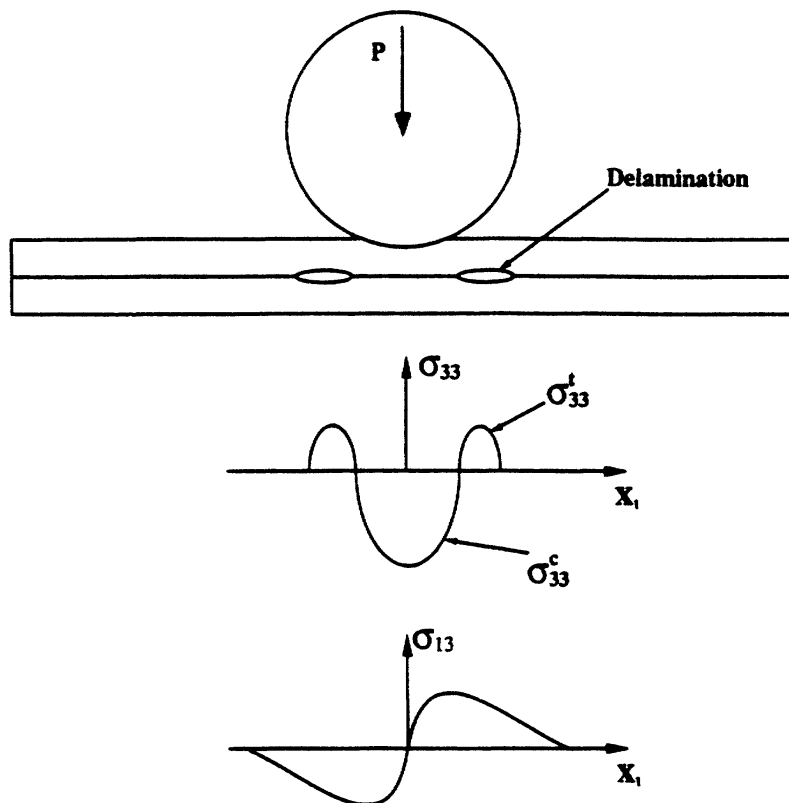
Figure 3.31. Induced stresses under a radial compaction roller from Sarazzin and Springer [17]

This may lead to the conclusion that a cylinder roller is not the perfect shape for a compaction device. Further, with the introduction of complex tool shapes with concave and convex surfaces and multiple curvatures, the concept of a deformable roller may not be sufficient. With a concave surface as in test setup 5 in Section 3.3.2, the contact on both sides of the roller happens before the roller deforms sufficiently to close the contact gap. With the assumption of non-slip contact due to the adhesive behaviour of the slit-tapes, it is no longer possible to close the bridging defect. Therefore, the compaction device should be able to adapt to the tool surface in a way that sufficient contact is guaranteed. This may lead to the development of a complete new compaction device.

Possible designs may be an inflatable compaction device. Also some functions could be implemented in the compaction device, e.g. local application of heat, instead of the IR lamp, by a heated compaction device, or a cooling effect to reduce peak temperatures, as was done by Henne et al. [18] for a thermoplastic AFP compaction roller.

Further work is needed to fully identify the potential of future compaction devices foraAFP, as well as to find the perfect design for such a device.

3.3.5.2. Linear elastic material assumption

The compaction roller was modelled with a linear elastic material assumption. However, the real roller consists of a coiled foam wrapped around an polyurethane foam core, with a release coating. As the exact material is under NDA, material properties are unknown, and needed to be determined by reverse engineering.

Usually, foam material with open pores, as is the case with the compaction roller, an hyperelasic material model is assumed. After initial linear behaviour, the material stress plateaus with increasing strain in compaction testing. When the material is compressed so the open pores are compressed, the material will go into block status, therefore potentially increasing in stress, as described in Zhang et al. [74] . In the model used in this study solely the first linear part of the deformation can be covered adequately. When the compaction strain increases further, resulting stresses are overpredicted.

Therefore, with high compaction forces, the normal contact pressures are overpredicted, as depcited in Figure 3.25 in Section 3.3.4.1. This affects the pressure distribution results for high compaction force values. However, for compaction forces usually input in an AFP process, the assumed material model agrees well with the experiments, and covers the material behaviour adequately.

3.3.5.3. Non-hertzian pressure distribution of the roller

The non-uniform pressure distribution of the compaction roller described in Section 3.3.4.1 is bound to have influence on the deposition process. Figure 3.32 shows the results of the compression of the roller on a flat surface at 500 N compaction force, compared to simulation results of the FEM model. Superimposed are the results of the analytical solution of Hertzian contact mechanics.
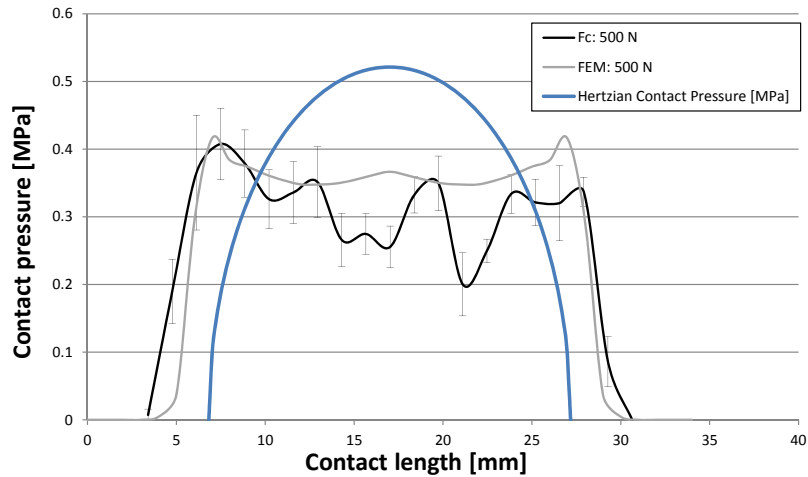
Figure 3.32. Comparison of the experimental and simulation values of static pressure of the compaction roller the analytical hertzian pressure

In the analytical solution, the pressure is a quadratic function of contact length (compare Equation 3.6b). Therefore highest magnitude of pressure is at the centre of contact, under the roller axis, with highly reduced contact pressures towards the edges of contact. The pressure distribution of the real compaction roller has peak pressures near the edge of the contact. This may come as an advantage on concave tool surfaces, e.g. a tapered honeycomb ramp, as the contact pressure peaks at the transition between flat tool and tapered section, therefore reducing possible bridging effects.

Further, with a more uniform pressure distribution, any shear or delamination effects, as described in Sarrazin and Springer [17], will be considerably reduced.

3.3.5.4. Validity of the model

The model of the compaction roller can be considered valid for low and medium pressures. For high compaction forces, the pressure distribution, as well as the deformation behaviour, care needs to be takes with the resulting predicted pressures. Furthermore, the model was simplified from the coiled foam material, with adhesive layers between each foam layer and a release coating on the outer surface to a orthotropic material behaviour in the foam section and an isotropic linear behaviour in the release coating. Roller dimensions are similar. However, the simplified model features a release coating with higher thickness than reality. When considering complex deformation modes of the roller, this fact may influence the deformation behaviour and corrupt the validity of the model. The stiffness of the release coating influences the pressure gradients on the area of contact.

Further work is needed to study the hyperelastic material behaviour of the foam, as well as its influence on the pressure distribution.

3.3.5.5. Alternative to the surface pressure measuring systems

As an alternative to the *Prescale* pressure measuring system, an electromechanical procedure was evaluated for testing. The *Tekscan* system is a commercially available normal pressure evaluation method. The electromechanical procedure assigns measured electrical resistance to a calibrated pressure value. The electrical resistance changes with applied normal pressure. Figure 3.33 depicts the test setup with concave tool longitudinal and the assignment from measured electrical resistance to applied calibrated pressure.
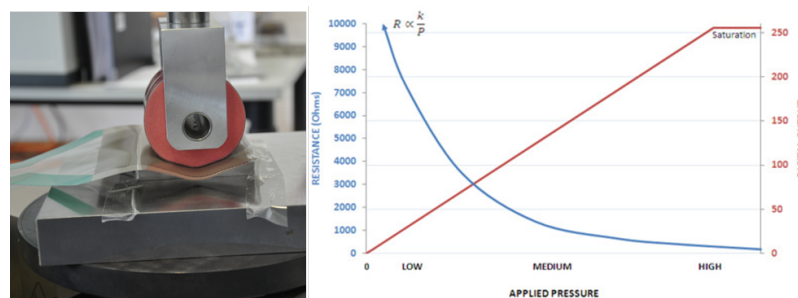
Figure 3.33. Test setup with the *Tekscan* system (l) and its pressure evaluation procedure (r)

The size of one measurement cell is 6.45 mm² and it an has an edge length of 2.54 mm. Figure 3.34 shows an exemplary result of the *Tekscan* system.

The resolution is smaller compared to the *Prescale* procedure. The major advantage of the *Tekscan* system is it ability to measure the pressure over time with a resolution of up to 100 Hz. The calibration of the system has to be conducted a priori with a
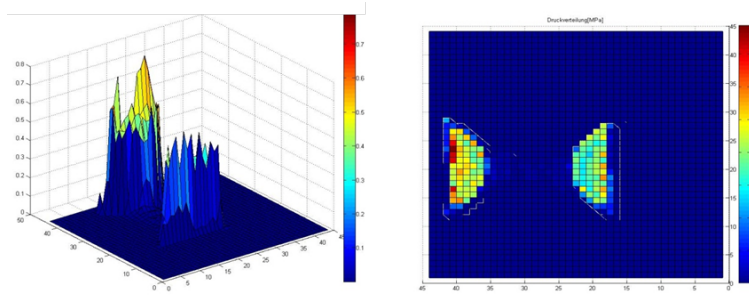
Figure 3.34. Tekscan results during the test of concave tool perpendicular

correction factor.

Both pressure measuring methods have their advantages and disadvantages, listed in Table 3.5:

Table 3.5. Comparison between two methods to measure surface pressure

	Advantages	Disadvantages
Prescale	High resolution after smoothing	High recurring cost for a high number of tests
	Repeatable process	Only static pressure measurable
	Low initial cost for academic purposes	Limited range of pressure for individual sheet type
		High cost for industrial software
		Difficult Handling
TekScan	Repeatable process	High initial cost
	Low recurring cost	Calibration necessary
	Time-dependent measurements possible	Limited resolution
	Dynamic tests possible	
	Easy handling	

For this study the *Prescale* pressure measurement system was used to evaluate the results. The resolution for the small contact area was too low for adequate results.

3.4. Experimental determination of through-thickness compaction behaviour of prepreg tapes under AFP conditions

In the thermoset AFP process, after the layup is complete, the laminate is consolidated. Consolidation involves the application of certain temperatures and compaction pressure to the laminate for predetermined lengths of time.

Usually, for aerospace grade prepreg material, consolidation happens in an autoclave at elevated temperatures and up to seven bar compaction pressure. Further, in most industrial cases, some further vacuum assisted debulking may happen during layup, after the completion of every n^{th} ply, to increase layup quality of the already placed laminate.

In the thermoset AFP process, the layup is also consolidated during layup, as the compaction roller presses the incoming slit-tapes onto the tool surface, or the already placed substrate. Further, the resin viscosity is reduced with elevated temperatures due to the influence of the IR lamp. Helenon et al. [46] modelled the thermoset AFP deposition process with focus on through thickness compaction and in-plane elongation, depending on process velocities.

There is a thickness difference between non-consolidated uncured slit-tape material and consolidated, fully cured theoretical laminate thickness. It is assumed that the thickness changes arises from consolidation of voids, and resin flow through-thickness of the partially impregnated slit-tapes.

Although the compaction pressure acts locally for a short amount of time, the high compaction pressure and elevated temperatures lead to a debulking effect, which was experimentally studied and is subject of following section of the chapter. The material used for the experiments is an aviation grade toughened slit-tape material.

3.4.1. Test setup of through-thickness compression experiments

3.4.1.1. Preparation of the test samples

The test samples are flat composite laminates with the dimensions of $20\,\text{mm} \times 20\,\text{mm} \times h_0$. The initial thickness of the test samples, h_0, arises from the hight of ten individual tapes stacked up. It ranges between $1.6\,\text{mm}$ and $1.8\,\text{mm}$.

Two different types of test samples were manufactured:

- Unidirectional (UD): Similar fibre orientation for all ten plies

- Multidirectional (MD): The fibre orientation was
  $[0°, 90°, 45°, 135°, 0°, 90°, 135°, 45°, 90°, 0°]$

Two plates, UD and MD, with dimension $220\,\text{mm} \times 220\,\text{mm}$ were loosely placed by hand. A $0.05\,\text{mm}$ non-adhesive PTFE film beneath and on top of the plies facilitated handling and prevented any sticking. The samples were than cut into the desired size.

3.4.1.2. **Test setup**

For the short-term compression tests, a modular compact *Rheometer MCR 302 Anton Paar* was used. It is capable of controlled compressive force up to 50 N. From the static compaction roller testing in Section 3.3, a maximum pressure of 0.5 MPa for the compaction of the roller on a flat surface is obtained. Therefore, a standard rheometer punch was turned to a diameter of 10.0 mm. With Equation 3.9:

$$F = p \cdot A, \tag{3.9}$$

with p the required normal pressure and A the punch area, the compaction force as machine input can be calculated. Table 3.6 lists the calculated compaction forces.

Table 3.6. Resulting compaction forces for desired compaction pressures

Compaction pressure [MPa]	Resulting Compaction Force [N]
0.2	15.7
0.3	23.6
0.4	31.4
0.5	39.3

The test samples were inserted into the test chamber. Then, a test cycle with a combination of load application, intermittent by a release time were applied. At the release times, the controlled load was set to zero, and the upward movement of the punch was measured at all times, so that the relaxation, and therefore a thickness growth, was also captured.

Following process parameters for both UD and MD test samples were tested, with variations in:

- Process temperature,

- Pressure magnitude,

- Release time and

- Compaction time.

Table 3.7 summarizes the values for the process variables stated above:

For all tests only one process variable was changed with fixed values for all other stated process variables. This results in 16 different tests for both UD and MD.

The initial thickness of the stack was determined by measuring the compaction force. When the measured force exceeds 0.1 N, the gap size is defined (compare Figure 3.36).
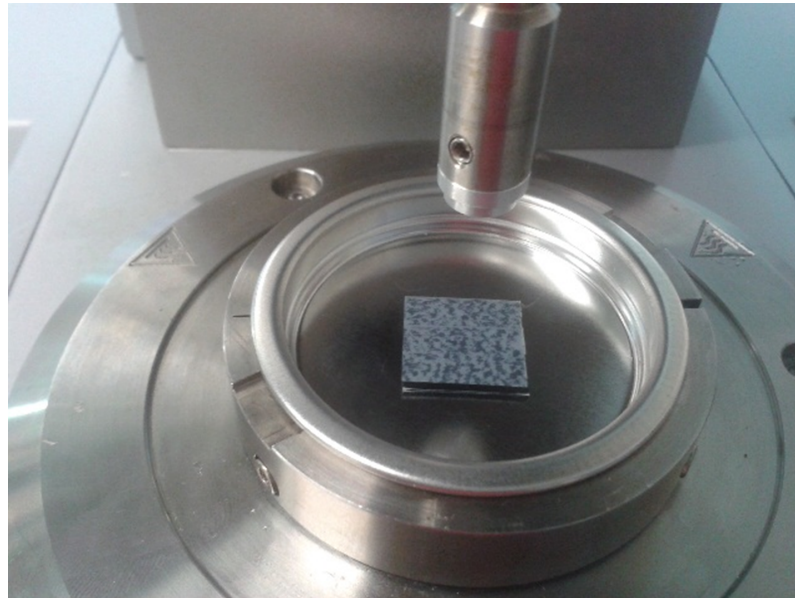
Figure 3.35. Experimental Setup of the compression tests. For elevated temperature a
thermal controlled hood was used (not shown).

Table 3.7. Varied process variables of the compression testing experiments

Pressure Magnitude	[MPa]	0.2 / 0.3 / 0.4 / 0.5
Temperature	[$°C$]	25 / 35 / 45 / 55 / 65
Compaction Time	[s]	1.0 / 2.0 / 4.0 / 6.0
Release Time	[s]	5 / 30 / 60 / 120 / 300

All tests were repeated five times to gain insight into repeatability.

3.4.2. Experimental results

The initial machine read out is depicted in Figure 3.36. With set machine parameters, the compaction - release cycle is repeated eight times, with varied process parameters. After each cycle, the point of maximum compaction and the point of maximum release is evaluated.
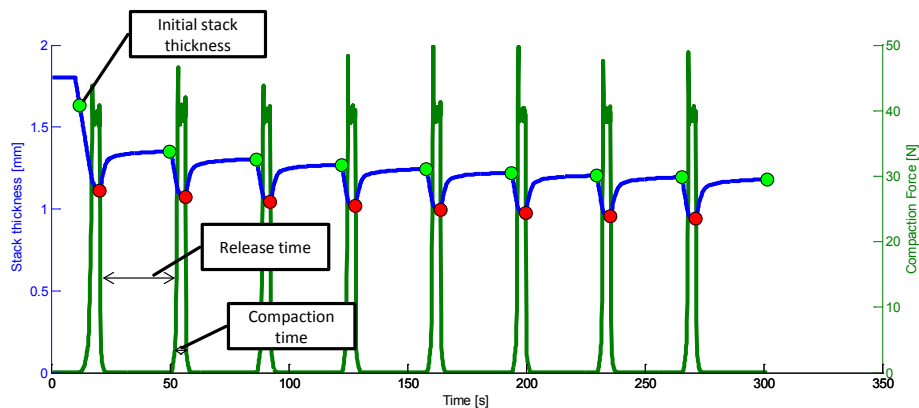
Figure 3.36. Experimental result for 55 °C Compression, with superimposed result evaluation procedure

It is observable that the stack thickness expresses behaviour of a visco-elastic material. After initial compaction,the stiffness of the material increases non-linear. After release of the compaction pressure, the material increases in thickness, therefore expressing the elastic behaviour.

All performed tests were evaluated on shown data points, starting with the initial stack thickness when the compaction force exceeds 0.1 N. At each compaction-release cycle the point of minimum stack thickness ("Low") is evaluated, as well as the point of maximum stack thickness ("High") after the complete release time without pressure. The graphs are plotted over the number of compaction-release cycles for multi-directional layup (Figures 3.37 to 3.40) and UD layup (Figures 3.41 to 3.44).

Unless stated otherwise, test parameters were:

- Process temperature: 55 °C

- Pressure magnitude: 0.5 MPa

- Compaction time: 3 s

- Release time: 30 s

Process variables are stated in the legend of the Figures.

Figure 3.37 shows the variation in process temperature for MD layup after each

cycle the stack thickness is reduced, and there is no convergence in thickness change after the eight' cycle is completed. Therefore further thickness change with higher number of compaction cycles is to be expected. With higher temperature the thickness change increases. Similar results show the variation of pressure (Figure 3.38). The higher the pressure the more the thickness change. As seen in Figure 3.39 and Figure 3.40, compaction pressure variation as well as release time variation has little influence on the stack thickness change.
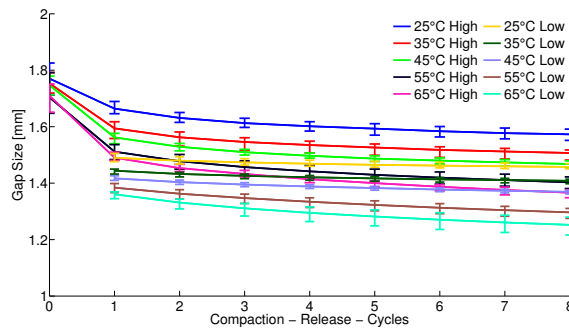
Figure 3.37. Compaction results of MD setup with temperature variation
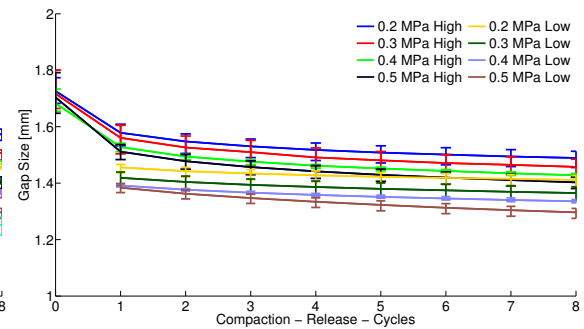
Figure 3.38. Compaction results of MD setup with pressure variation
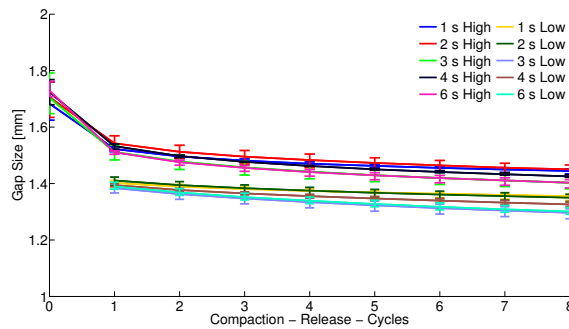
Figure 3.39. Compaction results of MD setup with compaction time Variation
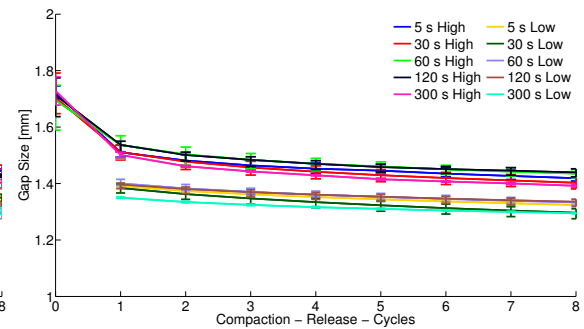
Figure 3.40. Compaction results of MD setup with release time variation

Figure 3.41 to Figure 3.44 show results compared to MD layup. Thickness change is higher than the MD stacks. At no test setup convergence in stack thickness is reached, therefore the thickness would decrease further with higher amount of compression cycles.

Figure 3.45 shows the influence of process temperature in thickness change percentage wise with UD and MD results juxtaposed. The thickness change from initial stack thickness to after release time at room temperature is 11.1 % for MD and 10.5 % for UD, −5.9 % difference. At a process temperature of 65 °C the thickness change is 20.1 % for MD and 40.8 % for UD, a difference of 103.1 %.

The influence of the applied pressure is depicted in Figure 3.46. The thickness change in UD layup is generally higher than MD, however it is apparent that the thickness
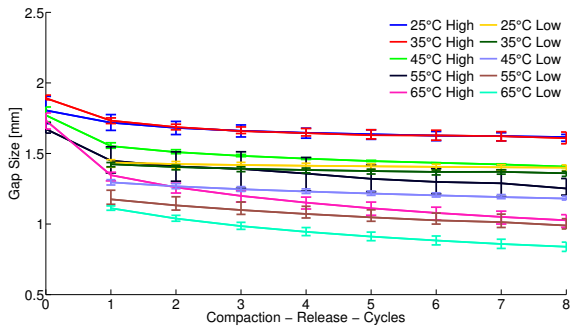
Figure 3.41. Compaction results of UD setup with temperature variation
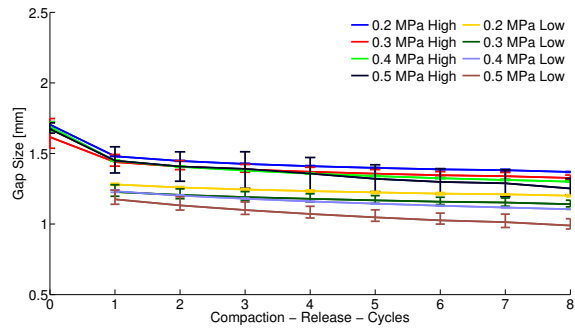
Figure 3.42. Compaction results of UD setup with pressure variation
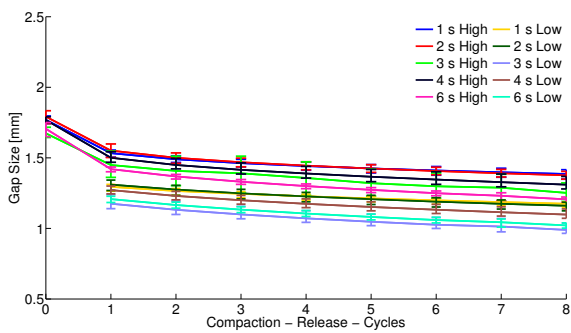
Figure 3.43. Compaction results of UD setup with compaction time Variation
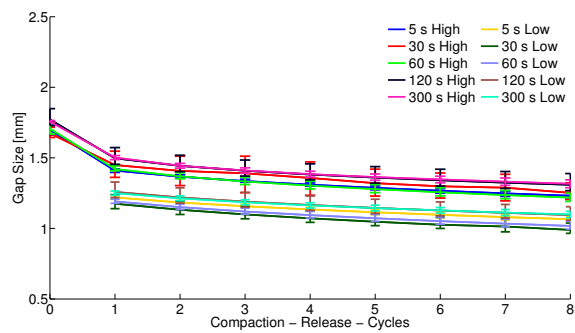
Figure 3.44. Compaction results of UD setup with release time variation

change is depending little on the applied pressure magnitude, with a difference of 21.8 % for UD and 22.3 % for MD between applied pressures 0.2 MPa and 0.5 MPa.

The influence of compaction time on stack thickness (Figure 3.47) shows that the thickness change increases with increased compaction time, indication viscous behaviour. Release time has little influence on the final stack thickness (Figure 3.48) with no apparent decrease with increased release time. Still there is a prominent difference between UD and MD between 29.1 % and 86.6 %. These findings correspond with measurements from Hall et al. [75]. They find that the difference between UD and cross-ply stacks arises from lateral spreading and a restriction thereof in a cross-ply stacked laminate. Further work is needed to fully understand the correlation between compaction to AFP process parameters, that also include in-plane influences.
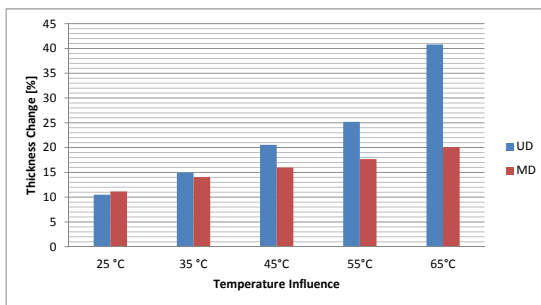
Figure 3.45. Influence of temperature in thickness change [%] after eight compaction cycles
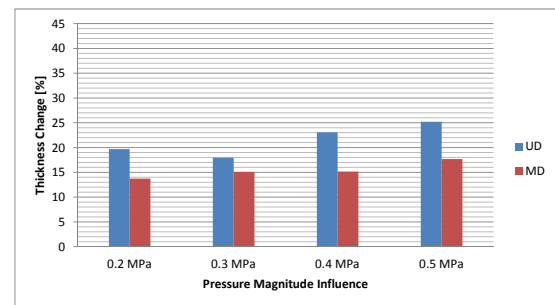
Figure 3.46. Influence of pressure variation on compaction [%] after eight compaction cycles
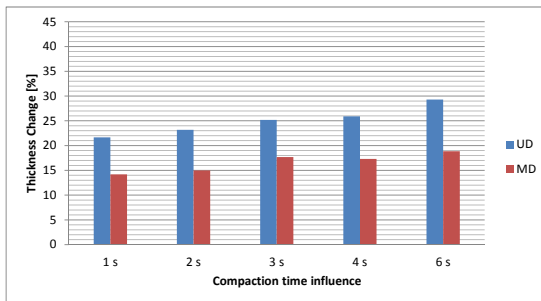
Figure 3.47. Influence of compaction time in thickness change [%] after eight compaction cycles
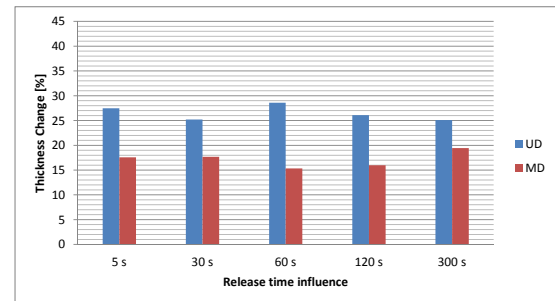
Figure 3.48. Influence of release time in thickness change [%] after eight compaction cycles

3.4.3. Discussion

The deformation behaviour of the slit-tapes influences most process parameters. Heat conduction as well as contact resistance are influenced by the compaction of the slit-tapes.

Further, with varying slit-tape thickness, void content as well as fibre volume fraction or an expansion in-plane is imposed, and therefore also the later laminate properties.

3.4.3.1. Influence on thermal material properties

The thickness change due to applied pressure under elevated temperatures alters thermal properties of the material stack. As test results show, stack thickness may change more than $40\,\%$ of its original value.

First, the compaction increases interlaminar intimate contact, therefore reducing thermal contact resistance considerably.

Further, with the decreased thickness of the plies, conduction through thickness changes considerable.

3.4.3.2. Void content and fibre volume fraction

With the applied pressure the void content of the material will reduce. Especially when voids are enclosed between plies, applied contact pressure enhances intimate contact, therefore reducing voids. As Cai and Gutowski [55] state, deformation of a lubricated fibre bundle is dependent on the waviness of the fibres as well as the viscous behaviour of the resin. This could indicate that with applied pressure the waviness of the fibres is reduced, which presumably enhances layup quality.

Further studies are needed to determine AFP process parameters like compaction pressure or elevated temperatures on the micro scale quality of fibre orientation and waviness.

3.4.3.3. Viscoelastic behaviour of compression response

The results from the compression response clearly indicate a viscoelastic material behaviour. After release of the compression pressure, the stack thickness increases. This indicates that a pure plastic deformation approach, as was done in [65] and in Helenon et al. [46], is not suitable for modelling the compression - release response cycle of the material.

Further studies have to be performed to gain insight into the deformation behaviour to distinguish between viscous and elastic parts of the compression response, as well as their influence on further AFP parameters.

4. Thermal measurements and thermal models for AFP

Heat input into the tool surface, as well as on the already placed substrate, is one of the most important aspects in AFP. Layup temperature plays an important role in- later mechanical performance of the laminate, e.g. inter laminar shear strength or void content[3]. If the temperature exceeds the material limit, artificial ageing or partial curing could occur [28]. When the process temperature drops below a threshold value, there is the risk of insufficient tack [27] - the ability of the slit-tapes to stick to the surface - and subsequent process failure. It is therefore imperative to influence the process temperatures to a suitable window of operations during layup. The AFP machines used in the experiments conduct the heat input in the form of two-bulbed IR lamps by *Heraeus Noblelight*. Their measurements show a close relationship to a lambert radiator [76], as depicted in Figure 4.1.
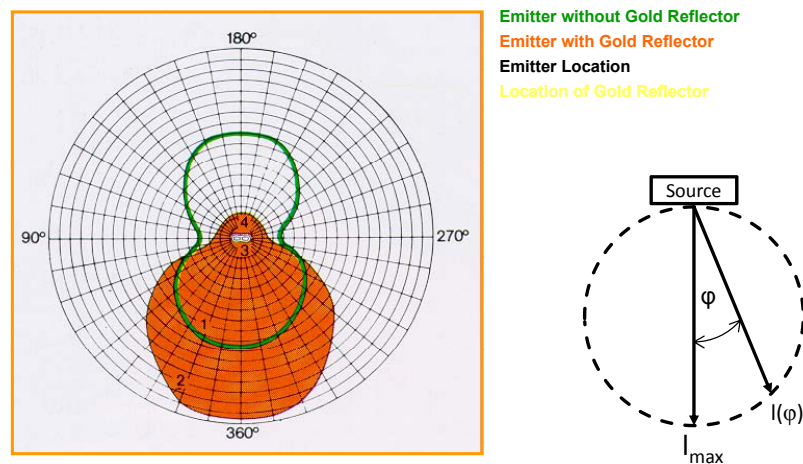
Figure 4.1. Lambert cosine law compared with the radiation distribution of Heraeus Noblelight IR emitter [76]

During the placement process the tool surface or the already placed substrate is heated up in front of the nip point. When the tapes touch the surface, they take on its temperature. This reduces the viscosity of the resin and activates their tackiness. In combination with contact pressure distribution and lay up velocity, temperature is the main driver for lay up quality.

Although there has been progress in recent years, heat input during the automated manufacturing process is realistically still in development, and is not a mature technology - despite its extensive application in industry [28].

Understanding of the process temperatures is especially important for challenging tool geometries. For multi-material tools like honeycomb - metallic tooling, heat

input needs to be controlled, as head conductances and heat capacities vary widely. For curved surfaces with complex kinematic movements and rotations of the robot with subsequent varying heat input, knowledge of process temperatures is imperative to avoid too little or too much heat input.

To understand the process and to reduce the gap between depth of understanding and application, process models for single-material tools and linear motion of the robot head were developed and validated. Then the model is expanded to cover more complex tools along with the sophisticated 3D rotational and translational movements of the placement robot. To experimentally determine the effects of heat input during the placement process, and to validate the simulation models, two different fibre placement machines with two different slit-tape materials were used. For flat placement experiments, the material *Toray T800S/3900-2* was used, for the placement on the tapered honeycomb an aerospace grade prepreg material by *Hexcel* under NDA, which is referred in the following as *Hexcel*.

4.1. Literature review for thermal analysis of automated composite manufacturing processes

In commercially available software packages, regulation of the power output, and therefore the process temperature, is usually dependent on the kinematics of the placement head and is independent of tool or slit-tape material properties. To reduce this gap in design, many thermal models have been developed, mostly reducing the problem dimensionally and therefore neglecting in-plane effects of the heat transfer. Tierney et al. [77] model heat transfer and void dynamics in the thermoplastic tow placement process to quantify the effects of process parameters. They use a 1D through-thickness model including convective heat transfer. On-line processing of hoop wound composite structures is proposed by Chern et al. [78–81]. They use radiation in the form of a volumetric or surface heat flux in a 2D Eulerian domain, and focus on the influence of independent and dependent scattering. Sarrazin and Springer [17] use a 2D finite element approach to calculate both thermoset and thermoplastic fibre placement in a combined thermal-stress model. The heat input, in the form of convective, conductive or microwave heating, is applied as a constant heat flux on a moving surface area. The thermoplastic fibre placement process is modelled thermally by Sonmez et al. [82], coupled with a crystallisation kinetic model with constant heat flux boundary conditions in a steady state process. Pitchumani et al. [83] use a previously created 2D heat transfer model for the thermoplastic tow placement process for optimisation and the development of a process window for in-situ consolidation. Kim et al. [84] suggest a possible in-situ cure of hoop-wound cylinders using radiative heating. They developed a 2D model with a moving

constant heat source covering a certain arc length of the cylinder. One of the first papers to take thermal contact resistance into account was Barasinski et al. [85]. They focus on the thermal modelling of the thermoplastic tape placement process which takes into account the imperfect bonding existing between the different layers of the substrate. Narnhofer et al. [86] present the current state of the art in simulating the tape-laying process for thermoplastic matrix composites, including imperfect bonding and polymer healing.

Due to the progression in computational power, recently some work concerning thermal simulation for fibre placement/tape laying was conducted in the three-dimensional (3D) domain. Hassan et al. [87] use a Lagrangian formulation to solve a 3D problem in the fibre placement process. They validate their model by continuously winding tapes onto a cylindrical mandrel. The used heat source is a hot gas nozzle modelled as constant convective heat transfer over an arc-length of the cylinder. Chinesta et al. [88] propose a new methodology to model complex coupled thermo-mechanical models for the AFP process for an efficient simulation. They combine a laser heat source with a novel 3D approach. Hörmann et al. [89] use a 2D FD model with heat input as diffuse lambert radiator. They neglect heat flow perpendicular to the placement path, and assume perfect contact.

Although there are many more process models available, few include the effect of heat flow in all directions. Most existing models that include radiative heating apply the heat input constantly over a certain area. The view factor - the orientation of two areas relative to each other in space - of a quasi Lambert-radiator IR lamp, and therefore its radiation distribution, is neglected.

Only recently has the importance of thermal contact conductance been introduced [28, 85, 88]. Contact conductance is highly influenced by the surface roughness of the contact partners [90]. For toughened AFP materials, surface roughness plays a major role concerning void content and tack [3], as well as for through-thickness thermal conductance [91]. Levy at al. [92] state the significance of the effect of thermal contact resistance for thermoplastic automated placement processes.

Little work was done to understand the effect of the radiation distribution of an industrial scale IR lamp in combination with the thermoset AFP process. Due to the influence of the radiation distribution of the IR lamp, there will be heat input over a large area of the tool throughout the whole process, along with in-plane and through-thickness heat flow in tool and substrate. The placement on multi-material toolings including complex geometry finds little attention in literature. The highly time-dependent behaviour of heat transport along with the complex movement of the robot plays a mayor role during the placement process, and needs to be further analysed.

4.2. Thermal material models

For transient thermal simulation models for homogeneous material, three material properties need to be available to predict thermal conduction within the material:

- Density

- Conductivity

- Specific heat of the material

Further, for adequate boundary conditions, following material parameters need to be known:

- For surface radiation heat input: emissivity

- Thermal contact conductance for non-perfect contact

Due to the little temperature difference, free convection on the surface is neglected.

Depending on the material used, thermal properties may be temperature dependent. For orthotropic materials, e.g. the slit-tapes or *Nomex* honeycombs, conductivities have direction dependent behaviour. In the case of *Nomex* honeycomb, the properties have a high spatial variance due to the inhomogeneous design. Within this study the properties were homogenized with direction dependency.

4.2.1. Thermal material model for uncured pre-impregnated tapes

For different test setups the two prepreg materials *Toray's T800S/3900-2* and *Hexcel* were used.
Both are toughened aerospace grade fibre placement materials with comparable areal weight and fibre volume fraction.

4.2.1.1. Density

To determine the slit-tape density, strips of similar length were cut from the spool. Every strip was measured in length, as well as its thickness determined at different points of the strip. With the known width of the slit-tape, the volume was calculated.
Then the mass of each strip was measured using a *Mettler* precision scale. With mass and volume, density was calculated.
For *Hexcel* a mean thickness of $0.217\,\mathrm{mm} \pm 3.6 \times 10^{-3} mm$ was measured, and therefore a mean density of $1.33 \times 10^{-3} g/mm^3 \pm 1.1 \times 10^{-5} g/mm^3$ calculated.

Toray's T800S/3900-2 was measured with a mean thickness of $0.221\,\mathrm{mm}\pm0.007\,\mathrm{mm}$, and a mean density of $1.278 \times 10^{-3} g/mm^3 \pm 7.496 \times 10^{-5} g/mm^3$ was calculated. The density is assumed to be independent of temperature.

4.2.1.2. Thermal conductance

According to Johnston [93] temperature dependency of thermal conductivity for prepreg material can be calculated, using

$$\lambda_{11} = \lambda_r \cdot (1 - \varphi_f) + \lambda_f^{11} \cdot \varphi_f \tag{4.1}$$

for fibre direction and

$$\lambda_{22} = \lambda_{33} = \lambda_r \cdot \left\{ \left(1 - 2\sqrt{\varphi_f/\pi} \right) + \frac{1}{B} \left[\pi - \frac{4}{\sqrt{1 - B^2\varphi_f/\pi}} tan^{-1} \frac{\sqrt{1 - B^2\varphi_f/\pi}}{1 + B\sqrt{\varphi_f/\pi}} \right] \right\} \tag{4.2}$$

with

$$B = 2 \cdot \left(\frac{\lambda_r}{\lambda_f^{22}} - 1 \right). \tag{4.3}$$

for transverse fibre direction. These approaches do not include internal voidage within the tapes, however, with the small void percentage within aerospace grade tapes this effect was assumed to be negligible.

With the conductivity of the fibres in fibre direction $\lambda_f^{11} = 35.10\,\mathrm{W/mK}$ [94] and Johnstons linear dependency on temperature [93] of the resin system *HexPly 8552*

$$\lambda_r = 0.148\,\mathrm{W/mK} + 3.43 \times 10^{-4}\,\mathrm{W/mK^\circ C} \cdot T\,(^\circ C) \tag{4.4}$$

and the assumption of zero cure, following linear temperature dependencies for prepreg tapes can be approximated:

$$\lambda_{11_{PP}} = 1.44 \times 10^{-4}\,\mathrm{W/mK} \cdot T\,(^\circ C) + 20.42\,\mathrm{W/mK} \tag{4.5a}$$

and

$$\lambda_{22_{PP}} = \lambda_{33_{PP}} = 1.01 \times 10^{-3} W/mK \cdot T\,(^\circ C) + 0.44\,\mathrm{W/mK}. \tag{4.5b}$$

Although applied material parameters have been partly taken from a different prepreg system, the assumption of similar material parameters can be made, as both ma-

terials are toughened aerospace grade prepregs with comparable areal weights and
highly similar viscosity profiles. Therefore above parameters were used for both
prepreg materials used during testing.

Furthermore parameter studies have shown that deviations of the thermal conductiv-
ity in and transverse to fibre direction have little effect on the process temperatures
due to the small thickness of the slit-tapes.

4.2.1.3. Specific heat

Specific heat of Toray T800S/3900-2   The specific heat values were taken from
Dykeman [95]. With the assumption of zero cure and therefore a fully rubbery state
the temperature dependent specific heat takes the linear form of

$$c_{pT} = s_{r0} \cdot T \left({}^{\circ}C \right) + c_{r0} \tag{4.6}$$

with $s_{r0} = 2.84644 \cdot 10^{-3}$ and $c_{r0} = 1.1966$.

Specific heat of the *Hexcel* material   The specific heat was measured using Dif-
ferential Scanning Calorimetry (DSC). After initial calibration of the machine, the
specific heat capacity was measured using Equation 4.7:

$$c_{pT} = \frac{60 \cdot H \cdot K}{H_R \cdot M}, \tag{4.7}$$

with c_{pT} the specific heat capacity in $[J/g/{}^{\circ}C]$, K the calibration constant, H the
measured heat flow in $[mW]$, H_R the heating rate of $10\,{}^{\circ}C/min$ and M the sample
mass in $[mg]$.

The resulting linear approximation for the temperature dependency below cure tem-
perature is stated in Equation 4.8:

$$c_{pT} = s_{r0} \cdot T \left({}^{\circ}C \right) + c_{r0} \tag{4.8}$$

with $s_{r0} = 3.59 \cdot 10^{-3}$ and $c_{r0} = 0.91$.

4.2.2. Thermal material model for Nomex honeycomb

The material used for following studies was *Hexcel Nomex HRH-10-1/8-3.0*.
This product consists of *Dupont's Nomex* aramid-fibre paper dipped in a heat-
resistant phenolic resin to achieve the final density. It features high strength and

toughness in a small cell size, low density non-metallic core [71].
For all thermal models the 0.05 mm thick adhesive film is neglected as material parameter, however the full area is used to calculate heat input into the material.

4.2.2.1. Density

The density of *Hexcel Nomex HRH-10-1/8-3.0* is stated in the product data sheet [71] with $48.055 \, \text{kg/m}^3$ with a maximum deviation of $\pm 10 \, \%$.

4.2.2.2. Thermal conductance

According to Hexcel's Honeycomb property sheet [71], through-thickness thermal conduction of *Nomex* honeycombs is temperature dependent. The little dependency on honeycomb thickness is neglected.
The in-plane conductances are reversely calculated by concluding to the thermal conductance of the pure core material λ_{cm} using the Swann and Pittman model [96], stated in Equation 4.9:

$$\lambda_{33_{Honeycomb}} = \lambda_{cm} \frac{\Delta A}{A} + \lambda_{c,gas} \left(1 - \frac{\Delta A}{A} \right) + \lambda_{c,rad}. \tag{4.9}$$

With $\Delta A = 6 \cdot t_c \cdot S_{hex}$, t_c the measured cell wall thickness 0.05 mm, and $S_{hex} = \frac{\sqrt{3}}{3} * S_c$ with S_c as the cell size 3.175 mm. A as the nominal area with $(S_{hex})^2 \frac{3}{2} \sqrt{3}$. k_{cm} is the conductivity of the core material and $k_{c,gas}$ the conductivity of air. Conductivity through radiation, $k_{c,rad}$, is neglected.
Fatemi and Lemmen [97] take this model and conclude from the through-thickness conductivity to in-plane properties with following Equations 4.10a and 4.10b:

$$\lambda_{11_{Honeycomb}} = \frac{1.5 \cdot k_{cm} \cdot t_c}{S_c} \tag{4.10a}$$

and

$$\lambda_{22_{Honeycomb}} = \frac{1}{3} \frac{k_{cm} \cdot t_c \cdot S_c}{S_{hex}^2}. \tag{4.10b}$$

Figure 4.2 depicts the resulting homogenized orthotropic thermal conductivity dependent on temperature in a range between $-18 \, °\text{C}$ and $204 \, °\text{C}$.
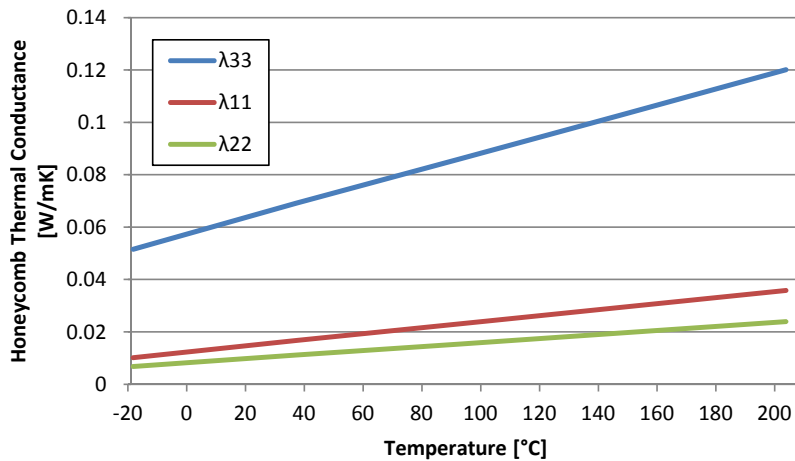
Figure 4.2. Orthotropic thermal conduction of *Hexcel Nomex honeycomb HRH-10-1/8-3.0*

4.2.2.3. Specific heat

According to Bitzer [98] the specific heat of Nomex / phenolic (HRH 10) honey-combs is in a range between 1170 J/gK and 1338 J/gK. Within this study the value of 1338 J/gK has been found to represent the material behaviour adequately. Temperature dependence is neglected.

4.2.3. Emissivities of the irradiated surfaces

Emissivity values for slit-tape prepregs and oxidized aluminium were taken out of literature [99].

For the placement on the tapered honeycomb covered with an adhesive film, emissivity values were gained using infrared thermography in combination with the measurement with TCs. Both temperature values were compared, and the emissivity was reversely calculated by aligning the temperature of the thermography image with the measured temperature of TC 11 at the same time step (see Figure 4.3). The large drop in temperature at the thermography values comes from the overlap of the cooled placement head.

Emissivity values of the shadowing areas of the head are assumed to be close to 1.0, to omit undefined reflection within the simulation model. Table 4.1 lists the emissivity values used in later simulation.

4.2.4. Thermal contact conductances between two parts

Due to asperities or irregularities of the prepreg surface perfect contact cannot be assumed [28, 30, 85, 92]. Therefore heat transfer needs to include the thermal contact resistance between all relevant contact partners.
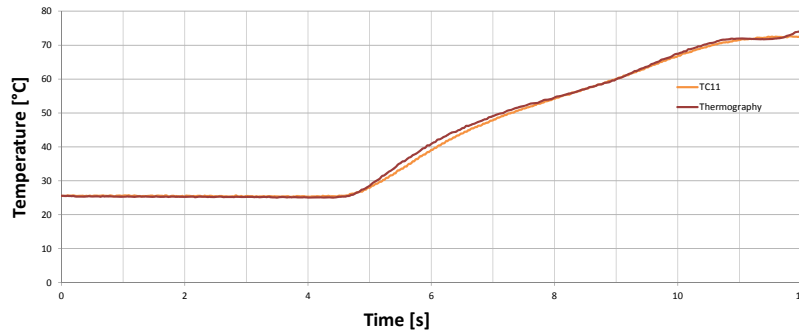
Figure 4.3. Thermography Emissivity calculation with help of the thermal video analysis, the light barrier as well as the TC recording

Surface Material	Emissivity Value [-]
Aluminium Tool	0.3
Slit-Tape Material	0.9
Adhesive Film on top of honeycomb	0.65
Placement Head	1.0

Table 4.1. Emissivity values for irradiated surfaces

According to Madhusudana [90], heat transfer through a joint depends on surface roughness, hardness, and conductivity of both joined materials. Moreover thermal contact is highly dependent on the contact pressure.

Due to the computational efficiency of the 1D model, it was used in this work to calibrate thermal contact conductances between the tool and the first ply, h_{TP}, as well as between each ply, h_{PP}. A parametric study was conducted and the values have been found by aligning local maxima and minima of the temperatures to the experimental values.

The thermal contact conductance, which is reversely proportional to the thermal contact resistance, is implemented as heat flow between two surfaces. Within this studies, contact conductance is assumed to be independent of temperature or pressure. A detailed discussion can be found in Section 4.6.5 of this Chapter.

Table 4.2 lists all used contact conductances within this study.

Contact Partners			Contact Conductance Value $[mW/mm^2 K]$
Tape	-	Tape	5.5
Tape	-	Aluminium	0.55
Tape	-	Adhesive Film	0.55
Honeycomb	-	Aluminium Tool	0.55

Table 4.2. Thermal Contact Conductances between surfaces

Thermal contact conductances were reversely gained through parametric studies of the simulation models described in Section 4.3.4. It is assumed the difference in conductances between two tapes arises from the viscoelastic contact under elevated temperatures. Further studies are necessary to determine the complete contact dependency on the AFP process variables.

4.3. Thermal modelling

To predict the thermal history of the AFP process and gain insight in the relevant heat transfer mechanisms, following different dimensional depth is used:

- One-dimensional (1D) finite difference model for fast and efficient parametric studies

- Two-dimensional (2D) finite difference model for heat up and cool down phase prediction as well as heat flow in the placement plane

- Three-dimensional (3D) finite element model to capture the relevant effect of 3D heat flow in the tool and substrate.

In the following, aspects of heat transfer are closely evaluated along with AFP specific boundary conditions, as well as their numerical solution methods.

4.3.1. Aspects of heat transfer

To model the different thermal experiments, transient heat transfer equations are used. Taking the general law of energy conservation

$$\frac{\partial}{\partial t} \int_V \rho\, c_p \,\mathrm{d}V = - \int_{\partial V} \dot{q}_i \,\mathrm{d}A_i \tag{4.11}$$

and the definition of Fourier's Law

$$\dot{\mathbf{q}}\left(\mathbf{x}\right) = -\lambda \nabla \mathbf{T}\left(\mathbf{x}\right), \tag{4.12}$$

with ρ the density, c_p the specific heat capacity, V the equivalent volume, A the equivalent surface, λ the direction-dependent thermal conductance and T temperature, adequate transient thermal process models are derived.

4.3.2. AFP specific thermal boundary conditions

For analytical or numerical solutions to transient heat transfer models, boundary conditions have to be applied. In the case of the described experiments, the following boundary conditions were implemented:

- The initial temperature T_0 of the tool, substrate and slit-tapes at $t = 0\,\text{s}$

- Thermal insulation at the bottom of tool was:

$$\dot{q}_{x_3} = \lambda_3 3 \left.\frac{\mathrm{d}T}{\mathrm{d}x_3}\right|_{x_3=0} = 0 \tag{4.13}$$

  with λ_3 as the transverse conductivity.

- Infrared radiation input on the topmost area was:

$$\dot{q}_{x_3} = \varepsilon\varphi_{12}\eta_H\frac{\mathrm{d}P}{\mathrm{d}A} \tag{4.14}$$

  with φ_{12} the view factor (detailed in Section 4.3.3), ε as the emissivity of the substrate, η_H the coefficient of efficiency of the heat source to convert electrical power into radiation and P the electrical power consumption of the IR lamp.

- Thermal contact conductance (detailed in Section 4.2.4):

$$\dot{q}_{x_3} = h_C \cdot \mathrm{d}A \cdot \mathrm{d}T \tag{4.15}$$

  with $h_C = h_{TP}$ for contact between tool and ply 1 and $h_C = h_{PP}$ for contact between all further plies.

The effects of heat flow due to free convection were neglected due to the small temperature differences.

4.3.3. Radiation heat transfer

Radiation is the energy emitted by matter in the form of electromagnetic waves (or photons) as a result of the changes in the electronic configurations of the atoms or molecules [100]. Kirchhoff's law of thermal radiation describes the emission, transmission and absorption behaviour of a solid body. Under the assumption of no transmission, heat absorption due to radiation equals its emissivity. Lambert's cosine law states the radiant intensity from an ideal diffuse radiator to be directly proportional to the cosines of the angles between the two surface normals, as is the case of the two IR lamps used in the thermal experiments. Therefore, radiation heat transfer between surfaces depends on the orientation of the surfaces relative to each other

as well as their radiation properties [100]. To account for the relative position of two surfaces A_1 and A_2, the purely geometric quantity called the view factor, based on Lambert's cosine law, has to be calculated. It is independent of material properties or process temperatures. The general equation of the view factor for surfaces $A_1 \rightarrow A_2$ takes the form

$$\varphi_{12_{general}} = \frac{1}{\pi A_1} \int_{A_2} \int_{A_1} \frac{\cos(\beta_1)\cos(\beta_2)}{r^2} \, \mathrm{d}A_1 \mathrm{d}A_2, \qquad (4.16\mathrm{a})$$

where β_1 and β_2 are the angles between the respective area normal vector and the vector between both surfaces $\overrightarrow{A_1 A_2}$, and $r = ||\overrightarrow{A_1 A_2}||$.

As the dimensions of the IR lamp used in the experiments were much smaller than the tool, the assumption of a point-source as heat source without spatial expansion can be made. Alongside this, the 2D lebesgue measure of the area A_1 becomes zero and Equation 4.16a simplifies to

$$\varphi_{12_{pointsource}} = \frac{1}{\pi} \int_{A_2} \frac{\cos(\beta_1)\cos(\beta_2)}{r^2} \, \mathrm{d}A_2. \qquad (4.16\mathrm{b})$$

In the case of a zero-dimensional heat input for a 1D model, Equation 4.16b further reduces to

$$\varphi_{12_{0D}} = \frac{1}{\pi} \frac{\cos(\beta_1)\cos(\beta_2)}{r^2} \cdot A_2. \qquad (4.16\mathrm{c})$$

4.3.4. Thermal models

The 1D and 2D FD models were implemented to cover the placement on a flat tool surface with a linear path. The 3D FEM models are parametrized to cover any type of tooling, from flat to more complex shape with multiple materials.

4.3.4.1. 1D Finite Differences thermal model

A detailed description of the 1D thermal model can be found in Lichtinger et al. [28] and is omitted here.

4.3.4.2. 2D Finite Differences thermal model

The heat transfer equations in Section 4.3.1 are reduced to a two-dimensional state, and solved using the commercial software MatLab.

The model (Figure 4.4) consists of:

- the tool with defined thickness and length,

- n initial plies, with $n \in \mathbb{N}_0$,

- a portion of current ply, where the model is expanded with every time step to account for additional parts of the current tape and

- the IR lamp as point source.
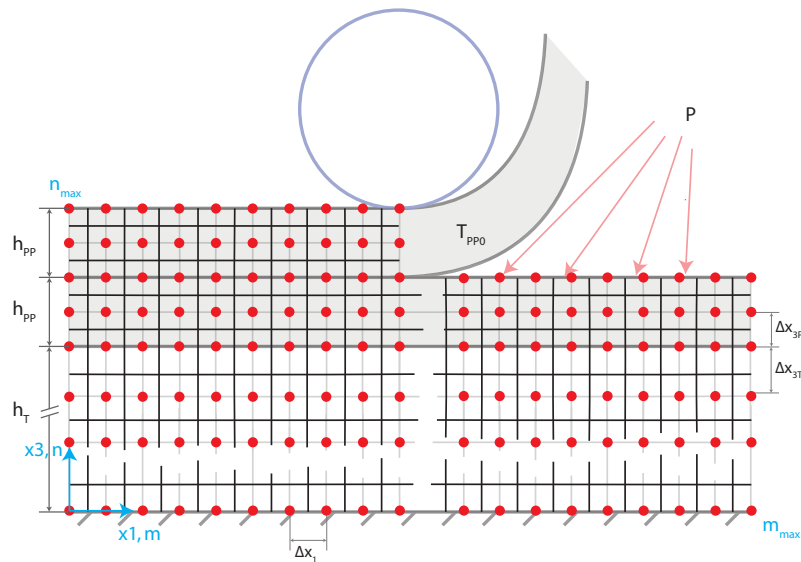
Figure 4.4. 2D FD simulation model discretised with a rectangular mesh

All boundary conditions as well as material properties taken from Section 4.3.2 and Section 4.2. The movement of the head is input as constant velocity, with updated view factor every time step. The model is solved implicitly transient for predefined amount of plies.

4.3.4.3. 3D Finite Element thermal model

To solve the transient 3D heat transfer equations described in Section 4.3.1 and include in-plane as well as out-of-plane heat flow, an implicit FEM model was created using the commercial FEM software Abaqus CAE (see Figure 4.5).

The model is fully parametric, allowing the study of a multitude of varying parameters.
The models consist of:

- The tool as a 3D continuum, without restrictions in dimensions and complexity, with the possibility of manual CAD import.

- Already deposited plies or portions of the plies as shell elements. These account for conduction in all directions, as well as the influence of thermal contact conductance between all plies.
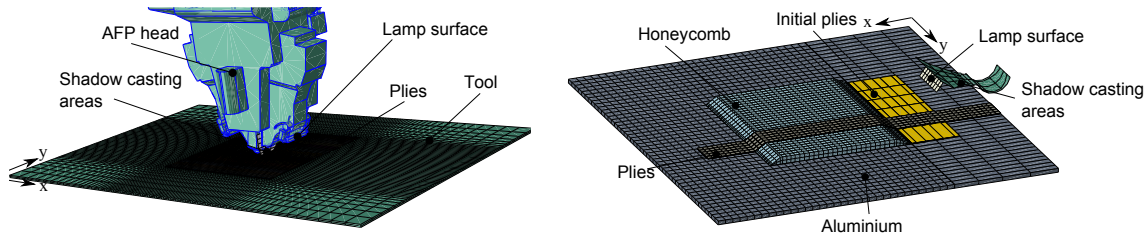
Figure 4.5. Abaqus 3D FEM Models for flat placement experiments on the *Coriolis Composites* $8 \times 1/8''$ slit-tapes by *LCC* (right) and for the placement on the honeycomb surface *Coriolis Composites* $8 \times 1/4''$ slit-tapes (left) by *Fraunhofer ICT FIL*. Images not to scale.

- For every path to be placed one individual model part modeled with shell elements. During the solving of all time steps, the simulation model is expanded with individual portions of the ply pathwise after completion of each path of the robot.

- The IR lamp as surface with two defined sides as heat input and heat output modelled as shell elements.

- The shadow casting surfaces of the placement head modelled with shell elements. The idealized surfaces have a fixed temperature, and absorb all radiation directed at the surface.

The model is transiently discretised by defined time steps, separated by the sequence of paths to be placed as input parameters.

Solving of the model happens in $2 \times$(amount of paths)+2 time steps in the sequence of:

1. Head moves from home position to starting point of path 1

2. Head moves along path 1 until the end of the path

3. Head moves from end point of path 1 to start point of path 2. The model is expanded with the material placed at path 1, and a thermal contact with the underlying substrate is created

    . . .

(n-2). Head moves along path n until the end of the path

(n-1). Head moves from end of path n into home position. The material for the last path is created along with the thermal contact

n. Cool-off time for an equalisation of temperatures, there is no radiation from the IR lamp

The simulated IR lamp emits at set power. Depending on the AFP machine used for validation, the IR lamp is switched on or off in transition between two paths. The view factor is recalculated after every time increment using Equation 4.16a.

Boundary conditions are equal to Section 4.3.2, with the exception of the lamp surface of $19.0\,\text{mm} \times 40.0\,\text{mm}$ for the $1/8''$ AFP machine, and $23.0\,\text{mm} \times 70.0\,\text{mm}$ for the $1/4''$ AFP machine, taking into account the influence of the area and the aspect ratio of the lamp.

The emissivity values of Section 4.2.3 were used as input for the aluminium surface, the honeycomb surface as well as the substrate plies.

All models described above predict the temperature history during the AFP process on different levels. These predictions could be used for a thermal control of the process including an on-line feedback loop. These possibilities are discussed in detail in Section 4.6.8.

4.4. Thermal measurements

To validate the thermal models, several placement experiments have been performed to capture bulk and surface temperature. First, both bulk and surface temperatures were evaluated during the placement of a flat structure on a aluminium tool. Further, the experiments were expanded for the placement on a honeycomb structure. For both the placement of a flat plate as well as the placement on a tapered honeycomb structure, the temperatures have been evaluated and compared with simulation results.

Figure 4.6 depicts the *Coriolis Composites* AFP machine used for the tests on the tapered honeycomb. The machine is capable of placing simultaneously eight slit-tapes with a width of $6.35\,\text{mm}$ each. The machine uses a gold-plated two bulbed IR lamp with a nominal power of $525\,\text{W}$ and a nominal heated area of $70\,\text{mm} \times 23\,\text{mm}$. The *Hexcel* material was used in the tests.

For the flat placement on an aluminium tool a different *Coriolis Composites* AFP machine was used (Figure 4.7). That machine can place eight slit-tapes with a width of $3.18\,\text{mm}$ each. The machine uses a IR lamp by *Heraeus Noblelight* with a quartz-coated reflector. Its nominal power output is $440\,\text{W}$, and the nominal heated area is $40\,\text{mm} \times 23\,\text{mm}$. The material used in the tests was slit *Toray T800S/3900-2* prepreg.

Figure 4.6. *Coriolis Composites* AFP machine for 8 1/4" slit-tapes, located at *Fraunhofer Institute for functional Lightweight Design* in Augsburg, Germany
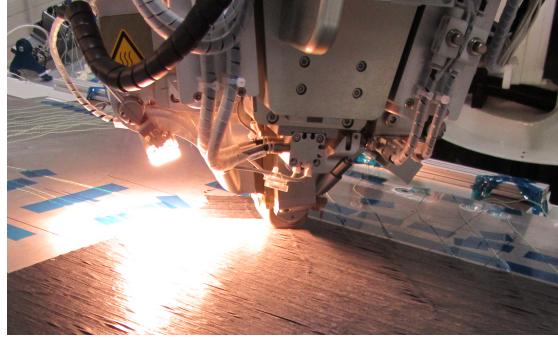
Figure 4.7. *Coriolis Composites* AFP machine for 8 1/8" slit-tapes, located at *Institute for Carbon Composites* in Munich, Germany

4.4.1. Measuring bulk temperatures with thermocouples

Bulk temperatures were measured with type K TCs in combination with a *National Instruments CompactRIO* and a *LabVIEW* recording routine. With the flat placement experiments, the TCs were fixed between ply 1 and 2 [28]. At the placement on a tapered honeycomb, five TCs were fixed on top of six layers of tape in front of the honeycomb, and 15 TCs were fixed on the adhesive film covering the honeycomb. The different test setups are depicted in Figure 4.8.
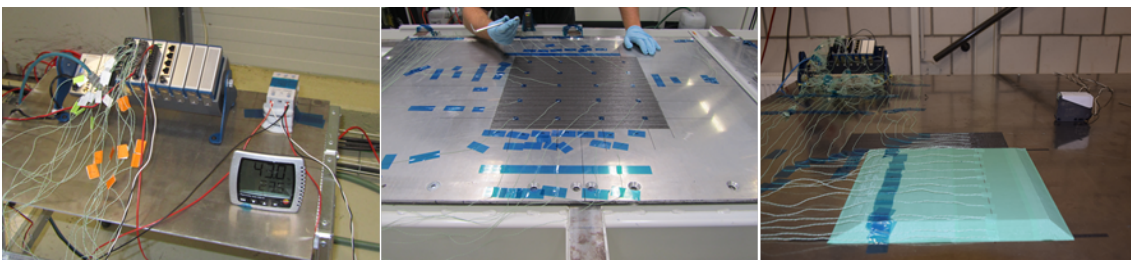
Figure 4.8. Setup for bulk temperature measurement

The signal of a light barrier, when the placement head passed through it, was used as a time stamp. With that, the repeats of the measurements could be shifted towards each other, so the mean temperatures as well as the error limits could be calculated. The upper error limits were computed using $T_{+err} = T_{max} - T_{mean}$ and the lower error limits $T_{-err} = T_{mean} - T_{min}$ for all measurement points.

TCs were calibrated at the beginning of the measurements to room temperature.

4.4.2. Measuring surface temperatures with thermography

A *FLIR A305/325 sc* thermal camera by *FLIR Systems* was used to measure the surface temperature during the experiments. For the placement experiments on the flat tool, the thermal camera was mounted to the placement head for the local surface temperature distribution. The camera recorded with 30 Hz, and temperatures were evaluated perpendicular to the movement direction with the length of 63 mm, 35mm in front of the nip-point. Lower and upper error limits are calculated similar to bulk temperature [28].

For the placement experiments on the tapered honeycomb the camera was next to the test setup for a complete overview during the process. Figure 4.9 shows the resulting images of both test setups.
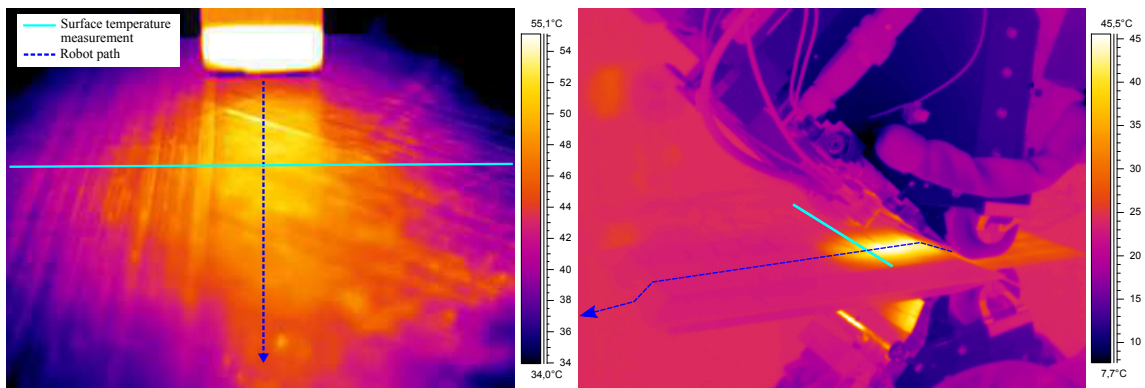
Figure 4.9. Resulting thermography images of flat placement tests (left) and placement on tapered honeycomb (right)

As the heat source is an infrared emitter with similar wavelengths to the thermal camera, special care has to be taken to evaluate the experiential results. This includes avoidance of direct IR radiation onto the camera lens, as well as special attention of the evaluated surfaces, that have a spectral reflection of the IR lamp.

4.4.3. Tracking the movement of the placement robot

The movement of the placement head is completely defined by the robot programming with the six Degrees of Freedom (DOF) of the Tool Centre Point (TCP) in relation to the tool coordinate system.

The placement program gained from kinematic AFP offline simulation consists of two files:

- One file containing all points of all paths along with the desired cardan orientation

- One file with specific commands for the placement robot, including point-to-point movement, maximum velocity between two points as well as AFP specific actions, e.g. cutting and restarting of tapes or control for the IR lamp

The two files are transferred manually to the human machine interface (HMI) at the AFP cell. There, the internal programming of the robot, in this case *KUKA KR240* with *KR C4* controller, interprets the NC programming. The programmed speeds from offline simulation are maximum values. The unknown internal robot programming overrides these maximum speeds with values that are safe for application. When considering the maximum speed of a placement on a tapered Honeycomb, it would take four seconds, while the actual experiment took more than 15 seconds.

The resulting velocity depends heavily on the allowed acceleration of the individual axes of the robot. Especially on sections of paths where stub-axles four, five and six of the robot experience large movements, the real speed of the robot will reduce drastically. Further, when paths with a large amount of points are laid up, the velocity also depends on the calculation capacity of the robot's processor.

Therefore, to use the robot program code for simulation input, the actual robot velocity needs to be mapped to the specific path points.

To do this, video analysis was used. The in-plane translational and rotational movement of the robot was tracked with a bright LED spot. The spot was mounted to the roller centre of the placement head, as depicted in Figure 4.10, and the complete placement procedure was captured with video.

The recorded video was enhanced in contrast and colour using the open source video editing software *VirtualDub*. In the next step the movement of the robot was analysed automatically using the open source software *Viana.NET 4*.

Figure 4.10. Movement Tracking Procedure a) video with LED spot b) enhancement of contrast c) automated analysis

With the known distance between touch-down and lift-off point of the placement head from the robot source code, the distances out of the video analysis could be converted from the pixel size to actual distances, in accordance with the appropriate time stamp, and therefore mapped to the robot program code.

As this tracking procedure is purely 2D, complex out of plane movement of the robot cannot be captured. The tracking along with the known paths of the robot was sufficient for an accurate analysis for the experiments described within this work.

4.4.4. Test setups for flat and honeycomb - placement

4.4.4.1. Placement of a flat structure - test setup

The test data is taken out of the test series from Lichtinger et al. [28]. The test setup is the placement of a flat plate with dimensions $450\,\text{mm} \times 450\,\text{mm}$ on a $1410\,\text{mm} \times 910\,\text{mm} \times 8.0\,\text{mm}$ thick aluminium plate.
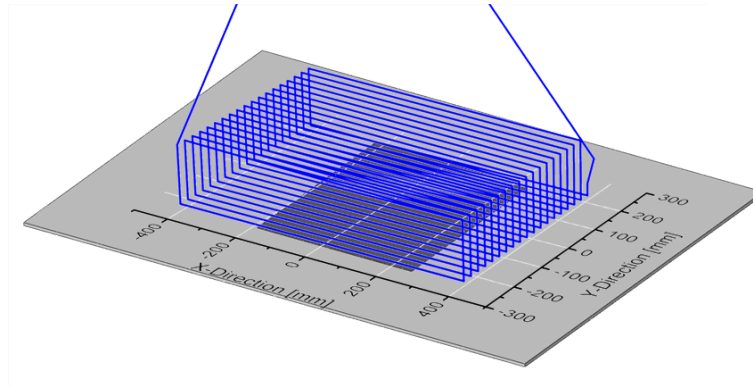
Figure 4.11. Robot Path for the placement on ply 3

Table 4.3 lists the relevant machine parameters as well as the processing conditions.

Angle of IR lamp towards nip point	20.0°
Horizontal offset of the centre of the lamp from roller centre	132.0 mm
Vertical offset of the lamp centre from substrate surface	60.3 mm
Deposition velocity 0°	59.1 mm/s
IR lamp - electrical power uptake	318 W
Compaction Force	250 N
Roller diameter	34.0 mm
Roller width	30.0 mm

Table 4.3. Test setup and geometric dimensions of the AFP head

As the experimental setup is fully described in Lichtinger et al. [28], a detailed description of the setup is not provided at this point. Table 4.3 lists all relevant boundary conditions.

4.4.4.2. Placement on a tapered honeycomb - test setup

The thermal tests were conducted on a *Coriolis Composites* AFP machine with the capability to deposit $8 \times 1/4''$ narrow tapes simultaneously, stationed at the *Fraunhofer ICT FIL*.
The tool was a $1400\,\text{mm} \times 1400\,\text{mm} \times 8.0\,\text{mm}$ flat aluminium plate. To prepare the

manual deposition of the tapered honeycomb, an initial placement of one layer of tape was conducted. This prevented the honeycomb to slide due to transverse forces during the latter testing.

In front of the honeycomb six layers of tape with a width of 2×50.8 mm were placed to simulate an initial substrate similar to industrial applications. The test setup is depicted in Figure 4.12, with superimposed rotational and translational movement of the robot.

At the touch-down point of the placement head a light barrier was installed to align the repeats of the tests in time, so mean values could be calculated.
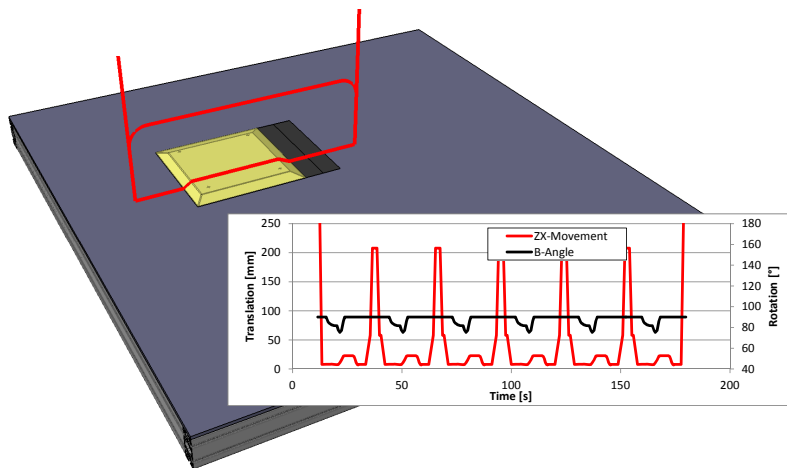
Figure 4.12. CAD Drawing of the test setup of the placement on the tapered honeycomb including the path of the AFP head with superimposed translational (red) and rotational (black) movement of the robot

The actual test was conducted by placing one path of tapes across the tool, already placed tapes and honeycomb six times. This resulted in a layer of six tapes along the path.

To capture the bulk temperatures five TCs were fixed to the already placed tapes in front of the honeycomb. The fixture procedure was to use the same material as the underlying substrate, therefore for the 5 TCs on the already places tapes, a small strip of tape with the average length of 10 mm was used, and for the 15 TCs on the honeycomb small patches of adhesive film with the average size of 10 mm $\times$ 10 mm (see Figure 4.13). The locations of the TCs are superimposed, starting from the edge of the already placed plies.

The stripes and patches already exhibited adhesive behaviour due to their nature, therefore making them a good fixture method. The locally increased thickness at the measuring spots with the accompanying measuring deviations had to be accepted.
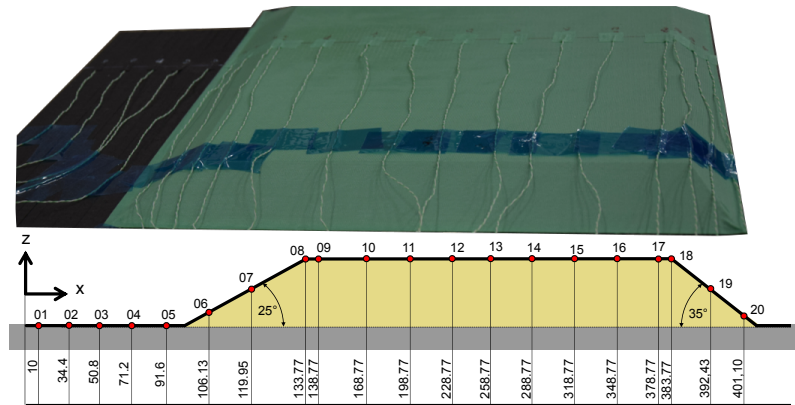
Figure 4.13. Fixtures of the TCs on the adhesive film of the honeycomb structure including their location

4.5. Comparison of results of experiments and simulation

4.5.1. Results of the flat placement

The transient 3D model, as well as the 1D model, were used alongside the experimental work to gain insight into the thermal history of both bulk and surface temperatures of a complete ply area during the deposition process [28].

For comparison of 1D, 2D and 3D simulation results with experiments, solely the centre path is evaluated in higher detail in the 0° placement of ply 3. Accordingly one TC at the centre path (TC 12) is used to evaluate simulation results. Starting temperatures of the simulations of the pure centre path were elevated to 24 °C to account for the preceding heat input of the ten previous passes of the placement head.

4.5.1.1. Bulk temperatures

Point-wise measurements clearly show the passing of the AFP head and the influence of the IR lamp at a distance. Figure 4.14 depicts TC 15 during the placement of ply 3. It is apparent that the radiation distribution of the IR lamp cannot be neglected. Although local heat is dissipated quickly into the tool, the global rise in temperature within the part is significant. Comparing the simulation results of the 1D model in ply 3 with the experimental results, before passing of the AFP head it is evident that the temperature was underestimated, whilst at the locations of the lamp near the measurement point, and after the passing of the head, temperature was overestimated. This was expected with the 1D assumption of no in-plane conduction.

Whereas the 3D FEM simulation results, including in-plane heat dissipation, are in good agreement with the experiments and well within error limits.
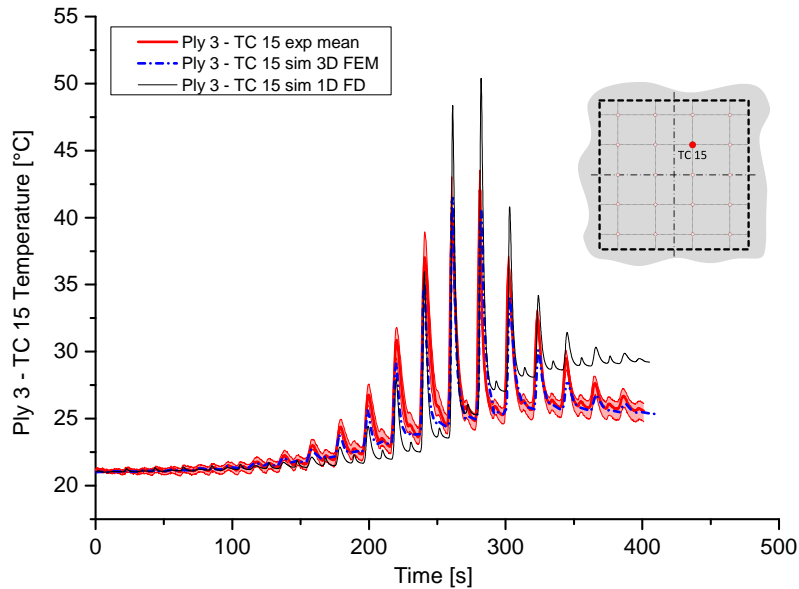
Figure 4.14. Bulk temperature of TC 15 during placement of ply 3, compare Lichtinger et al. [28]

Figure 4.15 shows temperatures $12\,°C$ less than during placement of ply 3 in Figure 8, and local temperature spikes during placement appear smoother. Again simulation results of the 3D model show good agreement, although maximum temperatures are not captured as accurately.

During the experimental placement of ply 10, the setup did not get sufficient time to reach ambient temperature (Figure 4.16), as perhaps would be expected in some production style phases of manufacturing, and so the experimental data was shifted by $1.5\,°C$ to account for that. Due to the high temperature difference between IR lamp and substrate surface, it is assumed that the temperature shift has negligible influence on the general temperature gradients. The maximum bulk temperature of $28\,°C$ was less than during the layup of ply 7, and the temperature difference between each sequential pass was smoother. 3D simulation results show good agreement, whereas the 1D model underestimated the temperature prior to passing of the measurement spot, and overestimated it for the rest of the ply.

Experimental testing allowed for the bulk temperature distribution across the area of the tool surface to be captured during the placement of the plies. This enabled a detailed analysis of temperature variations across the tool surface. Evaluated parameters were maximum temperature perpendicular to the placement path, as well as the final temperatures for each TC.

Figure 4.17 depicts four perpendicular lines of paths at maximum temperature and the final temperature at the end of the placement for ply 3. The starting point of
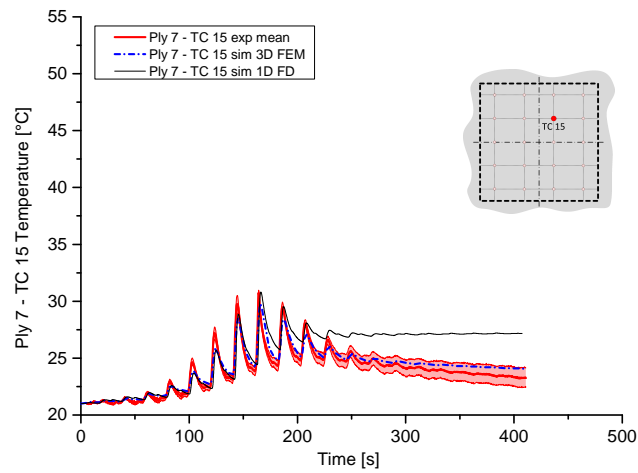
Figure 4.15. Bulk temperature of TC 15 during placement of ply 7, compare Lichtinger et al. [28]
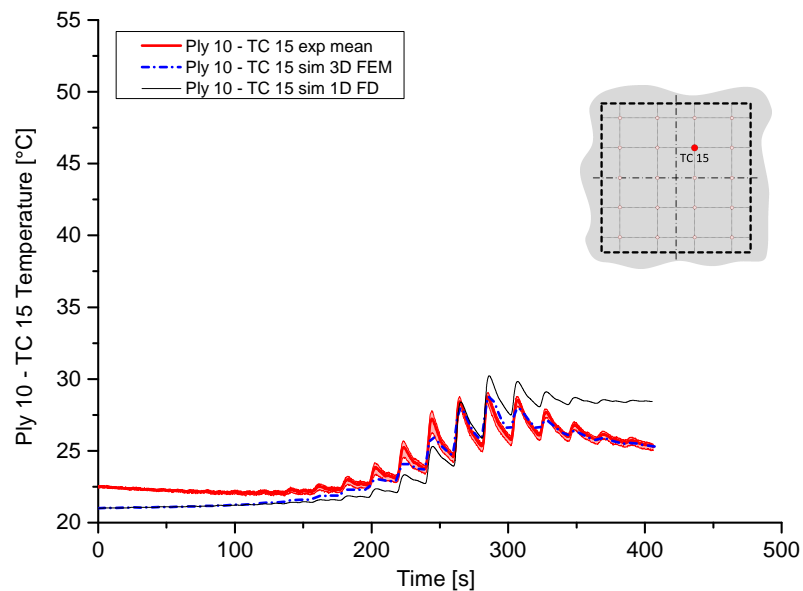
Figure 4.16. Bulk temperature of TC 15 during placement of ply 10, compare Lichtinger et al. [28]

the placement for ply 3 was the corner adjacent to TC 01. The maximum placement temperature increases with the advancing number of finished paths, and then converges. The final temperatures of ply 3 were evenly distributed perpendicular to the path direction, but elevated compared to the starting temperature. It is worth noting that there was a temperature gradient along the path length. Temperatures were higher at the beginning of the paths than at the end, so creating a 2D temperature gradient across the layup area.
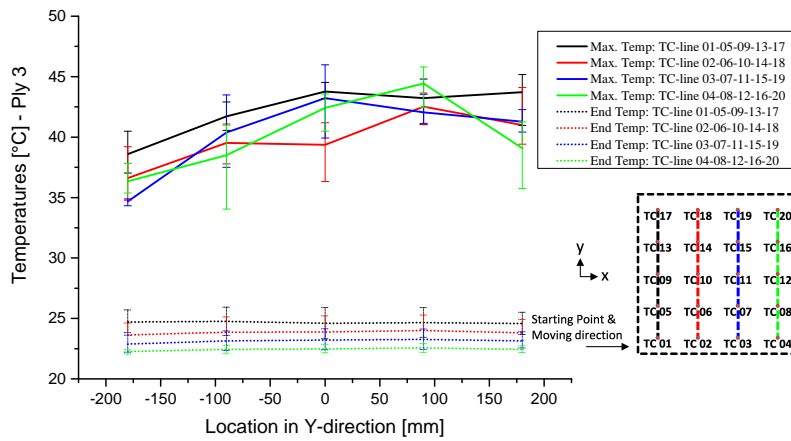
Figure 4.17. Max. and end temperature of ply 3 distributed over the placement area, compare Lichtinger et al. [28]

Figure 4.18 shows maximum and final temperatures of ply 7. The starting point for ply 7 was the corner adjacent to TC 20. Again, temperatures increased with progressing paths, and the gradient parallel to the path direction was apparent on the maximum temperatures. The final temperatures have a distinguished gradient perpendicular to the path direction, but no temperature deviations along the paths.
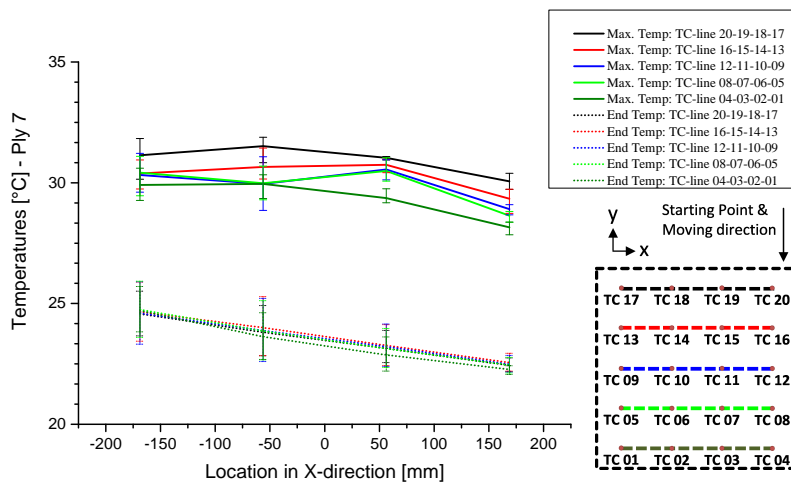
Figure 4.18. Max. and end temperature of ply 7 distributed over the placement area, compare Lichtinger et al. [28]

The maximum and final temperatures during placement of ply 10 are depicted in Figure 4.19. There is a distinct temperature gradient for both maximum and final temperature, depending on the advancing paths.
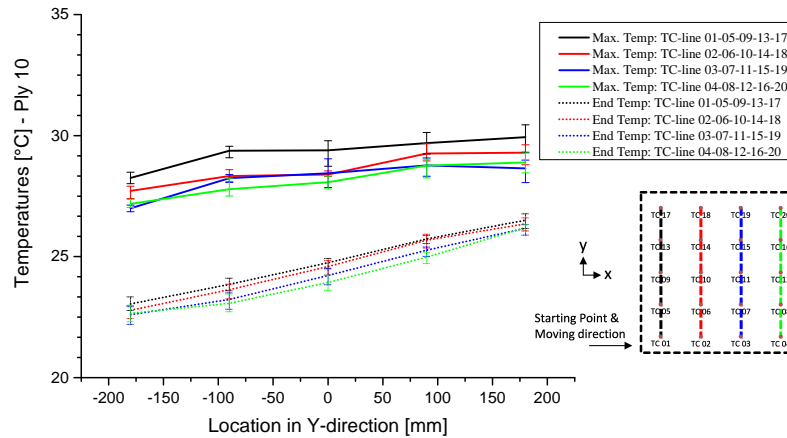
Figure 4.19. Max. and end temperature of ply 10 distributed over the placement area, compare Lichtinger et al. [28]

Shown measurements show the placement of individual plies, with an allowed cool-down period between every ply. In an industrial scale placement process this cool-off period may not be integrated for production reasons or efficiency. Therefore, after one ply is completed, the immediate start of the placement fo the subsequent ply follows. As the temperature gradient still exists from the placement of the previous ply, the quality of the process may be affected. Further work is necessary to quantify these effects. A detailed discussion on the implication of temperature control for path planning strategies can be found in Section 4.6.3 of this chapter.

4.5.1.2. Bulk temperature during placement of the centre path

Bulk temperature was measured between ply 1 and ply 2. Measurements were evaluated during the placement of ply 3, which is a 0° ply.

Figure 4.20 depicts the bulk temperature measured at TC 12, compared to 1D, 2D and 3D simulation results. At the beginning the experimental temperature is elevated due to previous heat input.

The 1D simulation results show delayed response of temperature by 0.2 s, which was expected because of absent in-plane heat flow. Further the 1D results show the highest magnitude of temperature with a deviation from experimental results of 51.5 °C, 49 % compared to initial temperature, as well as slower cool-down due to the inability of conducting heat in-plane away from the measurement point.

The 2D simulation results show accurate response in temperature rise, as heat flow in fibre direction is possible. The temperature magnitude is 2.7 °C below the 1D simulation results, and 6.4 °C above experimental values. The cool down phase is

mostly influenced by the advancing current ply at ambient temperature, which adds constantly a thermal sink into the system, therefore cooling it. With the 2D assumption the cooling effect adds overly proportional thermal mass to the model, therefore the cool-down phase is over-predicted.

The 3D thermal FEM model shows accurate results in temperature rise. The magnitude is 5.9 °C below 1D and 3.2 °C below 2D results respectively. Nevertheless, the maximum temperature is over-predicted by 3.2 °C compared to experimental results. The final temperature of the 3D simulation results agree well with experimental values.
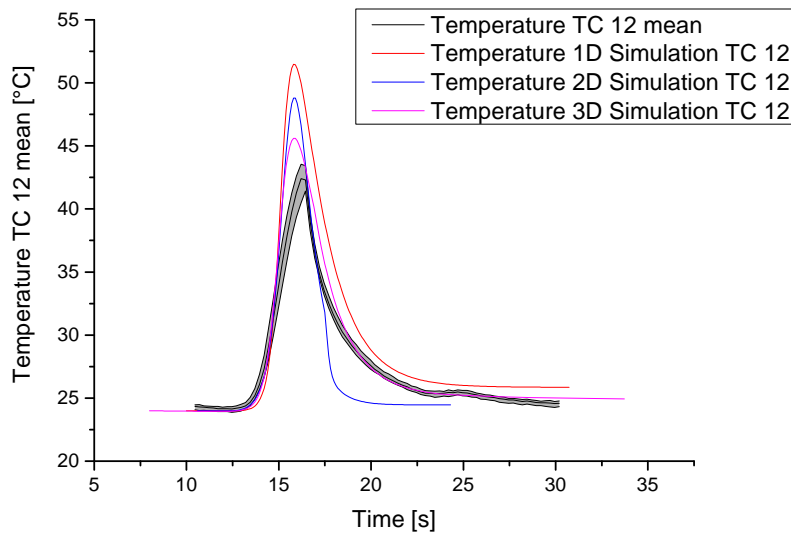
Figure 4.20. Ply 3 Bulk temperatures of TC 11

These results show that the influence of the compaction roller as well as the continuously placed tapes with increasing amount of plies needs to be further evaluated.

4.5.1.3. Surface temperature

Surface temperatures were evaluated experimentally using infrared thermography. The camera was mounted to the placement head. A path perpendicular to the placement path was evaluated and compared to simulation results.

Surface temperature perpendicular to path direction   Figure 4.21, taken out of Lichtinger et al. [28], shows the surface temperatures during the placement of ply 3 in the middle of the ply during path 10, compared to simulation results. Temperature magnitudes as well as the gradients right and left to the placement path are in good agreement to simulation results. However the measured temperatures on the placement path are over predicted due to the fact that the IR lamp is reflected on the placement head, and added to the measured value of the thermal camera. It is

assumed that the noise in the measurements arise from insufficient contact to the plies beneath, therefore heating up the top plies higher than normal.
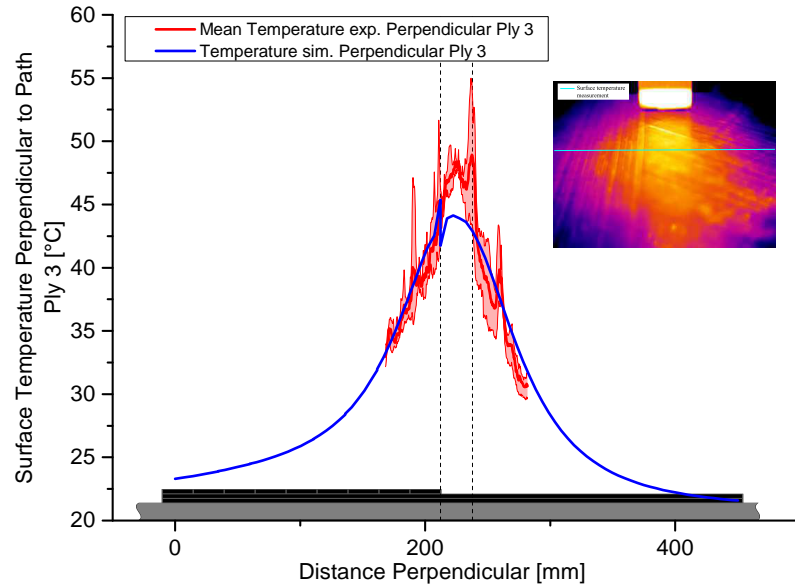
Figure 4.21. Results of Thermography and simulation of surface temperature during the placement of ply 3 [28]

Equivalent results are shown in Figure 4.22, which compared experimental values to simulation results during the placement of ply 10. Again, simulation results show good agreement to experiments next to the placement paths, and experimental values are over-predicted by 3.2 °C on the placement path.

Maximum surface temperatures during the placement of ply 3 and ply 10 differ by 3.9 °C experimentally and by 5.1 °C in simulation. At the placement of ply 10, the temperature gradients perpendicular to the placement path is steeper, due to the higher maximum temperatures.

Temperature in path direction The temperature in path direction is depicted in Figure 4.23. As soon as the entry of the radiation sphere is reached, the temperature starts to rise. At the point of the maximum view factor, the temperature rise has its highest derivative, but has not reached maximum temperature. The point of maximum temperature is at the equilibration between heat dissipation into the tooling and heat flow into the surface from the IR lamp. After this point, the temperature reduces up to the nip point.

The process should be adjusted so that the highest surface temperature is at the nip point. This is not the case in current configuration.
The point of highest temperature is, among other factors, highly dependent on:

- Tool material,
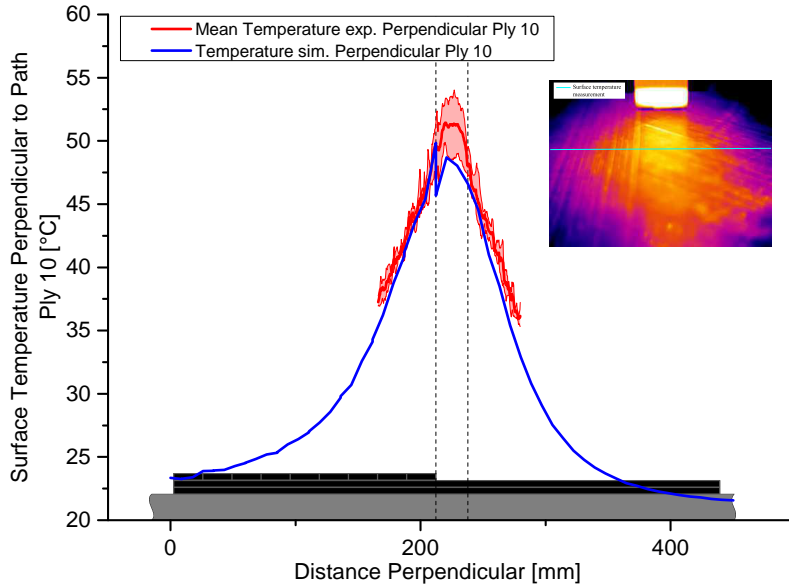
Figure 4.22. Results of Thermography and simulation of surface temperature during the placement of ply 10 [28]
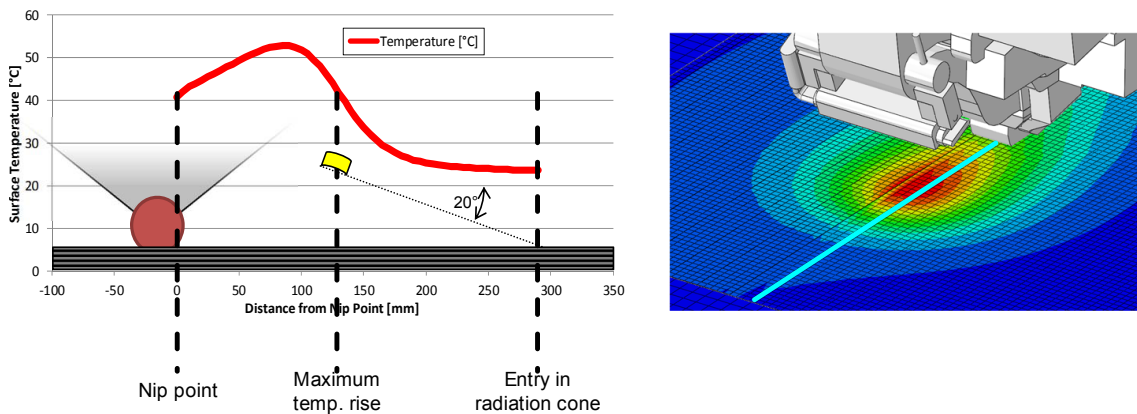
Figure 4.23. Temperature along the path direction from simulation (left) and evaluation path (right)

- Amount of plies already placed,

- heat output of the lamp,

- orientation and position of the lamp with regard to the nip point, e.g. the view factor and

- deposition material.

Therefore, for the prediction of maximum temperature, and an adjustment of the process variables so the point of highest temperature is close to the nip point, it is imperative to consider above mentioned process variables.

Radiation distribution   The 3D FEM model opens the possibility of complete overview of the radiation distribution between all surface elements. So the irradiated heat from the IR lamp can be quantitatively evaluated between individual portions of the model.

With the lamp power output of 318 W and a efficiency of 90 %, the radiation power output of the lamp is 286.2 W. With the emissivities of the tool of 0.3 and the substrate of 0.9, radiation heat input in the plies as well as the tool surface can be evaluated.

Figure 4.24 depicts the radiation distribution at the time step when the IR lamp is at the centre of the ply.

- Electrical Power Uptake of the IR lamp: 318 W
- Efficiency: 0.9
- Radiation power: 286.2 W

- Emissivity:
  - Tool: 0.3
  - Tapes: 0.9

Radiation input on path:
44.5 W   = **15.55 %**

Radiation input adjacent to path:
175.8 W   =   61.44 %

Radiation to ambient:
65.87 W   =   23.01 %
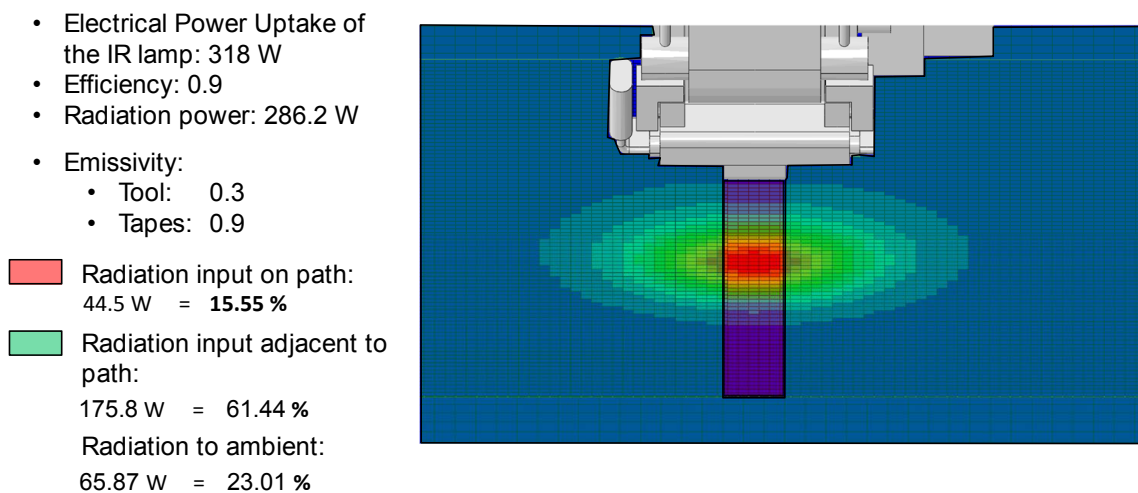
Figure 4.24. Radiation distribution as simulation result

15.6 % of incident energy is actually input on the placement path, therefore contribution to wanted elevation of temperature. However, 61.4 % is radiation input adjacent to the paths, therefore contributing to unwanted temperature elevation and ageing of the already placed substrate. 23.0 % is irradiated to the ambient environment.

4.5.2. Placement on a tapered honeycomb

4.5.2.1. Experimental results

The Figure Series 4.25 shows the temperature measured with the 20 TCs along the path. The first five TCs are fixed on the six plies in front of the honeycomb, 15 TCs are fixed on the tapered honeycomb. Mean values are displayed in bar graphs at the location of the actual TCs. For clarity error bars were omitted.

With the rotating movement of the robot at the crossover from flat surface to the tapered honeycomb, the IR lamp irradiates the first portion of the top of the honeycomb for a longer time. This increases the temperature disproportionately at this area. When the roller reaches the top of the ramp, it speeds up to reach the programmed velocity, therefore reducing heat input under the IR lamp, as it has less time to act on the surface. The backwards ramp of the honeycomb experiences a higher view factor, as it is almost parallel to the IR lamp, and therefore also experiences a disproportional high temperature rise. The temperature of TC 11 is depicted in Figure 4.26, along with the signal of the light barrier. With the reduced emissivity of the adhesive film maximum process temperature during first ply is at 63 °C, while temperatures reach 90 °C during following paths. It is worth noting that the maximum temperatures appear to stay constant during the placement of ply 2 - 5, with slightly reduced maximum temperatures at later plies.

At these elevated temperatures of up to 90 °C, typical aerospace grade prepregs start to experience the start of cure reaction. Further, with prolonged exposure to high temperatures, the material will be artificially aged, therefore reducing material life. These risks are discussed in detail in Section 4.6.2 of this chapter.

Figure 4.27 depicts the maximum temperatures during the placement of each ply.

As expected, highest temperatures are at the first part of the top of the honeycomb. The IR lamp has the maximum dwell time at this location, as the roller crosses over from the flat aluminium tool to the tapered section of the honeycomb.
Maximum temperatures for ply two to five are all within error limits, concluding that the thermal contact resistance between the adhesive film and honeycomb as well as the thermal conductivity of the honeycomb itself are the main drivers for temperature maxima, and thermal conductance of the tapes and thermal contact resistance between tapes have a negligible effect.
The maximum temperatures for ply 1 is 64.3 °C, 74 % of all further plies with 86 °C. That is due to the emissivity of 0.65 of the adhesive film compared to the emissivity of the black tapes of 0.90.
The first five TCs are fixed to the layer of six tapes in front of the honeycomb. There a distinguished temperature gradient is visible over the amount of placed plies. At
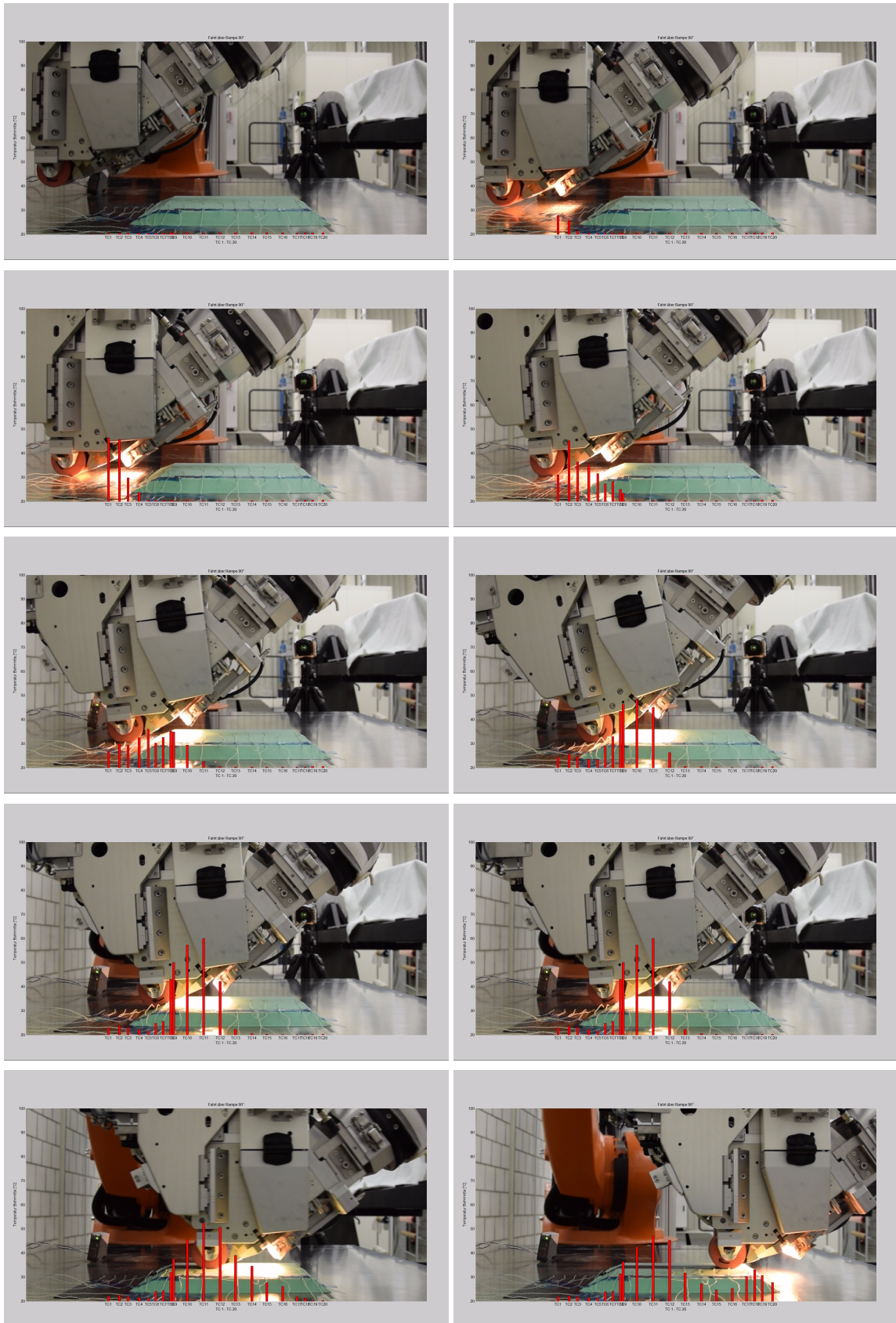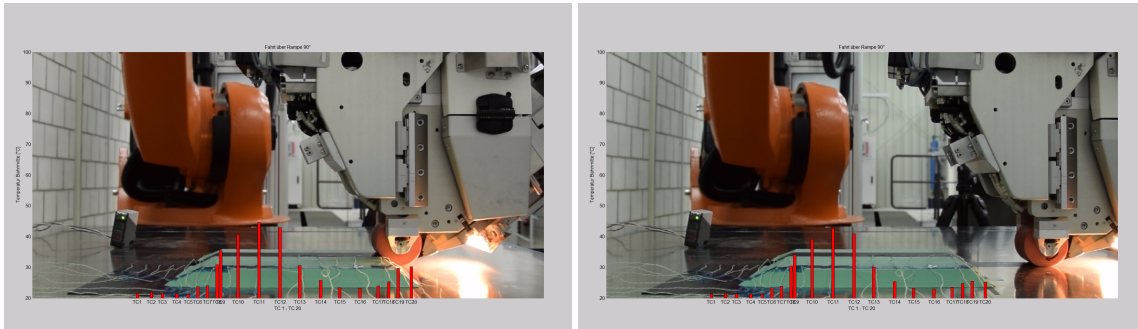
Figure 4.25. Series of images showing the temperature distribution along the placement path on the honeycomb during the placement of the first path
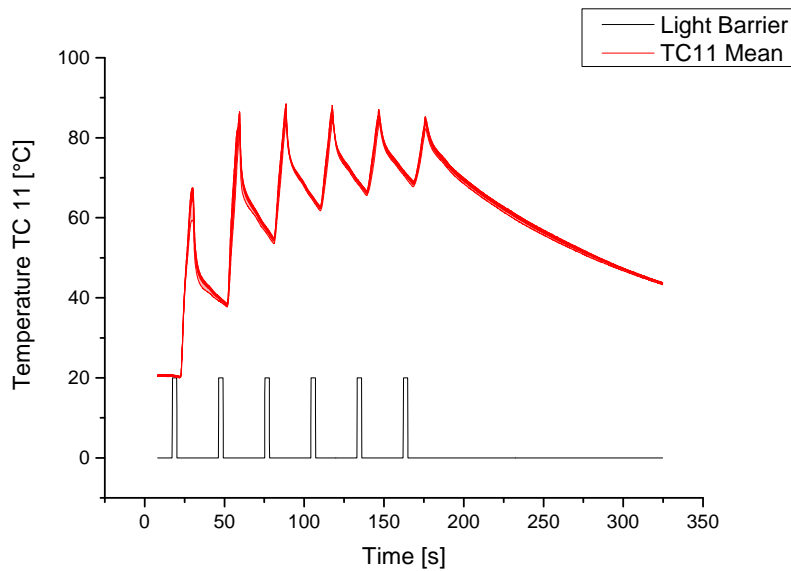
Figure 4.26. Experimental temperature of TC 11 during placement of all plies
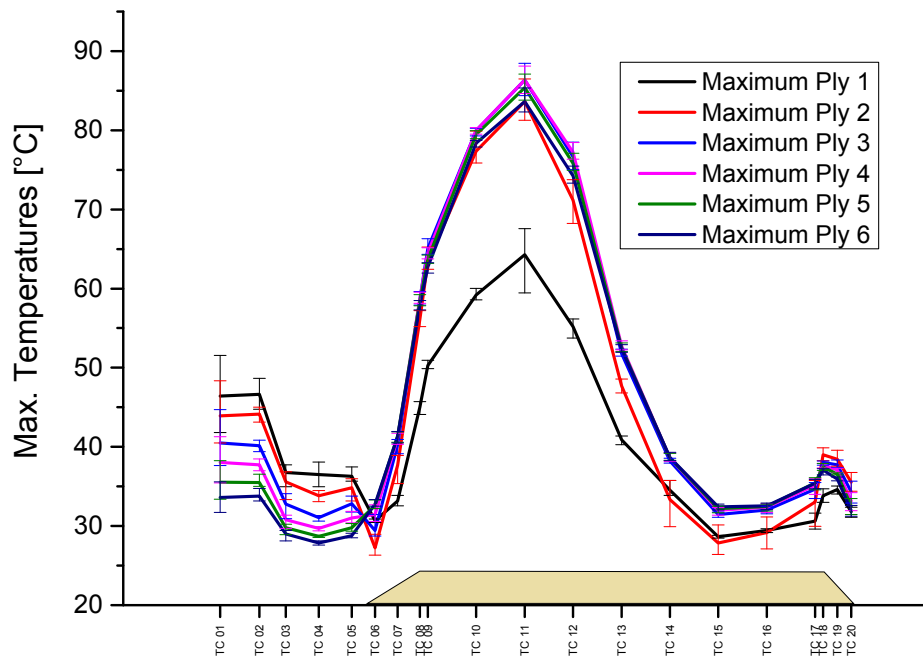
Figure 4.27. Maximum temperature values for all plies

the placement of ply 1 the temperatures start with 47 °C. With each further ply the maximum of TC 1 temperature drops. Therefore it becomes apparent that the main driver for maximum temperature here is thermal conductance as well as thermal contact resistance between tool and the first ply. With the higher thermal mass of the aluminium flat tool, the maximum temperature is considerably lower that at the honeycomb section. TC 1 and TC 2 experience higher maximum temperature then TC 3 - 5. This due to the fact that TC 1 and TC 2 are irradiated prematurely before the placement head starts to move along its path direction. The IR lamp is switched on, 1.00 s before the roller touches the tool, and 1.72 s before the placement head starts to move along the path. As the placement head accelerates, TC 3 - 5 have a decrease in maximum temperature.

Figure 4.28 shows the temperature values for all plies at the end of the placement of each ply. As the test setup cooled off during movement of the placement head, the main drivers for the heat dissipation become apparent. The general trend of the temperature distribution along the placement path stays comparable to the maximum temperatures. Highest end temperatures are at the first portion of the top honeycomb section. However, there is a distinct gradient of end temperatures over the number of placed plies. At the end of ply 1 the temperature of TC 11 is 40 °C lower that at the end of ply 6. On the one hand this is due to the lower emissivity of
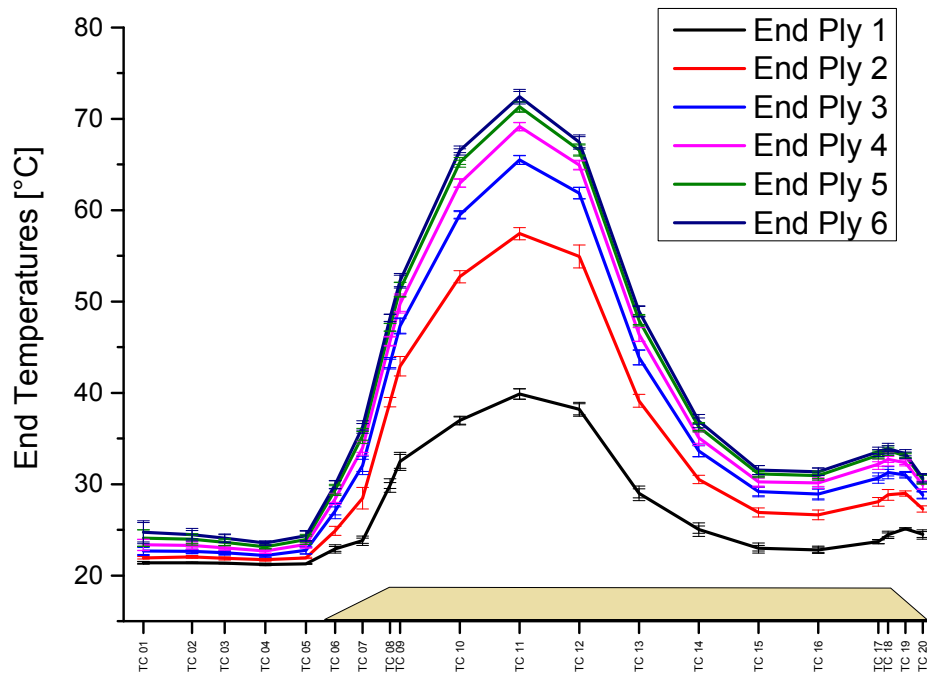
Figure 4.28. Temperature values of all TCs at the end of each ply

the adhesive film, and therefore lower maximum temperatures. The second reason for the temperature gradient over amount of plies there is more thermal storage within the plies, therefore concluding that one driver for the end temperatures is contact conductance as well as conductance within plies. Third reason for the gradient in end temperatures is the continuous placement process. The maximum temperatures are cooled off when the roller presses the new tapes against the substrate. Therefore the temperature of the roller as well as the temperature of the new tapes play a role that is yet to determine.

4.5.2.2. Surface temperature

Figure set 4.29 shows the placement of ply 1, with emissivity fixed to 0.65. As detailed in Section 4.5.2.1 the maximum temperatures occur at the first part of the top of the honeycomb.

As the head progresses, with increasing speed the surface temperature reduces. At the ramp down section temperature is disproportionally high due to the higher view factor.

Figure 4.30 shows the surface temperature at the location of TC 11 over time. The six temperature peaks along with the six plies are clearly visible. The disproportional
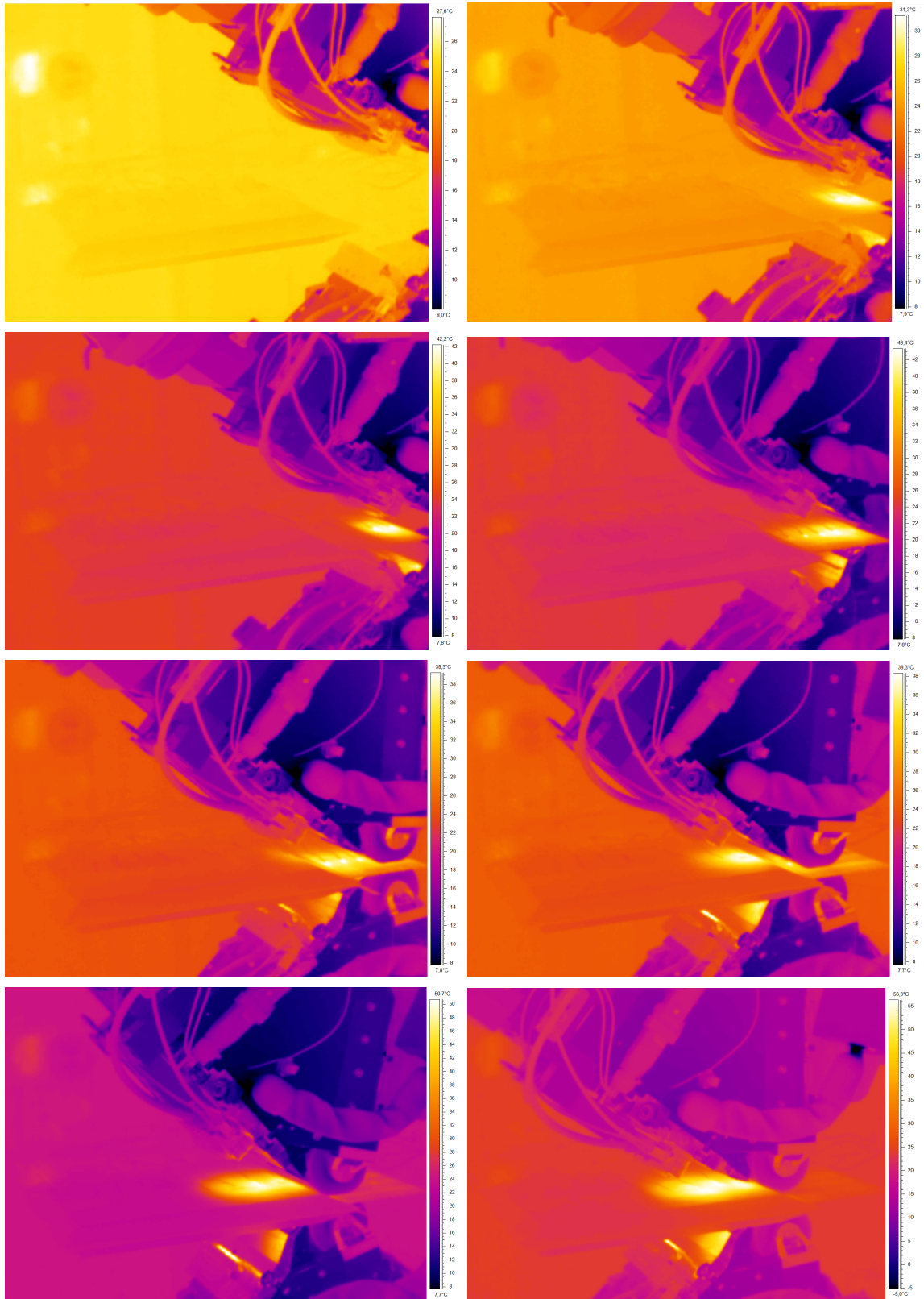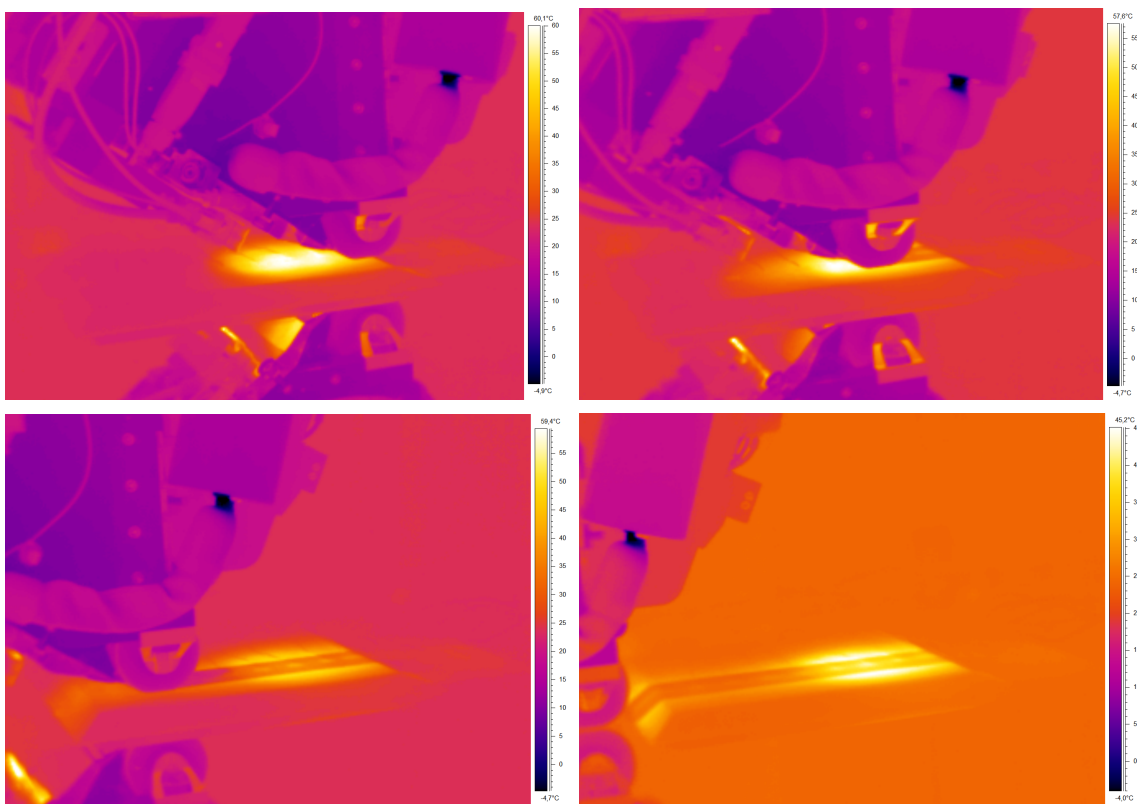
Figure 4.29. Series of images showing the surface temperature during the placement of the first path

large temperature drop occurs as the compaction roller conceals the evaluation point. Therefore that portion is excluded from evaluation.

The emissivity is set to 0.65 up to time 25 s - until the first pass of the roller - and then set to 0.90 to account for the emissivity differences between the adhesive film and the slit-tapes.

The surface temperature reaches 71.1 °C at first ply. During placement of second ply the surface temperature reaches 101.2 °C, an increase of 42 %. From ply three onwards the surface temperature stays constant with 86 °C.

It is presumed that the disproportionally large temperature increase during ply 2 is caused by insufficient tack of the first layer, and therefore highly increased thermal contact resistance.

The temperature drop after passing of the roller is of significance, as this shows that the roller along with the newly placed tapes are a major factor in temperature drop on the honeycomb. After passing of the roller the temperature reduces further through conduction, although this effect is considerably slower than through temperature drop of the roller.
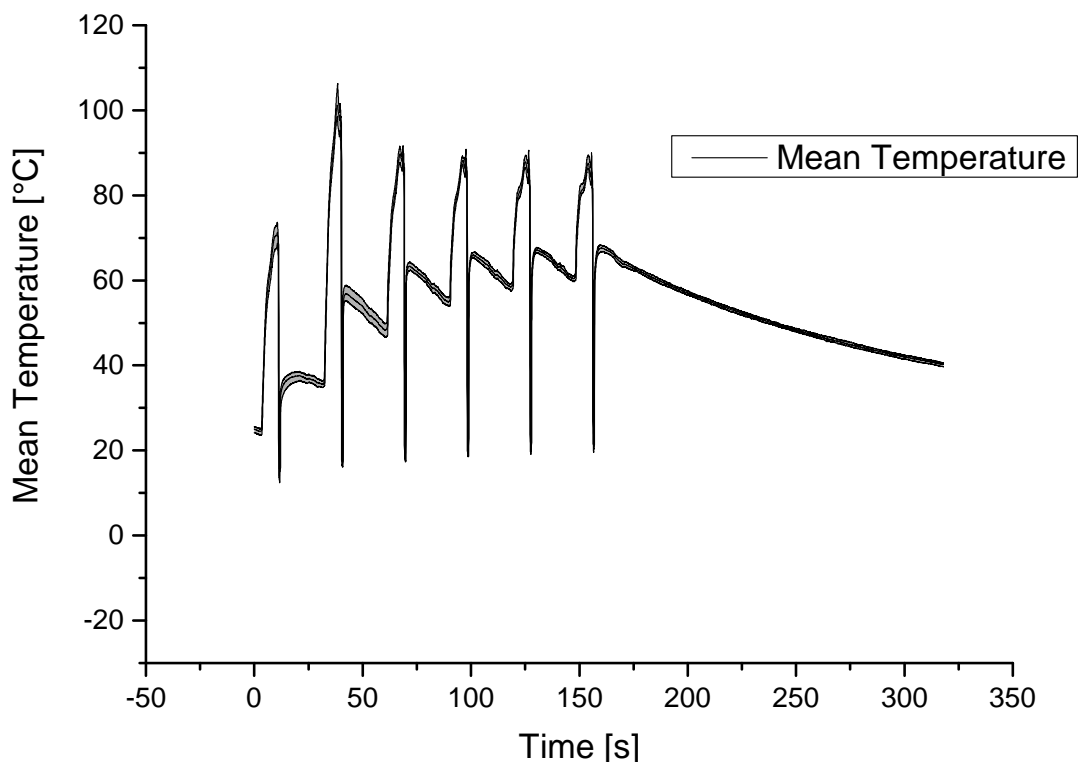
Figure 4.30. Surface temperature spot at location between TC 10 and 11 during the placement of all plies

After the end of the placement the test setup was allowed to cool off, therefore evaluating the temperature drop over a prolonged period of time. The end temperature

of the surface after the placement of ply 6 was 70 °C. After 160 s cool-off time the surface temperature was still elevated at 40 °C.

The surface temperature perpendicular to path direction 8.0 s after movement start of the head is displayed in Figure 4.31.
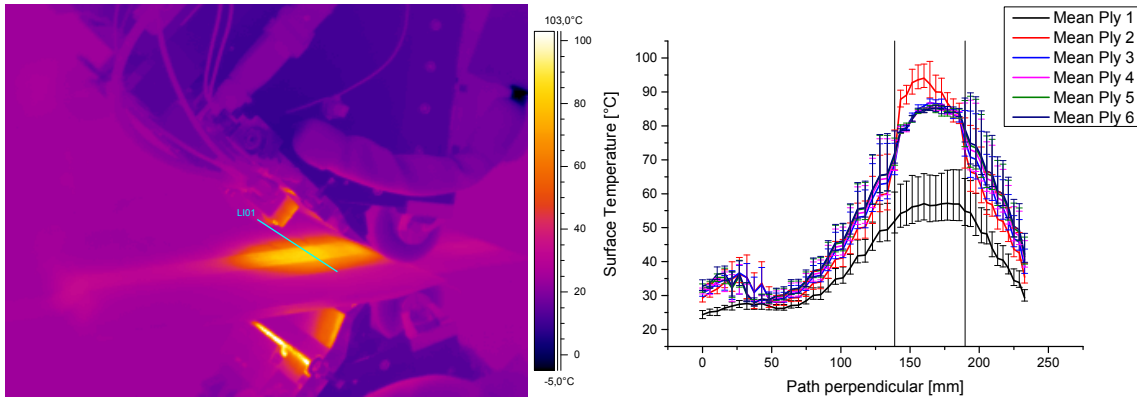
Figure 4.31. Surface temperature perpendicular to path direction (right) for all six plies (left)

A gradient surface temperature is clearly visible, with the heated area not delimited to the actual placement line. Highest temperature is directly at the centre of the path, with gradients towards the outer edges of the honeycomb.

4.5.2.3. Simulation results compared to experimental values

In the following simulation results are shown, compared to the experimental values when appropriate.
Figure 4.32 shows the simulation result of the thermal simulation 8.0 s after movement start of the head during first ply. The motion of the head is a direct input from the video analysis.
It is apparent that the area of maximum temperature lies underneath the IR lamp. At the nip point section the temperatures are greatly reduced.
Elevated temperatures are visible at the touch down point of the head, as the IR lamp has increased dwell time on that specific area.

Figure 4.33 features the experimental values of TC 11 compared to the simulation result of the node at the location of TC 11.

It is apparent that the maximum peak during the placement of the first ply is in good agreement between simulation and experiment, with 3.5 °C difference. The cool-off after ply 1, however, is over-predicted in the simulation, with a resulting difference of 6.0 °C (28.7 % compared to initial temperature). The temperature increase during the placement of ply 2 is then under predicted. This effect continuous up to ply 6, with increasing temperature difference between simulation and experimental values.
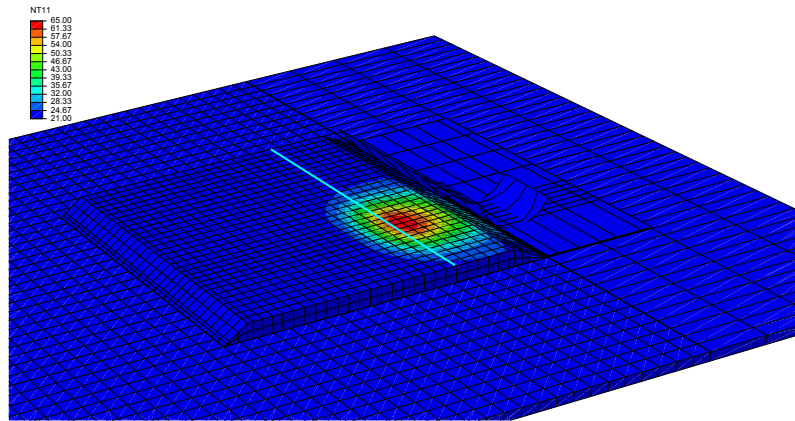
Figure 4.32. Plot of the simulation result in the Abaqus CAE environment 8 s after placement start with perpendicular temperature evaluation path
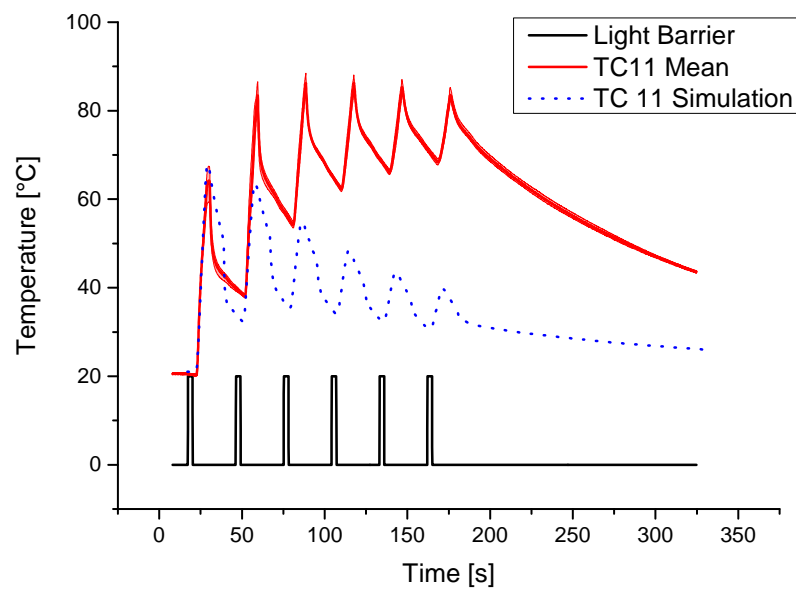
Figure 4.33. Experimental values compared to simulation results at TC 11

However, comparing not the absolute temperature values, but the relative temperature differences between cool-off and temperature rise ΔT, the difference between simulation and experiment at TC 11 lies between $2.9\,°\mathrm{C}$ at first ply and $-9.7\,°\mathrm{C}$ at second ply, with the difference reducing with increasing plies. (compare Figure 4.34.
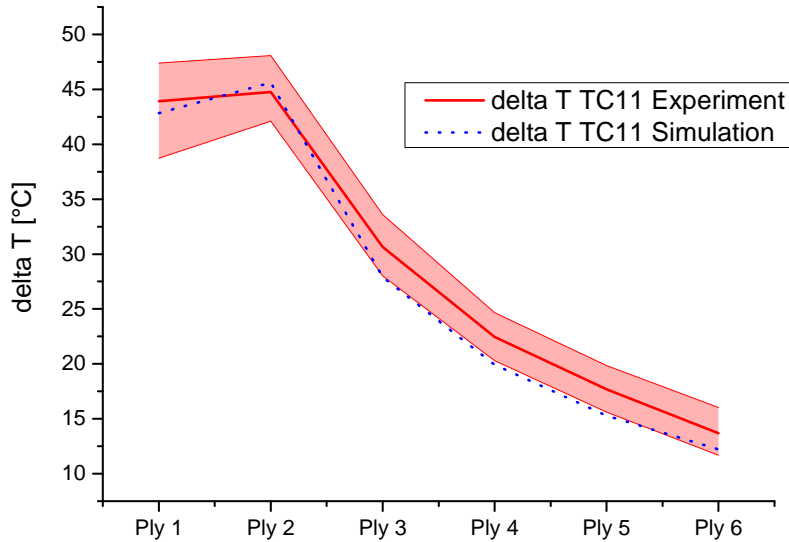
Figure 4.34. Temperature differences while passing of the IR lamp for all six plies: experimental values compared to simulation results

Figure 4.35 depicts the maximum process temperature during the placement of ply 1 in comparison between experimental and simulation values. As the cool-off phase is not accurately predicted with the pure thermodynamic model, solely temperatures during the first ply are compared.
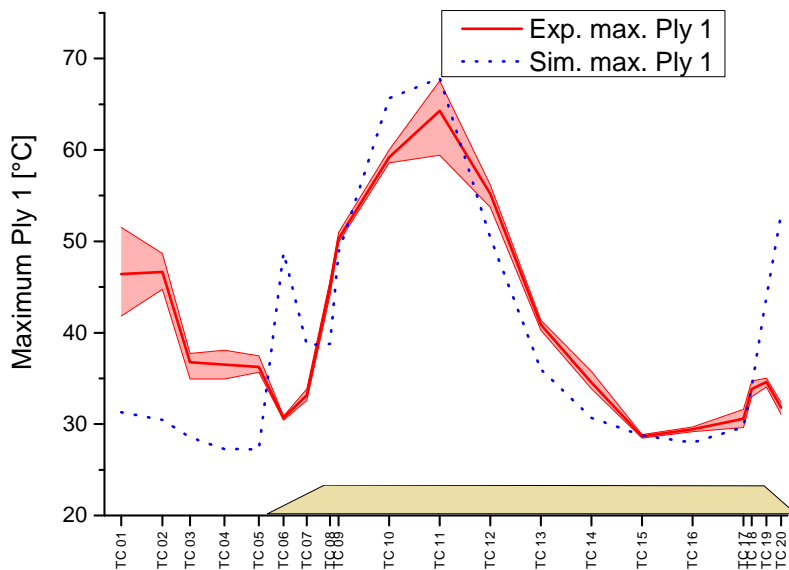
Figure 4.35. Maximum temperature values during the placement of ply 1 for experimental and simulation results

The temperatures on the honeycomb are with good agreement, however the temperatures on the tape stack in front of the honeycomb are under predicted. It is assumed that the fixture method falsifies the results, as hot spots appear on the thermal camera images at the spots of the TC measurement points. Further, the simulation results at the bottom of each ramp of the honeycomb highly overshoots the measured values. It is presumed that with the little honeycomb thickness thermal conductivity is highly influenced during the experiments. This fact was not modelled, therefore creating these temperature over shoots.

Figure 4.36 shows the surface temperatures 8 s after movement start of the first ply, compared to experimental results. The predicted temperature lies well within error limits at the path centre. However, temperatures are underpredicted left and right of the path, indicating a too little in-plane heat flow.
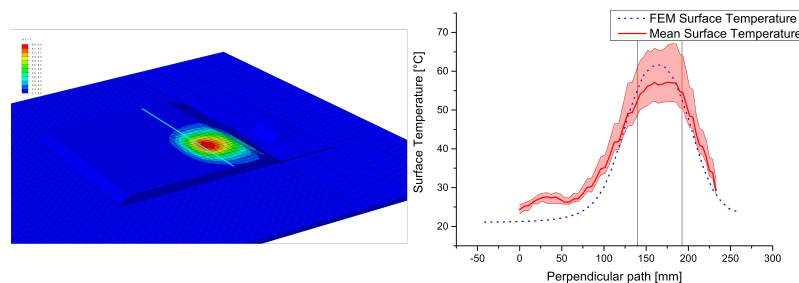
Figure 4.36. Surface temperature during placement of ply 1, 8 s after movement start

This concludes that the discontinuous method of the purely thermal simulation, without the effect of roller contact and continuous feeding of the tapes, is appropriate for the evaluation of temperature differences. However to accurately capture cool-off effects, further models have to be developed, including roller contact and continuous feeding of the tape.

4.6. Discussion

4.6.1. Influence of process parameters

The machine and process parameters

- heat output of the IR lamp,

- deposition material properties,

- tool material properties,

- deposition velocity,

- position and orientation of the IR lamp and

- process kinematics

have high influence in process temperatures.

When the velocity is reduced, and the heat output of the IR lamp is not adjusted accordingly, the heat input is inverse proportional to the velocity, i.e. the radiation dwell time. The orientation and position of the IR lamp influences the area of heat input, as well as the magnitude through the view factor. With different deposition materials and different tool materials along with varying material properties, temperature dissipation may vary significantly.

Parametric studies were conducted with the simulation models to conclude to the sensitivity of the process parameters. The results are depicted in Figure 4.37.
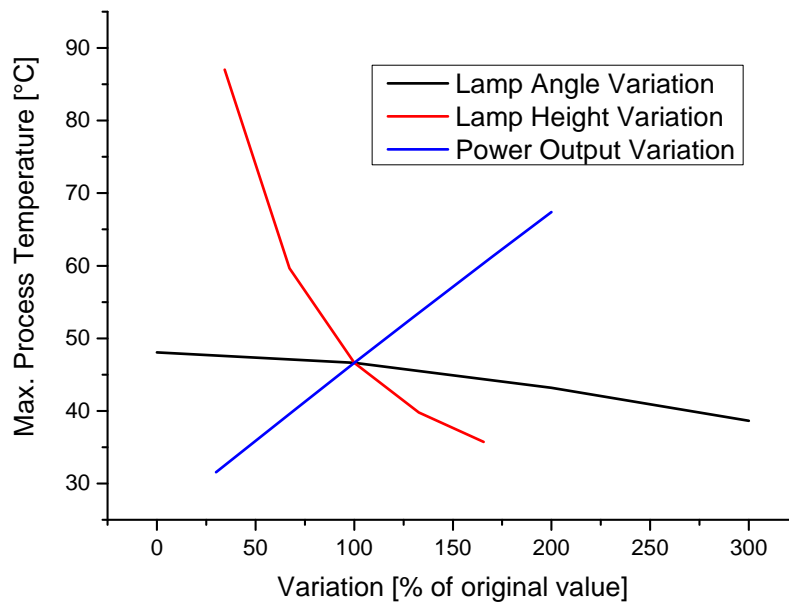
Figure 4.37. Process parameters variations for lamp angle, lamp normal height to the substrate and the lamp power output

The lamp angle has little influence on maximum temperature, however when the lamp angle changes further, the substrate will not be irradiated and process temperature will decrease disproportionally. There is an linear relationship between power output of the lamp and an inversely proportional relationship of lamp height to maximum process temperature.

4.6.2. Process temperature influencing material life

4.6.3. Process temperature as input for path planning strategies

Measured and simulated results show that thermal history during the layup process must be taken into account. There is a distinct temperature gradient along the

sequence of the paths in the bulk material. This needs to be considered for the planning of multi-angle layups. Depending on the starting point of each path, substrate temperatures are dependent on the previously placed plies. For several successive plies, there is a chance that this effect will multiply and therefore the danger of hot spots increases, resulting in material degradation or cold spots, with insufficient tack. Regarding the deposition strategy, e.g. linear or chaotic deposition, results will be different depending on the sequence of the paths. Its is presumed that a general chaotic layup strategy will reduce the temperature gradient effects and may generate an even temperature distribution on the tool surface.

On complex tool geometries it may be necessary to plan the complete layup according to thermal properties of tool and material, to avoid excess or unevenly distributed temperatures.

Depending on the placement algorithm and the AFP machine settings, the IR lamp is switched on during lift-off of the previous path and touch-down to the tool of the next. Usually the AFP head has a very low velocity just before touch-down and some preprogrammed dwell time at the touch-down point. When the IR lamp is switched on, there is an influence on the substrate temperature. On the one hand this can be used to counter tack problems at the starting points of the path but on the other, as this effect creates a temperature gradient along the direction of the paths which has to be taken into account concerning hot spots and tack effects for multi-angle layups.

It is therefore imperative for the path planning to take thermal management into account, i.e. by offline thermal prediction or experimental measurements.

4.6.4. Effects of simplifications and validity of the models

The purely thermodynamic simulation models neglect important aspects of the AFP process, and therefore the results are influenced by these effects. The effects of the compaction roller, along with its pressure distribution and its cooling or heating effects is not considered. For an aluminium tooling the pure thermal model was proved to be valid. For the honeycomb test setup, where the roller contact plays an important role due to the reduced cool-off, the simulated temperature magnitudes are valid solely for the first passing of the head, and the cool-off phase is not predicted correctly.

With the neglect of the pressure compaction roller, a thickness change of the placed tapes is also omitted, and therefore the changed material thickness and density of the tapes. In the further Sections these effects are discussed in detail.

4.6.5. Temperature dependent and pressure dependent contact

According to Madhusudana [90], heat transfer through a joint depends on surface roughness, hardness, and conductivity of both joined materials. Moreover thermal contact is highly dependent on the contact pressure as well as temperature due to the viscoelastic behaviour of the resin. Levy et al. [92] found the intimate contact between two thermoplastic tapes to be highly dependent on both pressure and temperature.

Within this work, thermal contact is neither temperature nor pressure dependent. As the compaction roller has contact with the substrate, the normal pressure improves intimate contact, and therefore contact conductance. In combination with local temperature increase with decreased viscosity of the resin, contact is assumed to improve. With the placement of more than one ply, when the compaction roller passes the area more than one time, contact will further be affected.

Usually in an industrial application, after a certain number of plies, the layup is debulked to allow for good layup quality. Depending on number of debulking cycles and debulking time, contact efficiency may vary.

Within the thermoset AFP process, thermal contact conductance is assumed to be dependent on following parameters:

- Local roller normal pressure distribution

- Set compaction force of the AFP machine

- Layup velocity, therefore pressure application time

- Number of plies along with number of passings with the compaction roller

- Debulking time and total layup time

- Amount of debulking cycles

- Process temperature history

- Local temperature during application of pressure

Due to the computational efficiency of the 1D model of the flat placement, it was used in this work to calibrate thermal contact conductances between the tool and the first ply, h_{TP}, as well as between each ply, h_{PP}. A parametric study was conducted and the values were found by aligning local maxima and minima of the temperatures to the experimental values.

4.6.6. Temperature influence of the compaction roller

The compaction roller has major influence on the AFP process. Its pressure distribution and its conformity allow the tapes to stick to the tool surface.

The tool surface or already places substrate experience elevated temperature due to the heat input of the IR lamp. When the roller then contacts the surface, it is also heated up through conduction. In the same process the substrate is cooled off as the roller and the substrate / tool balance their stored energy.

In an industrial scale thermoset AFP head the compaction roller is cooled by a stream of cold air. However this cooling is limited, so a constant increase of temperature in the compaction roller was experienced during the testing.

As the roller is not represented in the purely thermodynamic models, these effects are neglected. As proven in Section 4.5.1, that simplification is valid for tools with higher thermal mass then the roller, i.e. the aluminium tool. However, the honeycomb with different thermal properties it was found that the cool-off effects of the compaction roller has a significant influence and cannot be neglected.

The temperature increase and peak temperatures are driven by the heat source interacting with the substrate in front of the nip point. Therefore peak temperatures during one passing of the head can be accurately predicted. The cool-off phase must be regarded with great care, especially with follow up passes of the placement head.

4.6.7. Design of the heat source

As mentioned in Section 4.5.1.3 of this chapter, solely 15 % of the radiation output of the IR lamp arrive at the placement path. 95 % of power are either absorbed by adjacent paths or the tool, or are emitted to ambient. This leads to the conclusion that an IR lamp may not be an adequate heat source for the AFP process. Its diffuse characteristics delivers heat into parts where no heat is needed, and this may lead to negative effects like artificial ageing or even partial cure [28]. The uneven distribution of heat elevates the temperature of the tool and substrate unevenly, and creates temperature gradients across the tool surface.

Therefore it is concluded that a directive, regulated heat source is needed, that is able to irradiate defined portions of the tool surface. In thermoplastic AFP laser heating is the common chosen heat source, as it may be controlled efficiently, and allows for a directed heat input. However, the drawbacks of laser heating are the safety requirements, as well as the initial cost of investment, therefore it is infeasible for thermoset AFP. A further possible heat source may be IR LED heating [101].

As proposed earlier the compaction devise may incorporate the function as a heat source. However, care must be taken that tack is enhanced on the opposite side of the tape, in contact to the tool surface, so the tapes do not stick to the roller surface.

4.6.8. Control of temperature dependent on processing conditions

The results of both experiments and simulation show the definite need for process control. In industrial AFP applications, temperature output is regulated by placement velocity at best. Neither material properties nor tool geometry is considered. Especially in the case of multi-material tooling or complex geometry such as the aforementioned honeycomb-aluminium combination, these effects influence the process highly. Therefore, process temperature needs to be controlled actively throughout the complete process.

Process temperature could be integrated early in the design process. Within the path programming software thermal simulation could be included. Then both geometry or material properties could be taken into account in terms of temperature. This implies an increased workload early in the design phase, as not only the surface geometry needs to be designed, but the complete structure of both tool and substrate to be placed as well as all material parameters. However, the benefits would by far outweigh the increased workload. Heat output could be directly controlled in relation to position of the placement head, layup rate, material properties and further process parameters.

Another possibility of the simulation models described in Section 4.3.4 is the incorporation of an temperature control feedback loop. With the known design of both tool and layup, the process temperature could be measured online during layup far ahead of the nip point. These temperature values could be used as input for online thermal prediction with resulting controlled heat output. For this the simulation needs to be faster than real time, which is the case with the 1D and 2D FD thermal model. The advantage of this method would be the direct feedback loop, therefore taking into account individual process parameter such as ambient temperature or unforeseen variables.

5. Thermo-mechanical coupled model of the AFP process

In Chapter 4: Thermal measurements and thermal models for AFP the predicted temperatures were accurate during heat up phase when compared to experimental results. However, the influence of the continuous placement process as well as the compaction roller was neglected.

Within this chapter, these influences are studied in greater detail, and a thermo-mechanically coupled model is developed which incorporates these effects.

5.1. Literature review on thermo-mechanical coupled process models for AFP

The behaviour of the slit-tapes during placement plays a certain role during placement. The in-plane bending and shear behaviour of the slit-tapes are vital for the understanding of steering effects. Due to the viscosity of the matrix system, the mechanical behaviour of the tapes is highly temperature dependent. To study the temperature dependent mechanical effects, some work is available on thermoplastic tape placement.

Sarrazin and Springer [17] study both mechanical and thermal aspects of thermoset and thermoplastic fibre placement in a sequentially coupled thermal-stress simulation model. Schledjewski and Latrille [102] propose a fundamental tool for thermoplastic AFP process simulation, which includes several components dependent on thermal and mechanical properties of fibre placement material and boundary conditions. Khan et al. [103] states that both thermal and mechanical properties affects the mechanical strength of the composite produced by thermoplastic laser assisted AFP. Chinesta et al. [88] propose a numerical reduction method to reduce thermo-mechanically coupled models for the laser-based thermoplastic AFP process, which is refined by Barasinsiki et al [104, 105] and Poulhaon et al. [106]. They study the effects of non uniform thermal contact and thermal history in laser assisted thermoplastic tape placement on residual stresses for in situ consolidation. Narnhofer et al. [86] present an overview of thermoplastic tape placement depending on thermal and pressure boundary conditions on deformation behaviour and in situ consolidation. Sonmez and Akbulut [107] opimize the thermoplastic AFP process towards residual stresses and processing speeds.

Little work is available on coupled process models for the thermoset AFP process. To

close this gap in design, a thermo-mechanically coupled process model is developed to study the effects of the sequential placement as well as deformation behaviour on temperature distribution.

5.2. Thermo-mechanical coupled model for the placement on 3D tapered honeycomb structures

5.2.1. Material model for the temperature dependent bending behaviour of slit-tapes

The behaviour of the slit-tapes during placement play a certain role during placement. On the placement of variable stiffness laminates, e.g. Blom et al. [108], the in-plane bending behaviour of the slit-tapes is important. However, for the placement on convex or concave surfaces, the in-plane properties are assumed to be of minor importance, and the bending behaviour of the tapes is dominating the tape deformation behaviour.

During the placement on concave and convex structures as is the case with a tapered honeycomb, the tapes are required to bend sufficiently to allow complete contact within all areas. When the tapes do not bend enough, the risk of bridging defects occur.

The tapes are assumed to be a temperature dependent inhomogeneous elastic material. Due to the short term application any viscous behaviour is neglected. The fibres are loosely held together by the uncured resin. The fibres have high stiffness under tensile load, but under compression stress the fibres will buckle and carry very little load. Therefore it is important that the bending stiffness of the tapes is decoupled from tensile stiffness.

To measure bending behaviour, a test rig from characterisation of drapeability of fabrics is used. The test rig is based on Peirce [109], and is fully standardized in DIN 53362 [110]. The test setup is depicted in Figure 5.1 with the design out of [110] (left) and the actual test (right).

Although this test measures the bending behaviour under self loading, and in APF the tapes experience external loading due to compaction of the roller, it is presumed the bending stiffness does not vary significantly with a variance in boundary conditions.

To evaluate the data, the line load F_{L_B} in $[N/mm]$ due to gravity can be calculated using Equation 5.1 [110]:

Figure 5.1. Test setup for the characterization of the bending behaviour of uncured prepreg material with conventions (left [110]) and the actual setup (right)

$$F_1 = g \cdot \frac{m_S}{l_S}, \tag{5.1}$$

with m_S the mass and l_S the length of the sample and g the gravity acceleration with $9.81\,\mathrm{m/s^2}$.

The bending stiffness B_1 in $[N \cdot mm^2]$ is then determined by Equation 5.2 [110] with l_{S0} the overhang length of the sample:

$$B_1 = F_{L_B} \cdot \left(\frac{l_{S0}}{2}\right)^3. \tag{5.2}$$

To determine the temperature influence on bending stiffness, the test was repeated at elevated temperatures. Six repeats of each test was made to gain insight into repeatability.

The material behaviour with decoupled bending stiffness is implemented in the commercial FEM software Abaqus CAE. There, the tapes are modelled with S4 shell elements with orthotropic material orientation. To decouple the bending behaviour, every element of the slit-tapes is copied to the same position, and the nodes of the elements merged. One element is assigned pure membrane behaviour, therefore representing the in-plane behaviour of the tape, and one element is assigned pure bending behaviour without in-plane properties.

The in-plane properties are assumed to be of minor importance during the placement on a tool surface on a path with single curvature. The material properties are taken out of Lukaszewicz [6]. He uses similar aerospace grade toughened slit-tape material. The bending behaviour is implemented in the form of an isotropic material behaviour with the temperature dependent elastic modulus E_1 calculated with Equation 5.3:

$$B_1 = E_1 I_1 \rightarrow E_1 = B_1/I_1, \tag{5.3}$$

with $I_1 = \frac{w_S \cdot h_S^3}{12}$ the area moment of inertia, with a width w_S of 6.35 mm and a measured thickness h_S of 0.22 mm. The resulting bending stiffness as a function of temperature as well as the calculated elastic modulus as input for the model are depicted in Figure 5.2. bending stiffness reduces potentially with increasing temperature, with a roughly halved bending stiffness for every temperature increase of 20 °C. At 100 °C bending stiffness is reduced by 96 % compared to room temperature values.
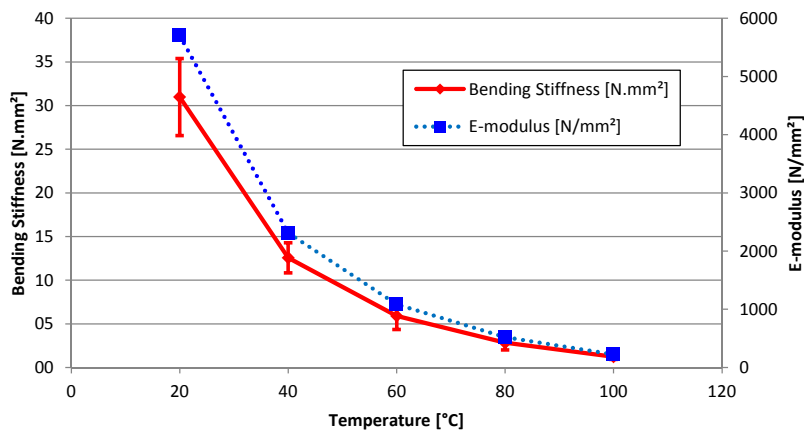
Figure 5.2. Slit-tape bending stiffness as a function of temperature of material 2

The influence of the model to bending perpendicular to fibre direction is neglected, as there is no bending on the placement of a straight path with single curvature.

5.2.2. Mechanical placement model

With the available model of the compaction roller, as one of the most prominent and important influencing factors for the layup quality and the material model for the bending behaviour of the slit-tapes, an mechanical model for the placement process is designed within the commercial FEM Software Abaqus CAE.
The model describes the complete placement process, including each separate slit-tape, the tool, and the kinematic movement of the placement head. Figure 5.3 depicts the model of the placement head.

The model consists of:

- 3D compaction roller with material properties taken from Chapter 3.3

- Rigid place-holder for the actual placement head including all relevant kinematic points
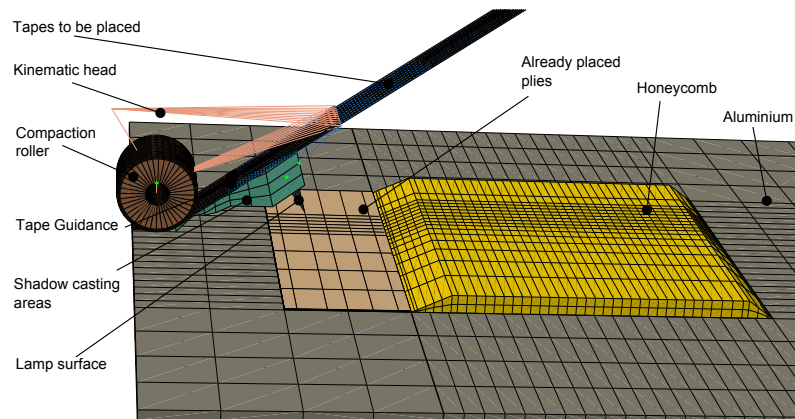
Figure 5.3. Overview of the mechanical model. Image not to scale.

- Individual slit-tapes with the length of the course

- Guiding channels for the slit-tapes

- Lamp surface and shadowing areas of the head for import in thermal analysis

- Arbitrary tool geometry, in current input from Section 4.4 of Chapter 4.

The model is fully parametrized to be easily adaptable to any AFP machine, and is accustomed to arbitrary tool geometries. The roller consists of 5040 C3D8 elements, the flat plate part of the tool of 812 C3D8 elements, the tapered honeycomb part of 1428 C3D8 elements. All elements for the slit-tapes consist of S4 shell elements, the guiding chanels for the tapes are rigid R3D4 shell elements and the wire head consists of 31 RB3D2 rigid beam elements. The model is solved implicitly including non-linear large deformations.
Boundary conditions of the actual model include:

- Kinematic movement of the rigid wire as placeholder for the actual placement head: five DoFs as direct input from the robot programming detailed in Chapter 4.4.3, with the exception of the translational DoF in the vertical axis of the robot

- Fixed bottom surface of the tool flat plate

- TCP in the vertical axis of the robot in the form of the compaction force

- Top edge of each individual slit-tape as the tape pretension

The boundary conditions of the placement path are input in the TCP of the rigid place-holder for the actual placement head. The kinematic movement of the head is input from the robot programming detailed in Chapter 4.4.3, for five DoFs, with the exception of the translational DoF in the vertical axis of the robot. Here, the defined compaction force is applied, with contact definitions between compaction roller, slit-tapes and tool surface. Further, standard penalty contact definitions are

applied to all contacting parts of the model with rough tangential contact behaviour, with exception of the tape guiding channels, which exhibit no friction behaviour.

5.2.3. Sequential coupling with thermal simulation

The mechanical model detailed in Section 5.2.2 is coupled with the thermal simulation from Chapter 4. The coupling procedure consists of:

1. Creation of the mechanical model

2. Input of the geometry to thermal simulation

3. Solving of the thermal simulation transiently with a defined time step t_i according to Chapter 4

4. Import of the temperature field to the mechanical simulation

5. Solving of the mechanical model implicitly transient with the time step t_i

6. Geometry update of the thermal model with input from mechanical results

7. Restarting the thermal simulation with previous temperature field and new geometry

8. Repetition from Step 2 until the placement is completed

The coupling procedure is further described in Figure 5.4.

After the simulation is complete, the full time-dependent temperature field can be compared with experimental values.

5.3. Thermo-mechanical coupled results of simulation validated with experiments

Thermal results including incremental geometric changes in the model are depicted in Figure 5.5, 8 s after movement start during the placement of ply 2. It is apparent that the maximum temperature is underneath the IR lamp, in front of the nip-point.

In the following, both surface and bulk temperature results will be compared to experiments that are described in Section 4.4.4.2 of Chapter 4.

Thermo-1:

1. Ini. temperature, $t << t_i$
2. Radiation, $t = t_0$

Temperature field

Mechanical-1:

1. Const. Temperature, $t = t_0$
2. Contact
3. Kinematic and Force BC, $t = t_i$

Geometry update

Thermo-i:

1. Radiation, $t = t_i$

$2 \leq i \leq n$

Temperature field

Geometry update

Mechanical-i:

1. Const. Temperature, $t << t_i$
2. Contact
3. Kinematic and Force BC, $t = t_i$
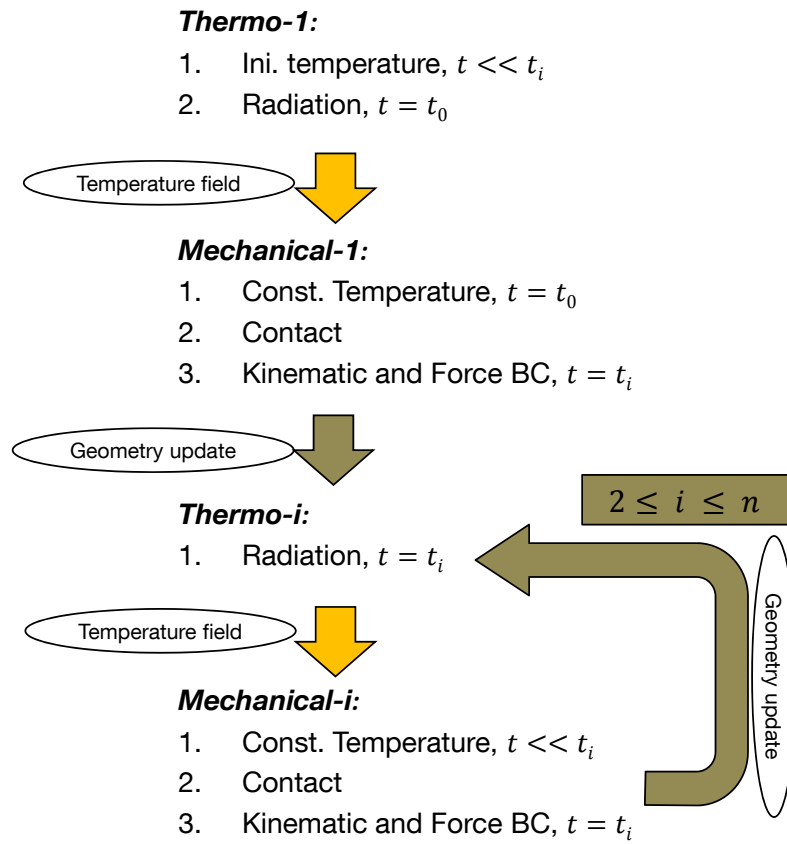
Figure 5.4. Sequential coupling procedure of the thermo-mechanical coupled model
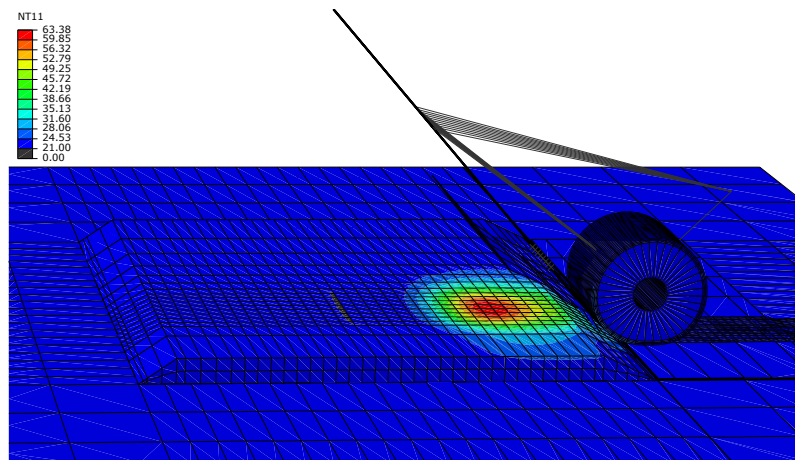
Figure 5.5. Simulation result during placement of ply 2, 8 s after movement start

5.3.1. Temperatures at the honeycomb interface compared with simulation results

Figure 5.6 shows the comparison between experimental and simulation result during the placement of all six plies on TC 14. The heat up and cool down phases are comparable, although there is a certain difference visible. Differences lie between $5\,°C$ during the placement of ply 1 and $2\,°C$ during the placement of ply 6. The prolonged cool-off phase after the sixth paths are completed is also captured accurately. Further shown are the six signals of the light barrier, as the head touches down.
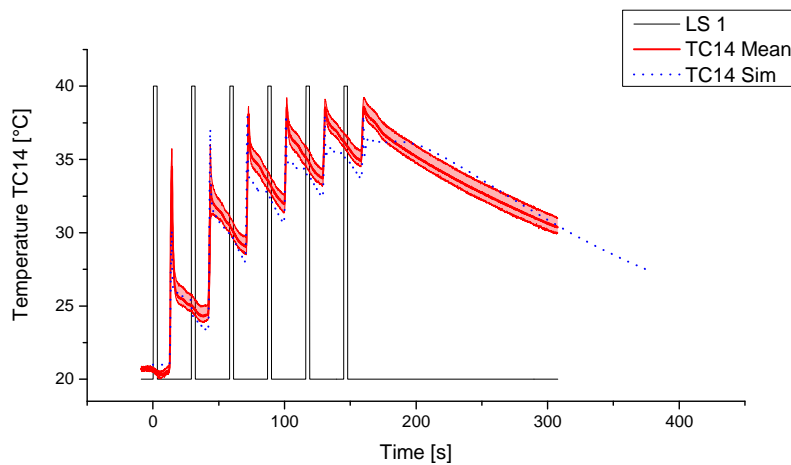
Figure 5.6. Temperature at TC 14: Comparison between Experiments and thermo-mechanically couples simulation results

The maximum temperatures of all TCs during all six paths are compared to simulation in Figure 5.7. The highly varying temperature distribution is captured accurately, with a maximum difference of $15\,°C$ during the second ply and a maximum difference of $-5\,°C$ during the last ply. It is presumed that the difference during second ply arises from insufficient contact of the first ply. Varying contact efficiency is neglected in the model.

The final temperatures of all TC for all plies are depicted in Figure 5.8 and compared to experimental values. It is apparent that for first ply the final temperatures agree very well with experimental values. As the number of plies rises, the temperature difference of the end temperature also rises, until there is a maximum difference of $-15\,°C$ for ply six.
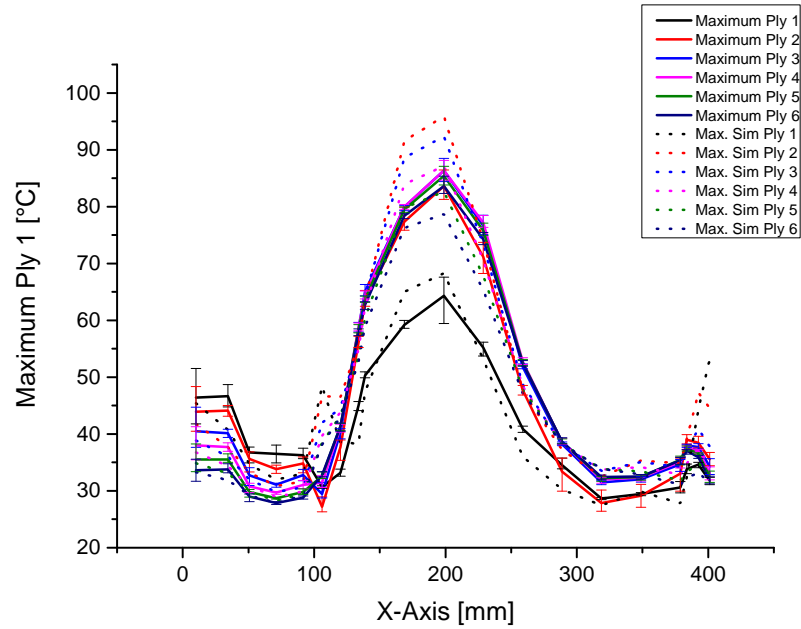
Figure 5.7. Maximum temperatures after the placement of each ply at every TC
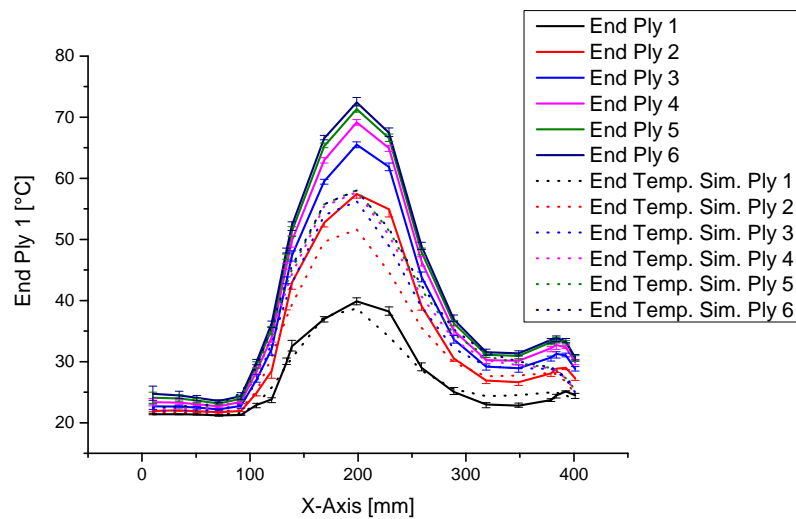
Figure 5.8. Final temperatures after the placement of each ply at every TC

5.3.2. Surface temperatures

Resulting surface temperatures were evaluated in the simulation model and compared to experimental values obtained in previous experiments. Figure 5.9 shows that both values are comparable, with highest differences during the placement of the first ply. During the experiments the surface temperature of all further plies is comparable, with the exception of ply 2, where insufficient contact leads to elevated temperatures. This effect is not captured in the model, therefore all simulation values reach similar temperatures, 30 °C higher than first ply.
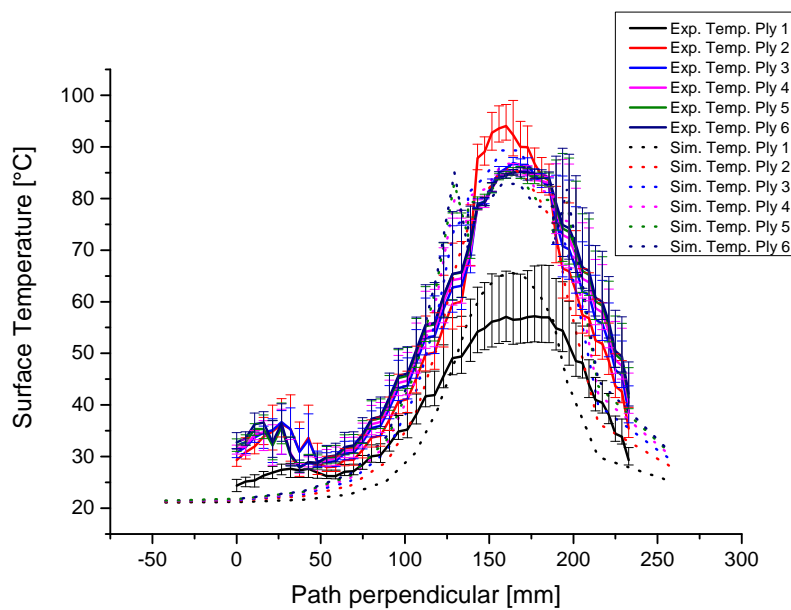
Figure 5.9. Surface temperatures perpendicular to placement direction, 8 s after movement start

The temperature gradients are over predicted, which leads to under predicted temperatures left and right of the path centre. This corresponds to simulation results of Chapter 4, and leads to the conclusion that in-plane conductivity values of honeycomb differs between simulation and experiments.

5.4. Discussion

With the sequential coupling of thermal and mechanical simulation, the continuous placement of the slit-tapes is modelled. This includes the cooling effect of the freshly placed slit-tapes as well as a continuous geometric update of the model. This opens up new possibilities to predict the AFP process. However, the modelling approach described above contains certain restrictions that will be discussed in the following.

5.4.1. Model possibilities and restrictions

With the sequential coupling it is possible to accurately predict temperature as well as the placement behaviour of the slit-tapes. The correct deformation and pressure distribution of the roller is predicted. Along with the known process temperature and process time, a model for pressure sensitive adhesives (PSAs) is developed in Chapter 6, so the adhesive behaviour of the slit-tapes depending on pressure magnitude, time of contact and process temperature may be included in the FEM model in future work.

However, the modelling approach holds some restrictions. The calculation time (6 CPUs) exceeds 48 hours for the six placement paths over the honeycomb structure. The model needs to increase in efficiency to be able to predict the placement of one complete ply or a full laminate. Further, with the sequential coupling, the temperature field influences the mechanical behaviour of the material, but not vice versa. A special exception in this study is the update of the geometry. However, this means that results of the mechanical simulation do not affect thermal results. Therefore a pressure dependent thermal contact is not possible to model. Therefore temperature and pressure dependent contact formation needs to be considered. The dependency is discussed in detail in Section 5.4.2.

With the high number of non-linearities including large deformation and non-linear contacts and the implicit numerical solver, convergence of the solution is an issue, and depends on the quality of the mesh as well as mesh discretisation.

5.4.2. Pressure and temperature dependent contact

Intimate contact in AFP is dependent on contact time, contact pressure and process temperatures as well as on the state of the prepregs in terms of surface topology. However, the contacts in the simulation model contain a fixed value that does not change with time, temperature or pressure.

Especially for high temperature gradients, as is the case during the placement on the honeycomb, this dependency is no longer safe to neglect, and needs to be included in future research. When the thermo-mechanical models are expanded to thermoplastic AFP, the formation of intimate contact is of major importance.

The next step to improve the simulation model is to incorporate pressure, time and temperature dependent contact. For this step, a fully coupled model is needed, because mechanical results are influencing the thermal properties as well as the thermal properties influence the mechanical results.

Further studies need to be undertaken to fully understand and characterize intimate contact dependent on AFP process conditions.

5.4.3. Cooling effect of continuous placement

When comparing simulation results of Chapter 4 and the coupled results above, it is apparent that the cooling effect of the freshly placed tapes may not be neglected for tools with low conductivities and specific heat. This corresponds with findings from Chapter 4 Thermal Measurements and Thermal Models for AFP. Especially for a tool material with low conductivities and high specific heat as Nomex honeycomb, these effects may not be neglected, and play an important role in process temperature.

6. Tack in Automated Fibre Placement - theory and application

The tackiness, i.e. the adhesive behaviour of the slit-tapes during deposition, is one key factor during layup. When the compaction roller presses the slit-tapes to the tool surface or the already deposited substrate, they have to completely stick to the surface to avoid layup defects. The slit-tapes tack develops a behaviour similar to a pressure-sensitive-adhesive (PSA)[27]. It strongly depends on the APF process variables compaction pressure, pressure dwell time (therefore layup velocity) and process temperature. Within this chapter, tack characteristics are discussed and a model for tack developed, that is able to predict tack for prepreg material and AFP boundary conditions.

6.1. Literature review for characterisation and modelling of tack

6.1.1. Tack characterisation

According to Zosel [111], tack is not a fundamental material property, but a phenomenon, that is conceived depending on its specific application. Different testing methods provide values to a specific end-use performance [112], and therefore are difficult to use as meaningful input for a physical understanding of tack.
Below, varying methods to determine tack are described including their advantages and disadvantages.

6.1.1.1. Thumb test

One of the earliest test for tack was the thumb test. A skilled worker applies a thumb with a certain pressure on the material to be tested, and removes it, therefore experiencing the stickiness of the material [113, 114] (Figure 6.1).

With time and repetitions, the worker gains an "experienced thumb", so being able to determine the amount of tack. This test is subjective and non-repeatable, depending on the individual worker, and therefore is not suitable for a robust objective method to determine tackiness.

Figure 6.1. Figure of finger print on tacky surface, from Crossley et al. [115]

6.1.1.2. Rolling ball test

The rolling ball test [113, 116] measures tack by placing a steel ball on an inclined surface, with the adhesive material at the bottom of the ramp (Figure 6.2).
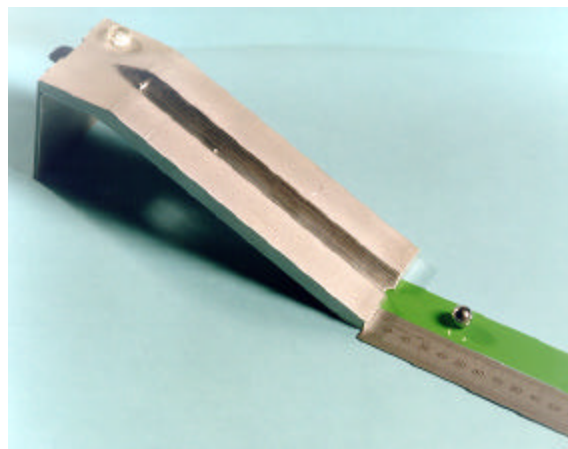
Figure 6.2. Rolling Ball Tack Test, from Duncan et al. [116]

The roller is released at a defined hight, and the distance the roller travels on the adhesive material is measured and used to quantify tack. There are some modifications to the test available, e.g. rolling cylinder or rotating drum [113].

The test is able to characterize tack, however, it does not take into account the surface structure or the wet-ability of the adhesive material. Further, any plastic or viscous behaviour of the material is neglected.

The test is suitable for rubber and tackifying resins [113]. Many functional adhesives do not have sufficient tack to stop the ball in the maximum prescribed length of tape, therefore no apparent roller tack can be measured.

6.1.1.3. Probe test

Probe tests are mechanical simulations of thumb tack tests [113]. A probe contacts the adhesive material with a certain force and dwell time, and is than removed at a defined speed. The maximum required force to remove the probe is defined as tack [113, 116].
A number of failure modes are observed occurring either in the bulk, possibly by fibrillation, or at the surface by crack formation and propagation [44, 117, 118] . Figure 6.3 depicts the test setup for the probe test.
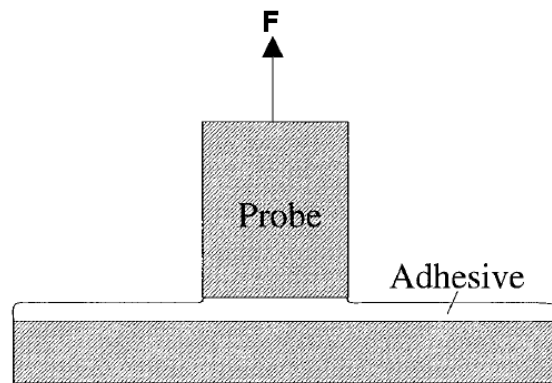
Figure 6.3. Probe Tack Test Setup, compare Lin et al. [117]

After Crossley et al. [44], the probe test is considered to be less suitable for the characterisation of ATL prepreg tack due to:

- Increased sensitivity to surface structure as well as entrapped air.

- Bulk failure may happen in the probe test, but is likely to be avoided due to the continuous fibres during AFP and ATL.

- There is no known method to convert the results to peel mechanisms.

6.1.1.4. Peel tests

Peel tests are most commonly used in the PSA industry [113]. Different modifications, e.g. the Loop Tack Tests [116], a 90° or 180° peel test according to *FINAT* Standard [119] or the most common test: the floating roller method [113, 120].

6.1.1.5. Peel tack test for AFP process parameters

To characterize tack that is closely related to tack experienced in ATL, the peel tack test was developed by Crossley et al. [115, 121]. The test setup was further developed to AFP processing environments by Stelzl et al. [122].

Figure 6.4 depicts the general principle of the test rig. The setup is designed to adopt comparable process conditions to a real AFP process.
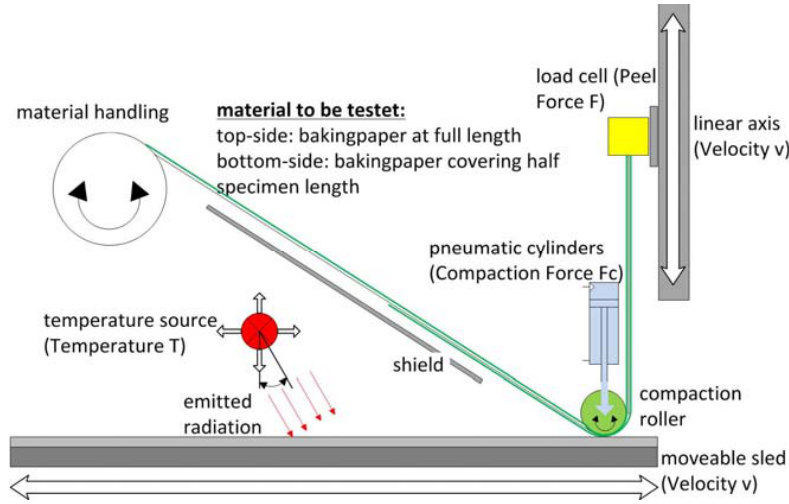
Figure 6.4. Principle of the Peel Tack Test Rig, Stelzl et al. [122]

The material is fed from a spool, and compacted to the surface by a deformable compaction roller with a defined force. A IR lamp heats the surface in front of the nip point of the material feed. A linear axis pulls the material upwards with a predefined speed, and measures the required force.

The fed material is separated into two parts:

- First part: The material is covered with a thin layer of PTFE, therefore omitting tack.

- Second part: The material is not covered any more, enabling tack

This leads to a separated curve of the measured force (Figure 6.5). The first part of the measured curve result from frictional losses and the bending stiffness of the tape, the second part of the curve has additional value due to the tackiness of the tape. When the mean forces of both parts are subtracted, the peel force due to tack can be extracted.

The unique characteristic of the test is that it represents AFP conditions very well. Velocity, compression force as well as heat input are comparable. The main difference to the real AFP process is that the substrate is peeled off after the compaction pressure is applied, opposed to real AFP when the peel is supposed to stay in place. Therefore, the tack test bench is able to test for short term tack development. However, long term tack cannot be covered.

The tackiness is measured in the form of a $90°$ peel force. The short-term character of the AFP process is adopted, while most other peel tests are suitable for long term compression forces. Further, the test can be applied to variable substrate materials
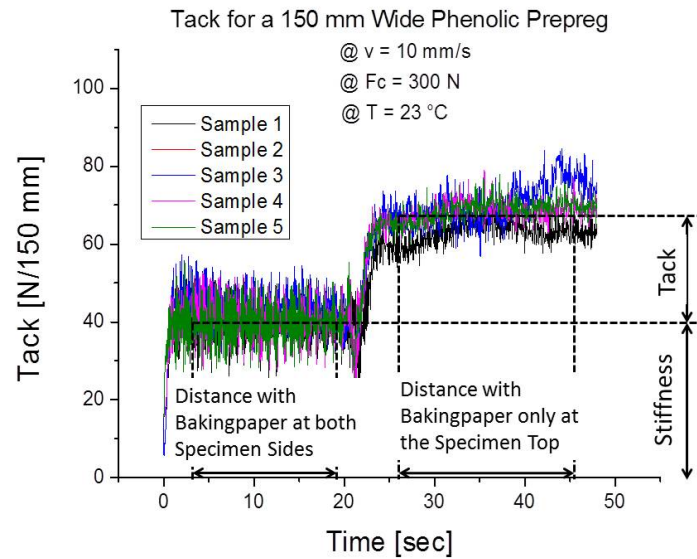
Figure 6.5. Exemplary data from measurement of the peel tack setup [122]

easily, therefore enabling the possibility to study first ply behaviour on varying materials.

6.1.2. Models for intimate contact

The definition of peel tack with both cohesive and adhesive failure strongly depends on the true contact area $A_C = \frac{A}{A_0}$. For many years scientist developed contact theories starting with the fundamental work of Hertz in 1882 [67]. Greenwood and Williamson [123] further develop the model towards a realistic microscopic contact behaviour. They describe a rough surface with a Gaussian heights distribution of spherical asperities with the same radius R. Although this contact model has been expanded for viscoelastic materials, e.g. Hui et al. [124], it is valid for true contact areas $A_C \ll 1$ where the contact area depends linearly on the load. Later Greenwood and Wu [125] revised their model, stating that peaks on a surface profile do not correspond to asperities. Instead a fractal approach should be used.

Levy et al. [92] uses a modified Lee and Springer model to determine the link between intimate contact and consequent thermal contact resistance during the thermoplastic automated fibre placement.

Persson et al. [126–131] presents a surface model with a self affine fractal structure using the surface roughness power spectrum. They present the model to be valid for a high degree of intimate contact close to 1. Yang et al. [132] further developed Perssons's model to molecular dynamics interaction between a randomly rough rigid body and an elastic flat block.

6.1.3. Models for tackiness

Creton and Leibler [133] ask the for AFP so important question of "how does tack depend on time of contact land contact pressure?". They model tack of polymer melts on randomly rough rigid surfaces under short contact times and low pressures. They further include molecular entanglement in the form of a power law with the result that the critical contact time has strong molecular weight dependence. Kendall [134] presents that adhesion is dependent on the interfacial surface energy, the geometry and elastic constant of the adherent bodies. Tordjeman et al. [118] present a probe test that is capable of studying the degree of intimate contact as well as tack strength. They find that tack has a strong dependence on sample thickness, therefore pointing out that the release energy is a function of contact area. Ahn et al. [112] use a modified probe test to study prepreg tack. They find that the relaxed and unrelaxed modulus of the prepreg stack along with relaxation time and initial void content are the four material parameters that define prepreg tack. Derail et al. [135, 136] test and model the adhesive behaviour for both cohesive and interfacial peel. They found that for cohesive fracture viscoelastic properties in the terminal region of relaxation are dominating. Interfacial peel splits into the regions rubbery, stick-slip and glassy. Gay and Leibler [137] state that interply tack energies are intensified by air suction in probe testing. Gent and Hamed [138] study the dependency of peel angle on the peel force. They found that the theory of small bending is only valid when the moment arm of the applied peel force is much larger than the length of the high stress region in the bond. Kaelbe et al. [139–142] study rheology and rate dependency of peel adhesives. They found that both molecular bond formation as well as boundary stresses define cohesive and adhesive failure in peel. Lin et al. model a probe tack test in detail using FEM [117]. They distinguish between frictionless and frictional failure, concluding that edge effects from pure Mode I failure to a mixture between mode I and II failure. They transfer their findings to the model of a 180° peel test in [143]. They found that the peel rate is inversely proportional to the square root of the adhesive thickness and directly proportional to $F_P^{3/4}$. Zosel [111, 144] tests various polymers in a probe tack test. He concludes that tack is related to incomplete bond formation and cannot be described with a viscoelastic material behaviour. It is rather influenced by glass transition temperature and the entanglement network of the polymer.

Crossley et al. [27, 115] experimentally determine peel tack under ATL process conditions . They use a WLF shift function to show that for tack depending on process temperatures time-temperature-superposition (TTS) is possible. Lichtinger et al. [29] developed a theory to conclude to peel tack from the process variables compaction pressure, pressure dwell time and process temperature.

Models for tackiness of PSAs range from molecular level to macroscopic phenomena

like fibrillation. The picture that the literature above describes is that PSA tackiness is a phenomenon that needs to be studied on many levels, and it is difficult to find a general model for all physical, chemical and mechanical elements.

6.2. Analytical tack model in respect to AFP process parameters

Within this study, the focus is on the tack between slit-tapes and the tool surface, as "the first ply problem" is the area of high concern regarding tack. Further plies exhibit elevated tack due to the adhesive behaviour of both contact partners.

6.2.1. AFP specifics applied to Pressure Sensitive Adhesives

Tack of slit-tapes is highly dependent of the AFP process parameters:

- Compaction force: With deformability of the roller resulting in compaction pressure and contact length

- Layup velocity: With contact length of the deformed roller resulting in contact time

- Process temperature

To understand tack of the slit-tapes depending on AFP process parameters, the laws of pressure sensitive adhesives (PSA) have to be applied, and combined with the theory of intimate contact between rough surfaces. With this knowledge, an analytical process model can be derived, describing tack as the energy release rate G_{IC}, dependent on the process variables temperature, compaction pressure as well as contact time, i.e. layup velocity, derived from the $90°$ peel tack test described in Section 6.1.1.5.

PSAs exhibit a direct dependency of pressure magnitude and time of applied pressure. With viscous behaviour of the resin there is further a dependency of process temperature.

Furthermore tack is dependent on the manifold material conditions, such as:

- Humidity

- Shelf-Life of the resin

- Surface structure of the tool as well as the slit-tapes

As this study is focusing on AFP process parameters, the material conditions are assumed to be constant. Therefore, the analytical tack model must contain the

dependencies for contact time, pressure magnitude as well as process temperature. Experimental values from literature are used to validate the analytical model for intimate contact and tack.

6.2.2. Fracture mechanics for the 90° peel tack test

The energy balance for a $90°$ peel tack test as shown in Figure 6.6 sums up the stored elastic energy in the peel substrate dW^e, the plastic energy dissipated during peel dW^v and the energy release rate G_{IC} of the fracture, compare Kinloch [145]:

$$(1 - cos\varphi) F_P dx = dW^e + dW^v + G_{IC} W dx. \tag{6.1}$$
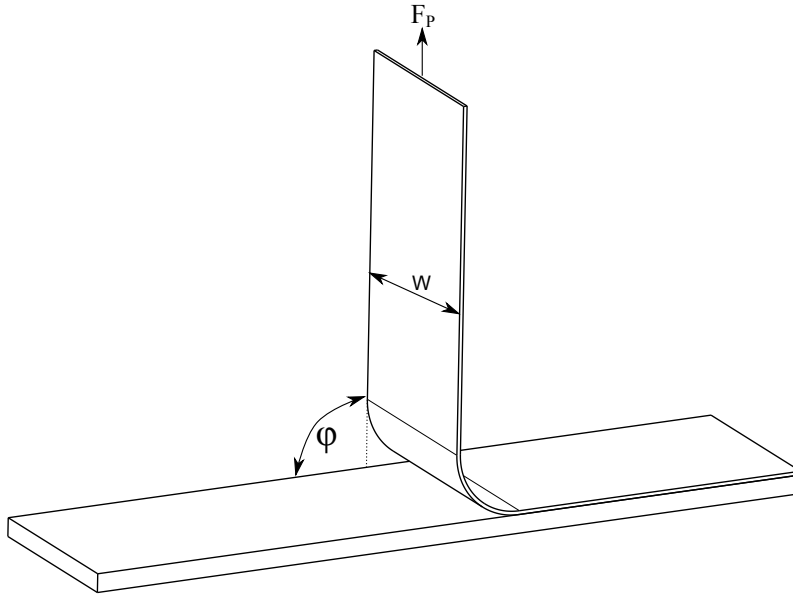
Figure 6.6. Sketch of the peel tack test with process variables

However, for the peeling of slit-tapes the elastic term can be neglected as the stiffness of the fibres is far greater than the adhesive forces. Further the plastic term can be neglected as the fibres take on elastic material behaviour in fibre direction. With a peel angle $\varphi = 90°$, this leaves the term:

$$\frac{F_P}{W} = G_{IC}; \tag{6.2}$$

with F_P being the force required to peel the specimen off the substrate, and W the width of the tape. Therefore, the quantity tack can be directly measured by the peel force F_P, and with the width of the tape expressed with the energy release rate G_{IC}. Failure can be roughly distinguished between

- adhesive (Interfacial) and

- cohesive (Strength)

failure (compare Figure 6.7). Adhesive fracture appears due to mechanical, chemical failure mechanisms as well as contact efficiency [113].
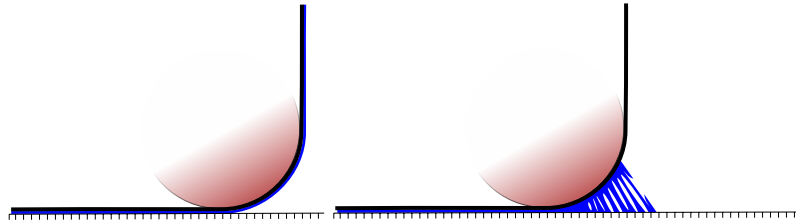
Figure 6.7. Adhesive (left) and cohesive (right) failure mechanisms during peel, compare Lichtinger et al. [29]

Cohesive failure happens due to the weakened internal strength of the viscoelastic resin, as well as to contact efficiency to a small part.

Models for peel must distinguish between both failure mechanisms.

Tordjeman [118] confirms experimentally what Raphael [146] suggested theoretically: A direct correlation between the adhesive energy release rate $G_{IC_{adh}}$ and the true contact area A_C:

$$G_{IC_{adh}} \sim (A_C)^2 , \tag{6.3}$$

with a_m being a coefficient dependent on the maximum possible energy release, the equation for $G_{IC_{adh}}$ becomes:

$$G_{IC_{adh}} = a_m \cdot (A_C)^2 . \tag{6.4}$$

Therefore, the energy release rate in adhesive failure depends heavily on the true contact area.

The cohesive fracture of a peeled tape is based on a weakened internal strength of the resin [121]. According to [113] in the case of cohesive failure there exists a direct linear relationship between bond strength of adhesive films.

In dynamometric tests the strength of the adhesive is expressed by force P or stress at the moment of failure which, in turn, depends on temperature and deformation rate.

Following relationship between cohesive strength and the process relevant parameters feed rate and temperature exists [113]:

$$\sigma_C = k_\sigma \cdot v^m \cdot e^{\frac{k_T}{T}} \tag{6.5}$$

Where k_σ and m are parameters depending on the properties of bond elements and test conditions and k_T are parameters depending in the mechanical deformation properties of the elements of the bond.

Furthermore [113] states under the assumption that shear stresses are negligible and the materials are hookean solids that

$$G_{IC_{coh}} \sim \sigma_C \tag{6.6}$$

With the width of the tape w and substrate thickness being constant, and σ_c the tensile strength of the adhesive.

Where k_σ , k_T and m are coefficient to be determined empirically. It is assumed that the internal strength is further depending on intimate contact A_C, as bond strength can only develop where true contact developed, although the influence of $\frac{A}{A_0}$ may be small because in a cohesive fracture zone $A_C \Rightarrow 1$. This is included in Equation 6.5:

$$G_{IC_{coh}} = A_C \cdot k_\sigma \cdot v^m \cdot e^{\frac{k_T}{T}}. \tag{6.7}$$

There a direct correlation between peel force and the process parameters peel rate, compaction force and process temperature was found with only few material and bonding parameters needed to be determined.

However, above model for cohesive failure depends heavily on parameters that must be determined by testing and then fitted to suit the equation. This fact is discussed in Section 6.4 of this chapter.

6.2.3. Intimate contact

Persson [131] recently developed a new contact mechanics theory which also includes large pressures with $\frac{A}{A_0} = A_C$ ratios close to 1. He states that the real contact area is based on the magnification level one looks at the surface roughness. In [132] Yang further develops Persson's theory to

$$A_C = \frac{A}{A_0} = \frac{1}{\sqrt{\pi G}} \int_0^p d\sigma e^{\frac{-\sigma^2}{4G}} = erf\left(\frac{p}{2\sqrt{G}}\right) \tag{6.8}$$

with p the pressure and

$$G = \frac{\pi}{4}\left(\frac{E(t)}{(1-\nu^2)}\right)^2 \int_{q_L}^{\xi q_L} dq q^3 C(q) \tag{6.9}$$

For this purpose the surface power spectrum $\int_{q_L}^{\xi q_L} dq q^3 C(q)$ was simplified as a constant coefficient c and the stiffness as $E^* = \frac{E_{resin}}{1-\nu_{resin}^2}$ therefore becoming:

$$G = \frac{\pi}{4} (E^*)^2 \cdot c, \tag{6.10}$$

dependent only of material parameters and the introduced coefficient c, therefore resulting in the true contact area:

$$A_C = erf\left(\frac{p}{\sqrt{\pi c} \cdot E^*}\right) \tag{6.11}$$

It is worth noting that [132] for small nominal pressures $p << G^{\frac{1}{2}}$:

$$A_C \approx \frac{p}{\sqrt{\pi G}} \tag{6.12}$$

which resembles the basic law of coloumb friction.

Hui et al. [124] use a maxwell material model to describe the relaxation function, where E_0 is the instantaneous modulus and η is the viscosity in addition to the time t.

$$E^* = E_0^* \cdot e^{-E_0^* \cdot \frac{t}{\eta}} \tag{6.13}$$

With the help of the basics of Time-Temperature-Superposition (TTS) and the William Landel Ferry Equations (WLF), a temperature dependence for the viscosity can be derived.

$$\eta_T = \eta_{T0} \cdot 10^{\left(-\frac{C_1(T-T_0)}{C_2+(T-T_0)}\right)} \tag{6.14}$$

Crossley et al. [27] use the WLF shift function successfully on their tack measurements. With this Equation 6.11 can be expanded to

$$\frac{A}{A_0} = erf\left(\frac{p \cdot e^{E_0^* \cdot \frac{t}{\eta_T}}}{\sqrt{\pi c} \cdot E_0^*}\right), \tag{6.15}$$

resulting in a true contact area only depending on the material properties, surface pair parameter as well as the contact pressure, contact time and temperature-dependent viscosity of the resin. For the sake of completeness it is added that the contact time is inversely proportional to the peel-rate.

With above Equations, a model was found that can relate peel tack to processing conditions of the AFP process, primarily:

- Contact pressure,

- layup velocity and

- process temperature.

6.3. Validation of the tack model

6.3.1. Method of validation

The original intention of this research was to validate the tack models for adhesive and cohesive failure at the peel tack test rig developed by Stelzl et al. [122] at the Institute for Carbon Composites. This test incorporates all AFP specific process parameters and tests the placed substrate for tackiness.
However, due to problems with control in temperature and peel rate, the test rig in its current form cannot be used for validation. Therefore, literature data by Crossley et al. [27, 44, 121] was used for validation of the models, along with following restrictions:

- Unknown surface roughness of rigid plate and peel specimen

- Rigid steel compaction roller

- Unknown thickness of tapes resulting in unknown pressure distribution of the roller

- Different peel rate, as literature data originates from ATL with reduced peel rate (maximum of 500 mm/min compared to AFP of 1000 mm/s)

- Different temperature range

- Glass prepreg instead of carbon

- Varying resin system

All unknown parameters had to be assumed or fitted to experimental data.
Failure of the initial test setup and how to improve the control of the test rig is discussed in detail in Section 6.4 of this Chapter.

6.3.2. Results of the tack model compared to literature

With the experimental values from literature, Equation 6.16 contains five values that have to be fitted.

$$G_{C_{adh}} = a \cdot \left(erf \left(\frac{p \cdot e^{E_0^* \cdot \frac{t}{\eta_T}}}{\sqrt{\pi c} \cdot E_0^*} \right) \right)^2 \tag{6.16}$$

Some of the parameters can be combined, therefore simplifying the curve fit. $\kappa_{pc} = \frac{p}{\sqrt{\pi c} \cdot E_0^*}$ and $e^{E_0^* \cdot \frac{t}{\eta_T}} = e^{\kappa_\eta / v}$ with v the peel rate, following Equation with three variables derives:

$$G_{C_{adh}} = a \cdot \left(erf \left(\kappa_{pc} \cdot e^{\kappa_\eta / v} \right) \right)^2 . \tag{6.17}$$

in cohesive failure the Equation 6.7 can be simplified by combining $\kappa_\sigma \cdot e^{\frac{k_T}{T}} = \kappa_{\sigma T}$, reducing variables to two parameters:

$$G_{C_{coh}} = A_C \cdot \kappa_{\sigma T} \cdot v^m . \tag{6.18}$$

The result is shown in Figure 6.8 for a sweep of peel rate, compared to experimental values from Crossley et al. [44]. The fitted variables are summed in Table 6.1. For the sake of simplicity units were omitted.

Table 6.1. Fitted values for the peel tack test with peel rate variance

a	40
κ_{pc}	0.2
κ_η	0.34
$\kappa_{\sigma T}$	90
m	0.95

The transition from cohesive at slow peel rates to adhesive failure at high peel rates can be clearly distinguished. The slower the peel rate, the more time for intimate contact to develop, strengthening the interfacial bond. There fibrillation occurs (compare also Crossley et al. [44]), and failure happens due to weakened internal strength of the resin. The influence of the degree of intimate contact is clearly seen in the transition between cohesive and adhesive failure, dominating the interfacial failure.

Figure 6.9 depicts results from temperature sweeps with multiple compaction forces, with experimental values from [27].
Equation 6.16 are be fitted with additional η_T as the WLF equation with $C_1 = 10.0$, $C_2 = 100.0$ and $T_0 = 10.0\,°C$.

Again, the transition between adhesive failure for low temperatures to cohesive failure at high temperatures can be clearly seen. The compaction force has influence on tack, however the process temperature is dominating. The model has good agree-
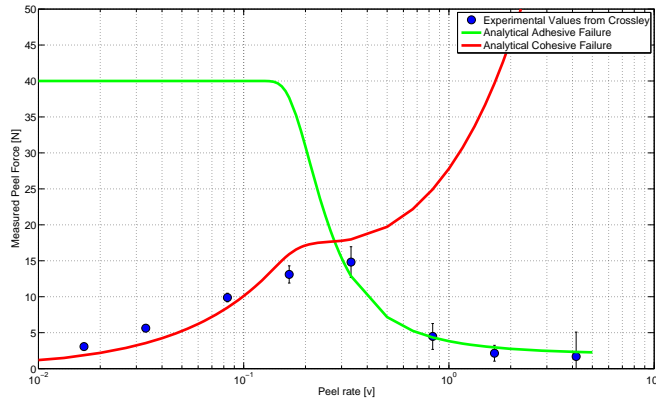
Figure 6.8. Results of the parameter fit for peel tack depending on peel rate; Experimental values from Crossley et al. [44]
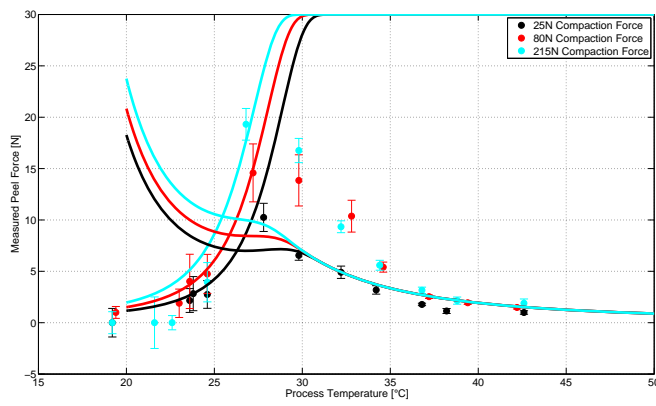
Figure 6.9. Peel Forces over Temperature for varying compaction pressures, experimental values from Crossley et al. [27]

ment with experimental values in the adhesive zone, however in the cohesive zone at higher temperature the fitted parameters do not fully agree. It is presumed that the curve fit for intimate contact does not fully agree with reality, as the model for cohesive failure has no other dependency on compaction pressure.

6.4. Discussion

Adhesive behaviour is a phenomenon hard to understand and difficult to describe. Within this work a model for the adhesive behaviour of thermoset slit-tapes was derived. The planned tack tests with a peel tack test rig failed therefore literature data was used to validate the model.

6.4.1. Validity of the model

The model uses the process parameters that are known to influence tackiness. To fully predict tackiness, all these parameters need to be measured and evaluated. These parameters are:

- Surface roughness of both contact partners (Tape and Substrate)

- Temperature dependent viscosity profile of the resin system

- Maximum possible energy release rate for perfect contact and adhesive failure

- Pressure distribution of the compaction roller

- Temperature dependent viscoelastic material parameters of the resin

The model does not include chemical bonding, e.g. molecule entanglement or van-der-waals forces, which might also influence tackiness of thermoset resin systems. Cohesive failure is a power law based on empiric data [113]. To further understand cohesive tacky failure, the behaviour of the uncured resin needs to be understood, and its influence on contact mechanics.

6.4.2. Implications of the model

At cohesive failure it is presumed that full intimate contact is established. this correlates to standard AFP process windows, as the tack rarely reaches a cohesive level during placement of the first ply.
Highest tack may be reached with the transition between cohesive and adhesive failure, therefore the goal of the design engineer should be to reach that process window.
The model indicate again the complex interaction between the AFP process parameters temperature, pressure and layup rate.

7. Conclusions and future applications

The goal of the research presented in this thesis is to deepen the understanding of the thermoset AFP process, and work towards a process model that combines the process variables relevant for AFP.

This required the study of detailed thermodynamic and mechanical phenomena starting from the analysis of basic AFP flat layup leading up to the placement on complex geometry of a tapered honeycomb chamfer. Process simulation proves to be a valuable tool alongside experimental work for insight into physical phenomena. With acquired knowledge it is possible to use the process models to predict the phenomena relevant for the AFP process up to a point. In the following the conducted research in the different physical disciplines is reflected and possible future applications are discussed. Based on the literature review of the individual chapters, the main results of the thesis are condensed below:

- Understand and predict the highly time dependent temperature balance during the thermoset AFP process.

- Research on contact behaviour of AFP compaction rollers and their application on complex shaped geometry.

- Combine the thermodynamic and mechanical process variables for the placement on a tapered honeycomb structure.

- Analyse and predict tack of the deposition material.

7.1. Conclusions

Within Chapter 3: "Mechanical aspects of AFP" the manufacture of tapered honeycomb structures using the AFP process was investigated, and the kinematic effects for the placement on discrete complex structures are discussed. An analytical relationship between gap and steering effects in relation to ramp angle and path angle was found and compared with experimental placement tests. It was found that resulting gaps may be reduced, but it is not possible to prevent them completely on a discrete structure such as a tapered honeycomb. Further, with the reduction of gaps additional effects such as unnecessary complex movements of the placement robot accompanied with placement defects may be generated.

To understand bridging effects on concave surfaces, the deformability as well as the

pressure distribution of an industrial compaction roller was studied, and a simulation model derived. Resulting deformability as well as pressure distributions agree very good in a practical range, and results conclude that deformability of the roller plays a major role in considerations for the placement on concave surfaces.

The resulting pressure magnitude and contact time of the testing of the compaction roller are used as input variables for through-thickness compression response experiments of slit-tape stacks. Results show that compression deformation of the slit-tapes is highly dependent on the process variables pressure magnitude, layup rate and process temperature. Stack thickness changes up to 40 %. Further, there is a dependency on fibre angle sequence of the stack, indicating nesting effects. It is concluded that these thickness changes influence further process variables such as temperature distribution as well as the final laminate quality.

In Chapter 4: "Thermal simulation of AFP" the need for thermal management and temperature predictions during the AFP process are outlined. A multi-angle flat plate component was laid up and both bulk and surface temperatures measured. The results show a temperature gradient perpendicular to the placement paths, as well as in path direction. This must be taken into account during the design phase of the path planning, as the process temperature affects all further process parameters as well as the layup quality. 1D, 2D and 3D models are compared to experimental values with the result that dimensional reduction is ineligible with an IR heat source. Further, the placement on a multi-material complex geometry, in this case the placement on a tapered honeycomb on an aluminium plate, shows the need for thermal control during AFP. Here, thermal experiments were conducted and compared to simulation. The results show a highly irregular temperature distribution, that arise from the differing tool material properties, as well as the complex kinematic movement of the placement head. The pure thermodynamic simulation is able to capture the temperature increase during layup, however it becomes apparent that it is not sufficient to capture the cool-off phase correctly.

Therefore, in Chapter 5: "Thermo-mechanical coupled AFP process model" a sequentially coupled process model is derived that combines the mechanical model of Chapter 3 and the 3D thermal FEM model of Chapter 4. This captures the continuous placement of the tapes, along with the pressure distribution of the roller as well as the layup rate. The bending behaviour of a slit-tape is experimentally analysed with the result that the bending stiffness reduces up to 96 % at a process temperature of 100 °C. These results are transferred to the thermo-mechanically coupled FEM model. It is found that the cooling effect of the tapes to be placed may not be neglected, and that they play an important role during the placement on the honeycomb. However, the model still needs improvement, as temperature or pressure dependent contact properties are omitted. This also implies that the sequentially coupling is not fully sufficient, and a full coupled model is necessary. Nevertheless,

the results show the definite need for process control and process prediction during placement on multi-material tools such as the combination of honeycomb and aluminium or with complex movement of the placement head.

In Chapter "Tack in the AFP process" an analytical model tailored to the AFP process including its specific boundary conditions is developed. Process variables include compaction pressure, contact time - therefore layup rate - and process temperature. Literature data is used to validate the model, with mentioned restrictions. The model provides insight in AFP tackiness, and states that intimate contact is one mayor factor that influences tack. With aviation grade toughened prepreg systems, that have a highly irregular surface structure, this needs to be taken into account. Low tack levels may be counteracted by adjusting the process window towards a higher temperature or compaction pressure or lower layup rate. However, more research is necessary to fully validate the model, and gain further insight into different phenomena that band together into tackiness.

7.2. Application possibilities and outlook for future work

The developed models are sufficiently accurate to propose the consideration of roller deformability and pressure magnitude during the design phase. With known deformability, it may be possible to exclude defects such as bridging early in the product development chain, therefore reducing the risk of additional cost. Additionally, it is possible to reduce the risk of core crushing during manufacture by considering maximum pressures.

Future research needs for mechanical phenomena in AFP are the combination of the resulting compaction pressure, compaction time and transient temperature in a through-thickness model that includes the compaction-release cycle of a typical AFP process. A through thickness deformation model for the slit-tapes may provide valuable insight into laminate compaction, consolidation and final laminate thickness after a certain number of plies. In Section 3.3.5.1 the design of a roller as compaction device was discussed. A further research possibility may be the design of a new compaction device that incorporates the necessary deformability along with a constant pressure distribution that is needed for the placement on multiple curved surfaces such as a tapered honeycomb sandwiches. Further, the compaction device may incorporate further features such as active heating or cooling, therefore influencing the process.

Thermal prediction of the process may be applied to the virtual optimisation towards maximum material throughput with sufficient temperature, and therefore

sufficient tack. This may reduce testing iterations, and therefore reduce initial cost of a product.

Above mentioned temperature and pressure results in the thermo-mechanically coupled simulation may be used in future research as input parameters for the tack model. On the other way round the model for intimate contact may be included in thermal contact resistance depending on temperature, pressure and time. With the known parameters, the model needs to be validated including AFP specific boundary conditions as well as aerospace grade material. The knowledge of tack characteristics may be applied to material screening for AFP manufacture for a quantitative assessment of the adhesive behaviour.

It is proposed that temperature consideration should be integrated early in the design stage, including the control of the heat output as part of the offline simulation. This reduces the risk of excess temperature, infeasible temperature gradients during manufacture and subsequent artificial ageing.

The design aspect must not be neglected. The path planning needs to take process temperature into account. More research is needed for path planning algorithms, therefore reducing irregular temperature distribution in tool and layup. This may lead to new layup strategies such as chaotic layup or a discrete distribution of paths. Further control variables may not just be the magnitude of the heat output, but also location and angle of the IR lamp through the mean of actuators. The "first ply problem" may be optimised by an increase in the emissivity of the tool through black varnish or soot, therefore increasing possible layup velocities during first ply layup. This study shows that temperature and pressure dependent thermal contacts need to be taken into account. This implies that a fully coupled model is needed, especially when considering these models for thermoplastic AFP, where the control of temperature has high impact in in situ quality.

When the application is in need of tight thermal limits during the process it is imperative to include thermal feedback control. Some if the thermal models described in this work are able to calculate the transient history in real time. Therefore it would be possible to include these models in a closed loop feedback control.

Future research may also rethink the requirements for a heat source in thermoset AFP. This study implies that a IR lamp is not optimal due to its diffuse characteristics. IR LED heating or a low level laser heating may be considered as future heat sources for thermoset AFP.

A. Improvement for the tack test bench

A.1. Reasons for failure of peel tack test

The peel tack test rig developed by Stelzl et al. [122] is in theory an excellent setup for testing the tack at AFP process conditions. Tests were conducted using Hexply 8552 UD prepreg system with a width of 150 mm. The prepreg was coiled around a paperboard drum, with backing paper between each layer. The setup is able to vary the process conditions velocity and compaction force, as well as temperature in the form of a IR lamp at a certain angle and distance.

The test setup works well with high tack resin systems like phenolic resins under room temperature and above. However, aerospace grade toughened prepreg systems have very little tack. With this, various problems arise which will be discussed in the following. Further, control of the process variables and the noise of the measured peel force were also influencing the tests, with the final conclusion that the peel tack test rig in its current form cannot be used to validate the tack model.

A.1.1. Signal noise

The measured peel force is depicted in Figure A.1. Random noise is dominating the measured signal. Nevertheless, there is a distinct difference between the two parts of the tape with and without adhesive behaviour, therefore it was possible to measure tack forces.
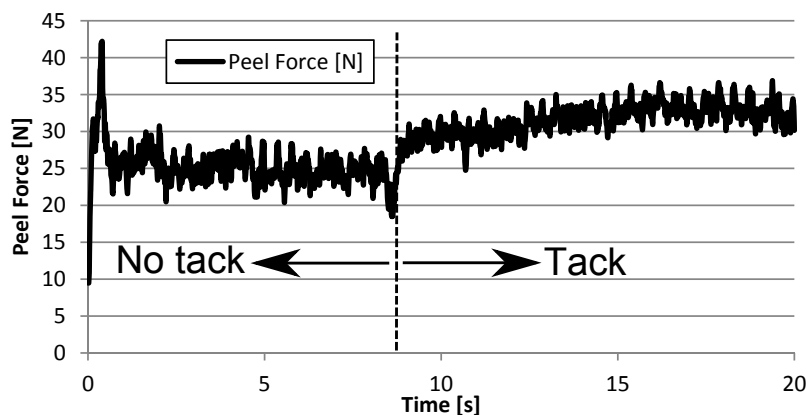
Figure A.1. Measured peel force signal at 25 mm/s peel rate, 3.2 N/mm compaction force and 3 W/mm heat output of the heat source

However, with the signal noise the variance of the test results are very high. Figure A.2 depicts test results of tack at a peel rate of 25 mm/s over a range of temperature and compaction force. Three repetitions were made, and the standard variance is displayed.

A dependency of compaction pressure is not possible to deduct. Further, the temperature dependency stays within error limits of each neighbouring test.
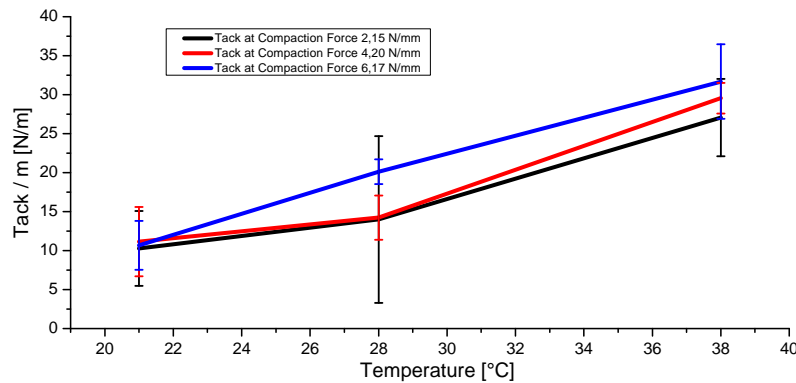
Figure A.2. Measured Tack over temperature, with standard variance after three measurements

It is necessary to reduce the signal noise to be able to measure tackiness of aerospace grade toughened prepregs.

A.1.2. Control of peel rate

The velocity control of the linear axis for a peel rate of 25 mm/s was adequate. However, when peel rate was changed to 100 mm/s, the torque controlled motor was not able to maintain a constant velocity. This results in a high variance of peel force, as depicted in Figure A.3.
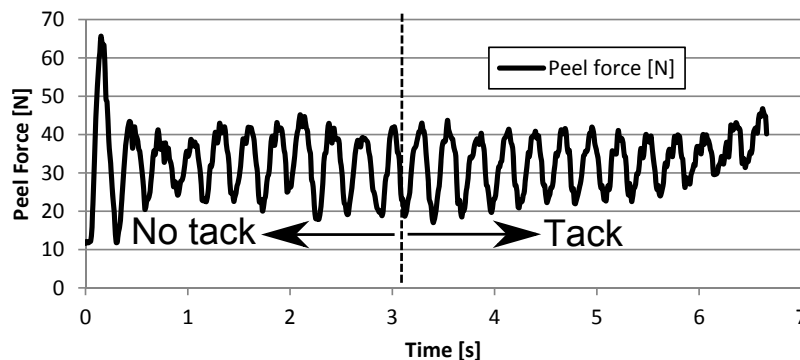
Figure A.3. Measured peel force at higher velocities

A sinusoidal oscillation of the peel velocity results in a high oscillation of measured peel force. Further, it is not possible to distinguish between non-adhesive and adhe-

sive parts of the test signal.

The preliminary assumption that the stiffness of the test setup is not sufficient was eliminated by applying a direct load to the force measuring cell in the form of a defined mass. Direct read out of motor current coincident with the oscillation, therefore resulting in the statement that the motor controller is not able to set a fixed velocity with varying motor torque.

A.1.3. Influence of backing paper

The spool of 75 mm wide UD prepreg is separated by a stiff backing paper coated with release agent. Nevertheless, the backing paper is bonded to the UD prepreg to a certain degree, therefore increasing the force required to pull the prepreg off the spool. When the linear axis moves upwards, the spool rotates. As the prepreg sticks to the backing paper underneath, the peel angle of the spool changes while the spool is rotating, from the original tangent (Figure A.4) to a normal direction. It is not
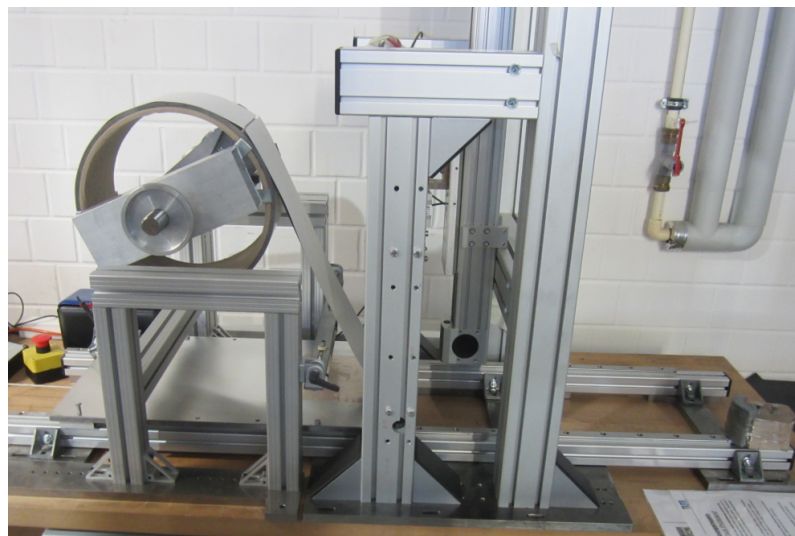
Figure A.4. Backing paper of the test roll between each layer

possible to set the peel angle normal from the spool as the tack from the prepreg to the backing paper is highly inconsistent and will cause additional variations in measured peel force.

A.1.4. Influence of tape width and width of compaction roller

To have full control of the test, the compaction roller needs to be the same width as the tested prepreg. Otherwise the applied compaction force would also be applied on the tool next to the tape, therefore making it impossible to determine how much force actually arrives at the prepreg.

When the compaction roller has the same width as the prepreg, the rotation axis of the spool needs to be totally aligned with the axis of the compaction roller and the line of the clamp of the load cell. Otherwise the prepreg will not stay centred during the motion of the linear axis, and will travel partly to the left or right of the compaction roller, therefore reducing measured peel force.

A.2. Recommendation for improvement of the peel tack test

From the experiences made from the failed tack tests, some recommendations on how to improve the test are found below.

A.2.1. Temperature control

The process temperature is set by the means of an IR lamp with a maximum output of 2700 W. The IR lamp perfectly simulates the real thermoset AFP process. However, an IR lamp is not suitable for process testing of tack for process windows.

The surface temperature of the tool needs to be measured for every tool design and every tool material, as well for every peel velocity, to conclude to the process temperature. Further, additional process variables arise from lamp angle and lamp position. In addition, the incoming tape needs to be shielded adequately from direct and indirect radiation heat input.

Figure A.5. Temperature control

It is recommended to change the heat input from IR to a thermal chamber, so temperature can be controlled for the complete system. Further, the thermal chamber could also incorporate humidity control.

A.2.2. Peel rate control

Apparently the torque controlled motor is not able to achieve a constant velocity. Until the end of the tests it was not clear if the set PID control parameters are the reason for the failed control, or the amount of steps of the motor.

It was ensured that the stiffness of the test rig was not responsible for the measured oscillations. Further tests should be made with a different controller, or a Servomotor-Drive with higher resolution of steps.

A.2.3. Accessibility

Further recommendation for improvement is accessibility. The test rig's design aims for maximum stiffness. However, some profiles can be omitted without losing structural stiffness. This will greatly improve accessibility when changing the prepreg on the clamp of the load cell, or re-feeding the prepreg after each test is completed.

B. Supervised student theses

Date	Thesis type	Student	Title of the Thesis
03/2012	Semester	Tang, Jiannan	Entwicklung eines zeit- und druckabhängigen Versagens mit kohäsivem Kontakt im Bereich Automated Tape Laying
04/2012	Diploma	Hans, Thorsten	FE-Modellierung des Automated-Fiber-Placement-Prozesses mit Kopplung der thermischen und werkstoffmechanischen Aspekte und Validierung des Simulationsmodells anhand von Ablegeversuchen
05/2012	Master	Zhao, Xu	Mechanical FEM Simulation of the Automated Fiber Placement Process
09/2012	Diploma	Tang, Jiannan	Entwicklung eines Versagensmodells für den Peel-Tack-Test und dessen experimentelle Validierung
09/2012	Semester	Hagedorn, Lorenz	Untersuchung zur geometrischen Winkeländerung während der Faserablage
02/2013	Diploma	Lechner, Alexander	Erstellung eines FE-Modells zur thermischen Analyse des AFP-Prozesses und Validierung anhand von Ablegeversuchen
06/2013	Semester	Leyendecker, Matthias	Numerische Simulation des thermochemischen und mechanischen Verhaltens von Prepregs während des Automated Fiber Placment Prozesses mit Matlab auf Basis der Finite-Differenzen-Methode
06/2013	Bachelor	Sagraloff, Nadine	Implementierung des P1-Strahlungsmodells in Comsol Multiphysics
08/2013	Term Paper	Guilloux, Adrien	Investigation of the Deformation Behavior of a Compaction Roller for the Automated Fiber Placement Process
08/2013	Internship	Ghrib, Meriem	Investigation of Compaction Behavior of Prepregs during Automated Fiber Placement Process
10/2013	Semester	Jähne, Christoph	Entwicklung eines Softwaretools zur Optimierung und Validierung diskreter Ablagepfade für den AFP-Prozess mit MATLAB
10/2013	Intership	Muhr, Markus	Thermodynamische Finite-Differenzen-Simulation des Automated Fiber Placement-Prozesses in Matlab mit Ausblick auf die Proper Generalized Decomposition-Methode
12/2013	Semester	Heigenhauser, Benedikt	Parametrische thermische Simulation des Automated Fiber Placement Prozesses angewendet auf eine Honeycomb-Struktur mit Hilfe der Finiten Elemente Methode
03/2014	Semester	Schlegel, Katharina	Numerische Simulation des Prepregverhaltens während des Automated-Fiber-Placement-Prozesses auf einem getaperten Honeycomb
08/2014	Master	Heigenhauser, Benedikt	Entwicklung eines Modells zur numerischen Optimierung der Faserablage in einem FVW Bauteil unter Berücksichtigung von Fertigungsbedingungen
12/2014	Diploma	Vilas, Alexis	Development of a Finite Element Method model to study the emerging defects in chamfered sandwich structures during the Automated Fibre Placement process

Bibliography

[1] Manfred Neitzel, Peter Mitschang, and Ulf Breuer. *Handbuch Verbundwerkstoffe*. Carl Hanser Verlag GmbH & Co. KG, 2004. ISBN 978-3-446-43696-1.

[2] Klaus Drechlser and Roland Hinterhölzl. Lecture: Analysis and design of composite materials, 2014.

[3] Dirk Hans-Joachim Adrian Lukaszewicz, Carwyn Ward, and Kevin Potter. The engineering aspects of automated prepreg layup: History, present and future. *Composites Part B: Engineering*, 43(3):997–1009, 2012.

[4] Timothy Gutowski. *Advanced composites manufacturing*. John Wiley & Sons, 1997. ISBN 978-0-471-15301-6.

[5] Sanjay Mazumdar. *Composites manufacturing: materials, product, and process engineering*. CRC Press LLC, 2001. ISBN 0-8493-0585-3.

[6] Dirk Hans-Joachim Adrian Lukaszewicz. *Optimisation of high-speed automated layup of thermoset carbon-fibre preimpregnates*. PhD thesis, University of Bristol, 2011.

[7] Klaus Drechlser and Roland Hinterhölzl. Lecture: Process simulation and material modeling of composites, 2014.

[8] Carroll Grant. Automated processes for composite aircraft structure. *Industrial Robot: An International Journal*, 33(2):117–121, 2006.

[9] W Goldsworthy, E Hardesty, and H Karlson. Geodesic path length compensator for composite-tape placement head, May 14 1974. US Patent 3,810,805.

[10] Pierre Debout, Hélène Chanal, and Emmanuel Duc. Tool path smoothing of a redundant machine: Application to automated fiber placement. *Computer-Aided Design*, 43(2):122–132, 2011.

[11] A. Hamlyn and Y. Hardy. Faserapplikationsmaschine mit flexiblen faserzufuhrschläuchen, September 22 2010. EP Patent 2,117,818.

[12] Giuseppe Dell'Anno, Ivana Partridge, Denis Cartié, Alexandre Hamlyn, Edmon Chehura, Stephen James, and Ralph Tatam. Automated manufacture of 3D reinforced aerospace composite structures. *International Journal of Structural Integrity*, 3(1):22–40, 2012.

[13] Adriana Blom. *Structural performance of fiber-placed, variable-stiffness composite conical and cylindrical shells*. PhD thesis, Delft University of Technology, 2010.

[14] Costas Soutis. Carbon fiber reinforced plastics in aircraft construction. *Materials Science and Engineering: A*, 412(1):171–176, 2005.

[15] Susan Krolewski and Timothy Gutowski. Effect of the automation of advanced composite fabrication process on part cost. *SAMPE Q.;(United States)*, 18(1), 1986.

[16] Brian F. Tatting and Zafer Gürdal. *Design and manufacture of elastically tailored tow placed plates*. National Aeronautics and Space Administration, Langley Research Center, 2002. ISBN 9781234310646.

[17] Hugo Sarrazin and George Springer. Thermochemical and mechanical aspects of composite tape laying. *Journal of Composite Materials*, 29(14):1908–1943, 1995.

[18] Florian Henne, Stefan Ehard, Andreas Kollmannsberger, Birte Hoeck, Markus Sause, Guenther Obermeier, and Klaus Drechsler. Thermoplastic in situ fiber placement for future solid rocket motor casings manufacturing. In *SAMPE Europe - SETEC 14 TAMPERE - 9th. Technical Conference & Table Top Exhibition Efficient Composite Solutions to Foster Economic Growth*, 2014.

[19] Ralf Engelhardt, Philipp Hörmann, F. Rinker, G. Weyerer, and Klaus Drechsler. Analysis of the cost efficiency of automated fiber placement based on an extensive process breakdown. In *SEICO 14-35th International Technical Conference & Forum Low Cost Composite Processing, from Aerospace OOA to Automotive Thermoplastic*, 2014.

[20] Kevin Potter, C Langer, B Hodgkiss, and S Lamb. Sources of variability in uncured aerospace grade unidirectional carbon fibre epoxy preimpregnate. *Composites Part A: Applied Science and Manufacturing*, 38(3):905–916, 2007.

[21] Kevin Potter, B Khan, M Wisnom, T Bell, and J Stevens. Variability, fibre waviness and misalignment in the determination of the properties of composite materials and structures. *Composites Part A: Applied Science and Manufacturing*, 39(9):1343–1354, 2008.

[22] Kevin Potter. Understanding the origins of defects and variability in composites manufacture. In *International Conference on Composite Materials (ICCM)-17, Edinburgh, UK*, 2009.

[23] Dennis Crowley, Carwyn Ward, and Kevin Potter. A status of acceptance criteria and process requirements in advanced composites manufacturing, and whether they are fit for purpose. Technical report, SAE Technical Paper, 2013.

[24] Dennis Crowley, Carwyn Ward, and Kevin Potter. The manufacture of advanced composite parts to rigid industrial specifications-can it be made? Technical report, SAE Technical Paper, 2013.

[25] C Ridgard. Out of autoclave composite technology for aerospace, defense and space structures. *Proceedings of SAMPE 2009, Baltimore, MD, May*, 2009.

[26] Jens Hinrichsen and Cesar Bautista. The challenge of reducing both airframe weight and manufacturing cost. *Air & Space Europe*, 3(3):119–121, 2001.

[27] R Crossley, P Schubel, and De Focatiis, D. Time–temperature equivalence in the tack and dynamic stiffness of polymer prepreg and its application to automated composites manufacturing. *Composites Part A: Applied Science and Manufacturing*, 52(0):126–133, 2013.

[28] R Lichtinger, P Hörmann, D Stelzl, and R Hinterhölzl. The effects of heat input on adjacent paths during automated fibre placement. *Composites Part A: Applied Science and Manufacturing*, 68:387–397, 2015.

[29] Roland Lichtinger, Jiannan Tang, and Klaus Drechsler. Peel tack simulation with applied cohesive fracture in reference to feed rate and compaction force. In *Proceedings of the 6th European Congress on Computational Methods in Applied Sciences and Engineering (ECCOMAS 2012)*. Vienna University of Technology, Austria, September 2012.

[30] Dirk Hans-Joachim Adrian Lukaszewicz and Kevin Potter. The internal structure and conformation of prepreg with respect to reliable automated processing. *Composites Part A: Applied Science and Manufacturing*, 42(3):283–292, 2011.

[31] Rene Holschuh, David Becker, and Peter Mitschang. Cost competitiveness of hybrid structures based on thermoplastic in-situ tape-placement process. In *Technical Conference, Society for the Advancement of Material and Process Engineering; SAMPE Tech 2012*, 2012.

[32] Jaroslav Mackerle. Finite element analyses of sandwich structures: a bibliography (1980 - 2001). *Engineering Computations*, 19(2):206–245, 2002.

[33] R. Oster. Non-destructive testing methodologies on helicopter fiber composite components challenges today and in the future. In *18th World Conference on Nondestructive Testing*, 2012.

[34] G. Di Bella, C. Borsellino, and L. Calabrese. Effects of manufacturing procedure on unsymmetrical sandwich structures under static load conditions. *Materials & Design*, 35(0):457–466, 2012.

[35] B. Castanié, J. Barrau, and J. Jaouen. Theoretical and experimental analysis of asymmetric sandwich structures. *Composite Structures*, (55):295 – 306, 2002.

[36] B. Castanié, J. Barrau, J. Jaouen, and S. Rivallant. Combined shear/compression structural testing of asymmetric sandwich structures. *Experimental Mechanics*, 44(5):461–472, 2004.

[37] I.L. Paris, M. Hojjati, J. Chen, and M. Octeau. Characterization of composites sandwich ramp failure under tensile loading. In *17th International Conference on Composite Materials - Proceedings of the 17th International Conference, ICCM-17 2009, Edinburgh, UK, Jul 2009*, volume 17, 2009.

[38] Bijan Shirinzadeh, Gursel Alici, Chee Foong, and Gary Cassidy. Fabrication process of open surfaces by robotic fibre placement. *Robotics and Computer-Integrated Manufacturing*, 20(1):17–28, 2004.

[39] Bijan Shirinzadeh, Gary Cassidy, Denny Oetomo, Gursel Alici, and Marcelo Ang. Trajectory generation for open-contoured structures in robotic fibre placement. *Robotics and Computer-Integrated Manufacturing*, 23(4):380–394, 2007.

[40] Bijan Shirinzadeh, Chee Foong, and Boon Tan. Robotic fibre placement process planning and control. *Assembly Automation*, 20(4):313 – 320, 2000.

[41] Adriana Blom, Brian Tatting, Jan Hol, and Zafer Gürdal. Fiber path definitions for elastically tailored conical shells. *Composites Part B: Engineering*, 40(1):77–84, 2009.

[42] Roland Lichtinger, Javier Lacalle, Roland Hinterhölzl, Uwe Beier, and Klaus Drechsler. Simulation and experimental validation of gaps and bridging in the automated fiber placement process. *Science and Engineering of Composite Materials*, pages 1–18, epub ahead of print.

[43] Ralf Schledjewski. Automated placement of CF/PEEK tape material. In *Keynote-Lecture; First International Symposium on Automated Composites Manufacturing*, 2013.

[44] R Crossley, P Schubel, and N Warrior. The experimental determination of prepreg tack and dynamic stiffness. *Composites Part A: Applied Science and Manufacturing*, 43(3):423–434, 2012.

[45] J. Zhang and M. F. Ashby. The out-of-plane properties of honeycombs. *International Journal of Mechanical Sciences*, 34(6):475–489, 1992.

[46] F. Helenon, Dirk Hans-Joachim Adrian Lukaszewicz, D. Ivanov, and Kevin Potter. Modelling slit tape deposition during automated fibre placement. In *ICCM19*. ICCM19, 2013.

[47] George Springer. Resin flow during the cure of fiber reinforced composites. *Journal of composite materials*, 16(5):400–410, 1982.

[48] AC Loos and GS Springer. Calculation of cure process variables during cure of graphite-epoxy composites. *ASTM STP*, 797:110–18, 1983.

[49] R Dave, JL Kardos, and M Duduković. A model for resin flow during composite processing: Part 1 general mathematical development. *Polymer Composites*, 8(1):29–38, 1987.

[50] R Dave, JL Kardos, and M Duduković. A model for resin flow during composite processing part 2: numerical analysis for unidirectional graphite/epoxy laminates. *Polymer Composites*, 8(2):123–132, 1987.

[51] Henry Darcy. *Les Fontaines publiques de la ville de Dijon. Exposition et application des principes à suivre et des formules à employer dans les questions de distribution d'eau, etc.* Victor Dalmont, 1856.

[52] Gregory Smith and Anoush Poursartip. A comparison of two resin flow models for laminate processing. *Journal of composite materials*, 27(17):1695–1711, 1993.

[53] Timothy Gutowski, Tadahiko Morigaki, and Zhong Cai. The consolidation of laminate composites. *Journal of Composite Materials*, 21(2):172–188, 1987.

[54] T Gutowski, Z Cai, S Bauer, D Boucher, J Kingery, and S Wineman. Consolidation experiments for laminate composites. *Journal of Composite Materials*, 21(7):650–669, 1987.

[55] Z Cai and T Gutowski. The 3-D deformation behavior of a lubricated fiber bundle. *Journal of composite materials*, 26(8):1207–1237, 1992.

[56] C Lekakou, MAKB Johari, and MG Bader. Compressibility and flow permeability of two-dimensional woven reinforcements in the processing of composites. *Polymer Composites*, 17(5):666–672, 1996.

[57] P Hubert and A Poursartip. A method for the direct measurement of the fibre bed compaction curve of composite prepregs. *Composites part A: applied science and manufacturing*, 32(2):179–187, 2001.

[58] Yizhuo Gu, Min Li, Zuoguang Zhang, and Zhijie Sun. Numerical simulation and experimental study on consolidation of toughened epoxy resin composite laminates. *Journal of composite materials*, 40(24):2257–2277, 2006.

[59] S Comas-Cardona, P Le Grognec, C Binetruy, and P Krawczak. Unidirectional compression of fibre reinforcements. part 1: A non-linear elastic-plastic behaviour. *Composites science and technology*, 67(3):507–514, 2007.

[60] Min Li, Yizhuo Gu, Zuoguang Zhang, and Zhijie Sun. A simple method for the measurement of compaction and corresponding transverse permeability of composite prepregs. *Polymer composites*, 28(1):61–70, 2007.

[61] Pascal Hubert, Reza Vaziri, and Anoush Poursartip. A two-dimensional flow model for the process simulation of complex shape composite laminates. *International Journal for Numerical Methods in Engineering*, 44(1):1–26, 1999.

[62] Rui Guedes, António Marques, and Albert Cardon. Analytical and experimental evaluation of nonlinear viscoelastic-viscoplastic composite laminates under creep, creep-recovery, relaxation and ramp loading. *Mechanics of Time-Dependent Materials*, 2(2):113–128, 1998.

[63] R Pitchumani, S Ranganathan, RC Don, J Gillespie, and M Lamontia. Analysis of transport phenomena governing interfacial bonding and void dynamics during thermoplastic tow-placement. *International journal of heat and mass transfer*, 39(9):1883–1897, 1996.

[64] John Gangloff, Shatil Sinha, and Suresh Advani. A model for tow impregnation and consolidation for partially impregnated thermoset prepregs. In *Proceedings of SAMPE Conference & Exposition. Long Beach, CA, US*, 2011.

[65] Dirk Hans-Joachim Adrian Lukaszewicz and Kevin Potter. Through-thickness compression response of uncured prepreg during manufacture by automated layup. *Proceedings of the Institution of Mechanical Engineers, Part B: Journal of Engineering Manufacture*, 226(2):193–202, 2012.

[66] Byung Kim, Kevin Potter, and Paul Weaver. Continuous tow shearing for manufacturing variable angle tow composites. *Composites Part A: Applied Science and Manufacturing*, 43(8):1347–1356, 2012.

[67] Heinrich Hertz. Ueber die berührung fester elastischer körper. *Journal für die reine und angewandte Mathematik*, 92, 1882.

[68] K Johnson. *Contact mechanics*. Cambridge University Press, 1985. ISBN 0 521 34796 3.

[69] A.B. Liggins. *The practical application of Fuji Prescale pressure-sensitive film.* Springer US, 1997. ISBN 978-0-412-60780-6.

[70] Fuji prescale film - two-sheet type for ultra super low pressure. URL `http://www.fujifilm.eu/fileadmin/products/prescale/media/Two_sheet_Type_for_Ultra_Super_Low_Pressure_klein.pdf`. visitied on 2014-10-02.

[71] Hexcel Composites. Properties: A comprehensive guide to standard hexcel honeycomb materials, configurations, and mechanical properties. `http://www.hexcel.com`, 1999. visited on 2014-09-05.

[72] B. Johnson. Conformable compaction apparatus for use with a fiber placement machine, May 21 2002. US Patent 6,390,169.

[73] K.K. Chawla. *Composite Materials: Science and Engineering.* Materials Research and Engineering. Springer, 2012. ISBN 9780387743646.

[74] Jun Zhang, Noboru Kikuchi, Victor Li, Albert Yee, and Guy Nusholtz. Constitutive modeling of polymeric foam material subjected to dynamic crash loading. *International Journal of Impact Engineering*, 21(5):369 – 386, 1998.

[75] C Hall, C Ward, D Ivanov, and Kevin Potter. The compaction of uncured toughened prepreg laminates in relation to automated forming. In *15th European conference on composite materials. Venice, Italy*, 2012.

[76] Heraeus Noblelight. Infrared basics and technology. URL `http://www.heraeus-noblelight.com/media/webmedia_local/media/pdf/ip/downloads/IR_basics_and_technology.pdf`. vistited on 2014-08-25.

[77] John Tierney and John Gillespie. Modeling of heat transfer and void dynamics for the thermoplastic composite tow-placement process. *Journal of Composite Materials*, 37(19):1745–1768, 2003.

[78] B. Chern, Moon, T., and Howell, J. Thermal analysis of in-situ curing for thermoset, hoop-wound structures using infrared heating: Part i—predictions assuming independent scattering. *Journal of Heat Transfer*, 117(3):674–680, 1995.

[79] B. Chern, Moon, T., and Howell, J. Thermal analysis of in-situ curing for thermoset, hoop-wound structures using infrared heating: Part ii—dependent scattering effect. *Journal of Heat Transfer*, 117(3):681–686, 1995.

[80] Bih Chern, Tess Moon, and John Howell. On-line processing of unidirectional fiber composites using radiative heating: I. model. *Journal of Composite Materials*, 36(16):1905–1934, 2002.

[81] Bih Chern, Tess Moon, and John Howell. On-line processing of unidirectional fiber composites using radiative heating: Ii. radiative properties, experimental validation and process parameter selection. *Journal of Composite Materials*, 36(16):1935–1965, 2002.

[82] Fazil. Sonmez and Hahn, Thomas. Modeling of heat transfer and crystallization in thermoplastic composite tape placement process. *Journal of Thermoplastic Composite Materials*, 10(3):198–240, 1997.

[83] R. Pitchumani, Gillespie, J., and M. Lamontia. Design and optimization of a thermoplastic tow-placement process with in-situ consolidation. *Journal of Composite Materials*, 31(3):244–275, 1997.

[84] Jonghyun Kim, Tess Moon, and John Howell. Transient thermal modeling of in-situ curing during tape winding of composite cylinders. *Journal of Heat Transfer*, 125(1):137–146, 2003.

[85] Anais Barasinski, Adrien Leygue, Eric Soccard, and Arnaud Poitou. An improvement in thermal modelling of automated tape placement process. *AIP Conference Proceedings*, 1315(1):185–190, 2011.

[86] M. Narnhofer, R. Schledjewski, P. Mitschang, and L. Perko. Simulation of the tape-laying process for thermoplastic matrix composites. *Advances in Polymer Technology*, 32(S1):705–713, 2013.

[87] Noha Hassan, Joseph Thompson, Batra, R., Hulcher, Bruce, Xiaolan Song, and Alfred Loos. A heat transfer analysis of the fiber placement composite manufacturing process. *Journal of Reinforced Plastics and Composites*, 24(8): 869–888, 2005.

[88] F. Chinesta, A. Leygue, B. Bognet, Ch. Ghnatios, F. Poulhaon, F. Bordeu, A. Barasinski, A. Poitou, S. Chatel, and S. Maison-Le-Poec. First steps towards an advanced simulation of composites manufacturing by automated tape placement. *International Journal of Material Forming*, 7(1):81–92, 2012.

[89] P. Hörmann, D. Stelzl, R. Lichtinger, S. Van Nieuwenhove, G. Mazón Carro, and K. Drechsler. On the numerical prediction of radiative heat transfer for thermoset automated fiber placement. *Composites Part A: Applied Science and Manufacturing*, 67(0):282 – 288, 2014. ISSN 1359-835X.

[90] C. Madhusudana. *Thermal contact conductance*. Mechanical Engineering Series. Springer, New York, 1996. ISBN 0-387-94534-2.

[91] Stephen Cassidy and Paul Monaghan. Effect of contact resistances on the thermal conductivity of an unconsolidated fibre-reinforced thermoplastic prepreg stack. *Composites Manufacturing*, 5(4):225–230, 1994.

[92] Arthur Levy, Dirk Heider, John Tierney, and John Gillespie. Inter-layer thermal contact resistance evolution with the degree of intimate contact in the processing of thermoplastic composite laminates. *Journal of Composite Materials*, 48(4):491–503, 2014.

[93] Andrew Johnston. *An integrated model of the development of process-induced deformation in autoclave processing of composite structures*. PhD thesis, The Univertsity of British Columbia, Vancouver, 1997.

[94] Toray Carbon Fibers America, Inc. T800H Data Sheet: Technical data sheet No. CFA-007. URL `http://www.toraycfa.com/pdfs/t800hdatasheet.pdf`. visited on 2014-07-04.

[95] Donna Dykeman. *Minimizing uncertainty in cure modeling for composites manufacturing*. PhD thesis, The Univertsity of British Columbia, Vancouver, 2008.

[96] Robert Swann and Claud Pittman. *Analysis of effective thermal conductivities of honeycomb-core and corrugated-core sandwich panels*. NASA technical note. National Aeronautics and Space Administration, 1961.

[97] Javad Fatemi and Martin Lemmen. Effective thermal/mechanical properties of honeycomb core panels for hot structure applications. *Journal of Spacecraft and Rockets*, 46(3):514–525, 2009.

[98] Tom Bitzer. *Honeycomb technology: materials, design, manufacturing, applications and testing*. Springer Netherlands, 1997. ISBN 9780412540509.

[99] Robert Madding. *Thermographic Instruments and systems*. PhD thesis, University of Wisconsin, Madison and Wisconsin.

[100] Y.A. Cengel. *Heat and Mass Transfer: A Practical Approach*. McGraw-Hill series in mechanical and aerospace engineering. McGraw-Hill, 2006. ISBN 9780071257398.

[101] Scott Holmes, Stanley Lawton, and John Haake. Method for heating and controlling temperature of composite material during automated placement, September 17 2002. US Patent 6,451,152.

[102] R Schledjewski and M Latrille. Processing of unidirectional fiber reinforced tapes-fundamentals on the way to a process simulation tool (ProSimFRT). *Composites science and technology*, 63(14):2111–2118, 2003.

[103] Muhammad Khan, Peter Mitschang, and Ralf Schledjewski. Identification of some optimal parameters to achieve higher laminate quality through tape placement process. *Advances in Polymer Technology*, 29(2):98–111, 2010.

[104] A Barasinski, A Leygue, E Soccard, and A Poitou. In situ consolidation for thermoplastic tape placement process is not obvious. In *The 14th International ESAFORM Conference on Material Forming: ESAFORM 2011*, volume 1353, pages 948–953. AIP Publishing, 2011.

[105] Anaïs Barasinski, Adrien Leygue, Eric Soccard, and Arnaud Poitou. Identification of non uniform thermal contact resistance in automated tape placement process. *International Journal of Material Forming*, pages 1–8, 2013.

[106] Fabien Poulhaon, Chady Ghnatios, Brice Bognet, Anais Barasinski, Adrien Leygue, and Francisco Chinesta. A numerical approach for the evaluation of residual stresses in the automated tape placement process. In *ASME 2012 11th Biennial Conference on Engineering Systems Design and Analysis*, pages 41–49. American Society of Mechanical Engineers, 2012.

[107] Fazil Sonmez and Mustafa Akbulut. Process optimization of tape placement for thermoplastic composites. *Composites Part A: Applied Science and Manufacturing*, 38(9):2013–2023, 2007.

[108] Adriana Blom, Shahriar Setoodeh, Jan Hol, and Zafer Gürdal. Design of variable-stiffness conical shells for maximum fundamental eigenfrequency. *Computers & Structures*, 86(9):870–878, 2008.

[109] FT Peirce. 26-The "Handle"OF Cloth as a measurable Quantity. *Journal of the Textile Institute Transactions*, 21(9):T377–T416, 1930.

[110] DIN 53362. Bestimmung der Biegesteifigkeit - Verfahren nach Cantilever, October 2003.

[111] A Zosel. Adhesion and tack of polymers: Influence of mechanical properties and surface tensions. *Colloid and Polymer Science*, 263(7):541–553, 1985.

[112] KJ Ahn, JC Seferis, T Pelton, and M Wilhelm. Analysis and characterization of prepreg tack. *Polymer composites*, 13(3):197–206, 1992.

[113] Donates Satas. Handbook of pressure sensitive technology. *Van Nostrand-Rheinhold Co, New York, USA*, 1982.

[114] J Johnston. Tack: known by many names, it's difficult to define. I. *Adhesives age*, 26(12):34–38, 1983.

[115] R Crossley, P Schubel, and N Warrior. The experimental determination of prepreg tack and dynamic stiffness. *Composites Part A: Applied Science and Manufacturing*, 43(3):423–434, 2012.

[116] BC Duncan, LA Lay, A Olusanya, RA Roberts, and SG Abbott. The measurement of adhesive tack. In *Proceedings of 7th International Conference on Adhesion and Adhesives, Cambridge*, 1999.

[117] Y Lin, C Hui, and H Conway. A detailed elastic analysis of the flat punch (tack) test for pressure-sensitive adhesives. *Journal of Polymer Science Part B: Polymer Physics*, 38(21):2769–2784, 2000.

[118] Ph Tordjeman, E Papon, and J Villenave. Tack properties of pressure-sensitive adhesives. *Journal of Polymer Science Part B: Polymer Physics*, 38(9):1201–1208, 2000.

[119] *Finat Technical Handbook: Test Methods*. FINAT Technical Handbook. FINAT, 2014.

[120] ASTM D3167-10: Standard Test Method for Floating Roller Peel Resistance of Adhesives, 2010.

[121] R Crossley, P Schubel, and N Warrior. The experimental characterisation of prepreg tack. In *The 17th International Conference on Composite Materials (ICCM-17)*, 2009.

[122] Daniel Stelzl, Ricardo Marin Carsi, Michael Hollerith, Jonathan Roth, Javier Lacalle, and Klaus Drechsler. A peel tack test bench for automated fibre placement processes. In *Composites week @ Leuven and Texcomp-11 Conference. 16-20 September 2013, Leuven*, 2013.

[123] JA Greenwood and JBP Williamson. Contact of nominally flat surfaces. *Proceedings of the Royal Society of London. Series A. Mathematical and Physical Sciences*, 295(1442):300–319, 1966.

[124] CY Hui, YY Lin, and JM Baney. The mechanics of tack: viscoelastic contact on a rough surface. *Journal of Polymer Science Part B: Polymer Physics*, 38 (11):1485–1495, 2000.

[125] JA Greenwood and JJ Wu. Surface roughness and contact: an apology. *Meccanica*, 36(6):617–630, 2001.

[126] B Persson. Theory of rubber friction and contact mechanics. *The Journal of Chemical Physics*, 115(8):3840–3861, 2001.

[127] B Persson, F Bucher, and Bernardino Chiaia. Elastic contact between randomly rough surfaces: comparison of theory with numerical results. *Physical Review B*, 65(18):184106, 2002.

[128] B Persson. Adhesion between an elastic body and a randomly rough hard surface. *The European Physical Journal E: Soft Matter and Biological Physics*, 8(4):385–401, 2002.

[129] B Persson, O Albohr, C Creton, and V Peveri. Contact area between a viscoelastic solid and a hard, randomly rough, substrate. *The Journal of chemical physics*, 120(18):8779–8793, 2004.

[130] B Persson, O Albohr, Ugo Tartaglino, AI Volokitin, and Erio Tosatti. On the nature of surface roughness with application to contact mechanics, sealing, rubber friction and adhesion. *Journal of Physics: Condensed Matter*, 17(1): R1, 2005.

[131] B Persson. Contact mechanics for randomly rough surfaces. *Surface Science Reports*, 61(4):201–227, 2006.

[132] C Yang and B Persson. Contact mechanics: contact area and interfacial separation from small contact to full contact. *Journal of Physics: Condensed Matter*, 20(21):215214, 2008.

[133] C Creton and L Leibler. How does tack depend on contact time and contact pressure. *J Polymer Sci B Polymer Phys*, 34:545–554, 1996.

[134] K Kendall. The adhesion and surface energy of elastic solids. *Journal of Physics D: Applied Physics*, 4(8):1186, 1971.

[135] C Derail, A Allal, G Marin, and Ph Tordjeman. Relationship between viscoelastic and peeling properties of model adhesives. part 1. cohesive fracture. *The Journal of Adhesion*, 61(1-4):123–157, 1997.

[136] C Derail, A Allal, G Marin, and Ph Tordjeman. Relationship between viscoelastic and peeling properties of model adhesives. part 2. the interfacial fracture domains. *The Journal of Adhesion*, 68(3-4):203–228, 1998.

[137] Cyprien Gay and Ludwik Leibler. Theory of tackiness. *Physical review letters*, 82(5):936, 1999.

[138] AN Gent and GR Hamed. Peel mechanics. *The Journal of Adhesion*, 7(2): 91–95, 1975.

[139] DH Kaelble. Rheology of adhesion. *Journal of Macromolecular Science-Reviews in Macromolecular Chemistry*, 6(1):85–112, 1971.

[140] DH Kaelble. Theory and analysis of peel adhesion: rate-temperature dependence of viscoelastic interlayers. *Journal of Colloid Science*, 19(5):413–424, 1964.

[141] DH Kaelble. Peel adhesion: influence of surface energies and adhesive rheology. *The Journal of Adhesion*, 1(2):102–123, 1969.

[142] DH Kaelble and RS Reylek. Peel adhesion: rate dependence of micro fracture processes. *The Journal of Adhesion*, 1(2):124–135, 1969.

[143] YY Lin, CY Hui, and YC Wang. Modeling the failure of an adhesive layer in a peel test. *Journal of Polymer Science Part B: Polymer Physics*, 40(19): 2277–2291, 2002.

[144] A Zosel. Adhesive failure and deformation behaviour of polymers. *The journal of adhesion*, 30(1-4):135–149, 1989.

[145] Anthony Kinloch. *Adhesion and adhesives: science and technology.* Springer, 1987. ISBN 9780412274404.

[146] E Raphael and P De Gennes. Rubber-rubber adhesion with connector molecules. *The Journal of Physical Chemistry*, 96(10):4002–4007, 1992.